ARECA PALM SHEATH: A PLANT-BASED MATERIAL ALTERNATIVE TO PLASTICS FOR FOODWARE PRODUCTS

by

Debapriya Pinaki Mohanty

A Dissertation

Submitted to the Faculty of Purdue University

In Partial Fulfillment of the Requirements for the degree of

Doctor of Philosophy

School of Industrial Engineering

West Lafayette, Indiana

December 2021

THE PURDUE UNIVERSITY GRADUATE SCHOOL
STATEMENT OF COMMITTEE APPROVAL

Dr. Srinivasan Chandrasekar, Chair

School of Industrial Engineering

Dr. Ramses Martinez

School of Industrial Engineering

Dr. Kevin P. Trumble

School of Materials Engineering

Dr. Mysore Dayananda

School of Materials Engineering

Dr. Christopher J. Gilpin

Life Science Microscopy Facility

Approved by:

Dr. Abhijit Deshmukh

I dedicate this dissertation to my wife Surya Kanya Tapati and our daughter Aakriti. With a special gratitude, I also dedicate this work to my brother, parents, in-laws and family members, who have always been supportive of my endeavors.

ACKNOWLEDGMENTS

I would like to express my heartfelt appreciation to my committee chair, Professor Srinivasan Chandrasekar, for his guidance, expertise and patience through this dissertation. I want to give special thanks to Prof. Mysore Dayananda for his unwavering support, and discussions throughout my PhD research. I would also like to thank the members of my advisory committee, Professor Kevin Trumble, Professor Ramses Martinez, and Dr. Christopher J Gilpin, for their advice and assistance. My gratitude also goes to all of my current and former laboratory colleagues in the Center for Materials Processing and Tribology, including Dr. Anirudh Udupa, Dr. Jason M. Davis, Dr. Mojib Saei, Dr. Koushik Viswanathan, and Dr. Mohammed Naziru Issahaq for their collaboration and discussions. I am grateful to Dr. Anil Chandra of BMS College, Bangalore, India, for providing me areca sheath samples and for discussions. Finally, I would like to thank Dr. James B Mann for his assistance with developing some unique experimental setups as well for his participation in my research. The thesis would not have been possible without the assistance provided by these individuals.

TABLE OF CONTENTS

LIST OF TABLES

LIST OF FIGURES

ABSTRACT

The proliferation of single-use plastics in the foodware and packaging sector has stimulated interest in sustainable material substitutes that can be processed efficiently and which possess sufficient structural integrity. Herein, we study the structure, mechanical response and diffusion properties of leaf-sheath from a representative palm species—*Areca catechu*—widely cultivated in the Indian sub-continent and Southeast Asia. The study of this material system, and the specific attributes, are motivated by the use of this material in foodware applications. Foodware such as plates and bowls can be produced from the areca sheath, directly, in a single step, by stretch forming analogous to sheet metals. The material is eco-friendly, biodegrading in ~100 days. Formability and water diffusion are two key attributes of relevance for foodware, since the former attribute determines the shape change capability of the material and range of producible shapes; and the latter, foodware product (structural) integrity and life.

We characterize the morphology (external structure) and anatomy (internal structure) of the sheath using imaging techniques and composition analysis. The sheath is shown to resemble a composite material, with structural characteristics intermediate between those of the palm leaf and stem. By measuring the mechanical response of the sheath to various types of 1D and 2D loading (e.g., uniaxial tension and compression, biaxial stretching, rolling), and hydration conditions, we show that the sheath material has high stretch-formability, especially when hydrated. This formability is similar to that of the most ductile sheet metals. The formability is shown to be further enhanced by addition of small quantities of NaOH (~5%) during hydration. Local deformation measurements in biaxial stretching, based on analysis of distortion of grid-markers inscribed onto sheath samples, have enabled characterization of strain-field anisotropy and mode of failure in the sheath. By consolidating the mechanical test results, we present a forming limit diagram for the leaf-sheath.

The structural integrity and life of foodware products produced from the leaf-sheath are directly determined by diffusion of liquids (e.g., water, oils) through the sheath wall thickness. Water and oils are important constituents of semi-solid and solid foods. Diffusion of water is also important for designing the hydration cycle to enhance formability. The diffusion of water through the sheath material process is studied using mass gain measurements and *in situ* imaging of water transport.

We determine the diffusion coefficient for water, which is critical for estimating product life. The diffusion coefficient for the matrix is shown to be one order of magnitude greater than for the fiber. We vary salt concentration in the water by controlled additions of NaCl and note a non-monotonic dependence of the diffusion on concentration. By subjecting the leaf-sheath to a short-time (~ 3 minutes) thermal treatment (~ 80^0 C), a hydrophobic wax layer can be made to secrete onto the leaf surface. This wax coating is found to significantly reduce the water diffusion, enabling the sheath foodware life to be increased.

Lastly, we argue, that since the leaf-sheath is a "waste product" of the palm, it has negligible embodied energy (4 to 5 orders of magnitude smaller) compared to paper and plastics based foodware.

We discuss the implications of the results for single-step forming of high-aspect ratio products and structures from the palm sheath, methods to reduce diffusion of liquids and improve foodware product life, and some directions for future research into mechanical behavior of plant leaf materials from a forming perspective.

1. INTRODUCTION

The deleterious effects of plastics on the environment are well-known, and are the subject of numerous scientific reviews and popular articles. Among industrial sectors that use plastics, the foodware/packaging segment is by far the largest consumer [1]. A disturbing aspect of plastics consumption in this sector is use of products that are designed for short-term (single) use **(Fig. 1.1)**. Most of these products, post consumption, find their way either into landfills or are dumped into the ocean, adversely impacting human and animal health, and affecting precious groundwater resources [2,3]. Increasing awareness of these facts has spawned efforts to combat the otherwise unopposed increase of single-use plastics. For example, several cities around the world have banned single-use plastic products such as bags, cutlery and straws. But interestingly, these plastics have seen a resurgence in the current 2020-21 pandemic environment, driven by enhanced demand for plastic bags, packaging, bottled water, besides PPE, due to concerns driven by safety and cross-contamination. Nevertheless, heightened environmental standards and the journey towards a greener earth, even if temporarily stayed, are inevitable. This is leading to increased research interest in finding sustainable and environment-friendly materials and processing alternatives in the foodware and related packaging sector.

Figure 1.1 Single-use food packaging, currently dominated by plastics and paper.

The major challenges for these research efforts in the foodware/packaging sector are two-fold: Firstly, identifying sustainable alternative materials that mechanically, functionally and aesthetically match or even surpass plastics; and secondly, developing scalable, energy-efficient

processes for converting these materials into products at a cost comparable to equivalent plastic products currently in use (e.g., plates, cutlery). In recent years, plant-based materials processing has emerged as an attractive alternative for this sector. A notable everyday example is in production of utensils such as plates and bowls by molding of paper or bagasse. The former is pulped and molded wood fiber, while the latter is lignocellulosic residue, left behind after processing of sugarcane or sorghum stalks. Although the plant provides the primary production of these fibrous materials (and fixes CO_2 from the atmosphere in the process), the advantages of paper- and bagasse-based products are offset by the energy intensity of the pretreatment, pulping, and drying steps involved in their manufacture. These processes are also among the most water intensive of all materials production processes. Furthermore, the pulp-based manufacturing often involves use of fillers and chemicals (~ 30%).

The present research seeks to exploit a new opportunity in manufacturing with plant-based natural materials - a fundamentally transformative route for production of food packaging that is highly eco-friendly and energy efficient. This route involves product manufacturing directly from plant materials, without use of energy-intensive processing steps like pulping, and *sans* fillers and chemicals. An illustrative example of this manufacturing involves areca palm (or betel palm), a palm that has been cultivated in India, South-East Asia, East Africa, Hawaii and Pacific Islands. Areca palm has been grown for more than 2000 years, as may be inferred from references to their nuts (betel nut) in ancient Indian (Sanskrit) literature and medicinal texts**,** and even Herodotus circa 340 B.C [4–7] .

Figure 1.2 shows foodware such as plates and bowls that have been produced by deformation processing (forming) of areca palm sheath. These products are also commonly classified as palm leaf products. The figure, more broadly, also captures the "cradle-to-grave" life cycle of the palm-sheath and the products. This palm-sheath deformation processing (forming) is very much analogous to forming of sheet metal by stretching or punching, using dies. The direct forming of the sheath into foodware completely avoids use of filler materials or additives. The sheath material biodegrades in approximately 100 days, compared to hundreds of years for plastics. In the latter case, the degradation also results in polymer microparticles which are of growing concern worldwide [8]. Furthermore, since the palm is grown primarily for its nuts, the sheath, which is shed by the tree at periodic intervals, is essentially "waste material" that, in this foodware case, is

utilized for producing highly eco-friendly products. This use of waste material highlights another attractive advantage of areca palm-leaf product manufacturing. The energy consumed in production of the single-use palm sheath products should be just a small fraction of that used in production of similar plastic or paper-based products, as discussed later. This energy advantage is likely to be at least an order of magnitude greater if the "recycling energy and service" contribution provided by the Earth, often taken as free, is included [9,10].

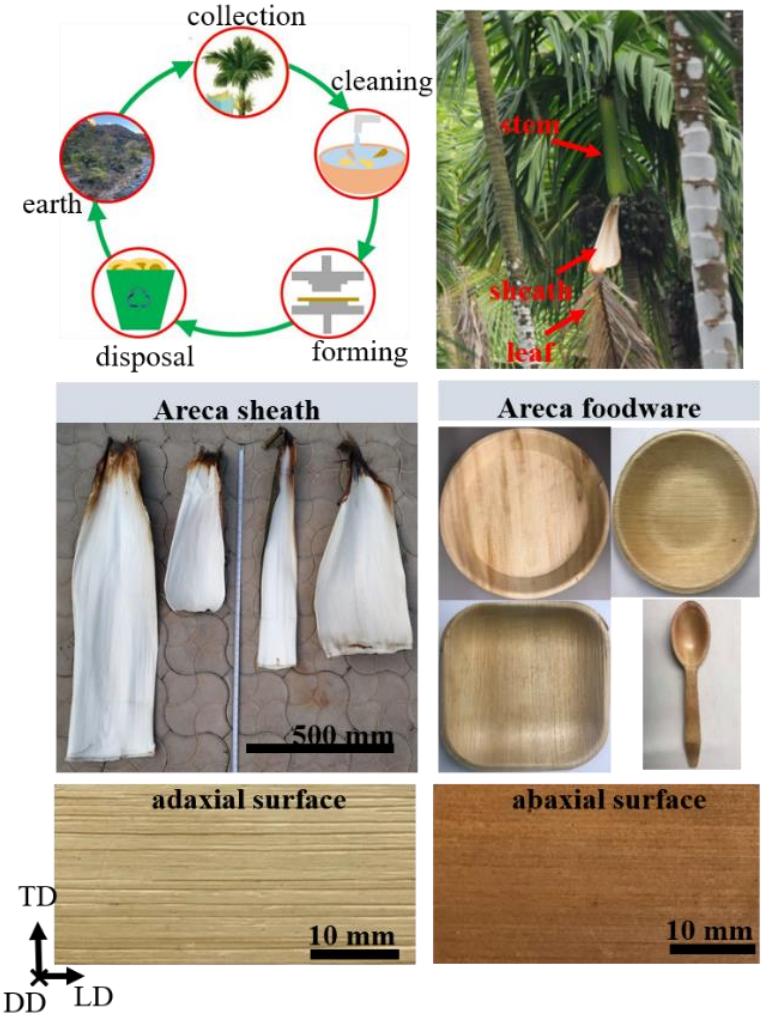

Figure 1.2 Areca palm leaf sheath and products: (top row) areca product life cycle (left), and palm tree showing sheath (right); (middle row) typical areca sheath and foodware products; (bottom row) adaxial and abaxial surfaces of a sheath and plate/bowl, and striation features.

In the emerging economies and developing world, palm-sheath foodware is usually manufactured in small sheds, using low-cost press equipment (< 10,000 dollars) and a workforce comprised

mainly of women. Areca leaf foodware has been in use in South Asia for at least 200 years, finding a listing even in Watts' famous Dictionary of Indian Economic Products [11]. Palm leaf products are now finding customers globally, including in the USA and Europe, because of their attractive attributes: functionality and aesthetics; rapid biodegradability; and price. Given that there are 2500+ documented palm species across the world, including in Florida, California, Hawaii and various US Territories, and that palms are the second most common plant species after grasses [12–14], the potential scope even for just exploiting various types of palm leaf in direct manufacturing of foodware products is vast.

1.1 Rationale

From a scientific standpoint, the most intriguing aspect of the areca palm sheath is its capacity for large shape change, i.e., high formability. In this regard, it appears to resemble ductile metals like aluminum, copper and low-carbon steels. However, practically nothing is known about the mechanical response or structural properties of this sheath material (e.g., strength, formability, fracture), nor the microstructure basis for its deformation characteristics. Hence, it is not possible to answer questions such as: a) what are the shapes and products that can be formed out of these materials, i.e., forming limits?, b) what is the structural integrity of the product (e.g., strength, stiffness), and what are material failure limits?, and, c) can sheath or leaf from other more widely occurring palms, e.g., coconut, palmettos, or other plant species (e.g., banana) be used to manufacture similar products and more? The answers to such questions, and, importantly, the methodologies to answer them, are well-known for forming of metals and polymers, contributing in no small measure to the widespread use of these materials in structural applications.

Besides formability and strength properties, diffusion of water in sheath materials is also important for foodware applications. For it is diffusion, that is one of the principal factors that determines the shelf life of products such as plates and bowls – that is, how long can a plate/bowl hold solid, semi-solid or liquid food without its constituents permeating through the sheath? It has been reported, mainly by manufacturers, that the areca foodware can hold semi-solid foods for roughly 60 minutes before the plate/bowl becomes soggy due to liquids (mainly water) seeping through the ~ 3 mm thick sheath wall. In discussions with manufacturers, it has become clear that if this shelf life can be enhanced to 90 or 120 minutes by reducing the seepage (diffusion), then the

foodware product life will be increased, increasing its economic competitiveness and value. Therefore, it is worthwhile to obtain some level of understanding of the diffusion properties of the sheath material. Besides, adding to scientific knowledge of how fluid diffusion occurs through porous media, such an understanding could also help develop strategies for reducing the rate of water diffusion through the sheath and help extend product life. It is likely to be of value, as will be seen, also for designing hydration treatments to improve formability.

To establish the direct forming paradigm and better understand structural degradation of the sheath-based foodware, the current research explores four closely-related research objectives: (1) establish microstructure and composition of palm sheath (2) characterize mechanical and physical properties of palm sheath, and establish forming-limit diagrams that can help also demarcate producible shapes; (3) understand how hydration and temperature affect formability via material microstructure; and (4) characterize diffusion of water through the sheath to determine how this impacts structural integrity (product life) and formability of the sheath. The research objectives are guided by the hypothesis that formability and diffusion (liquid into the sheath) are the two key properties of the sheath that determine its use in foodware applications – from a manufacturing and product durability perspective.

Palm sheath product manufacturers, perhaps because of limited access to scientific and technological resources, have relied on empiricism and intuitive understanding of material behavior for their product design and manufacturing. Many scientific opportunities, vis-a-vis these palm leaf materials, thus await exploration, which could unlock new manufacturing potential. These could also result in a systematic way for identifying plant-based natural materials of high formability, and spawn new means for production of foodware from plant materials.

1.2 Problem statement

With the goal of enhancing applications of plant-based materials in foodware applications, via the direct deformation processing approach, this thesis seeks to study microstructure, formability and diffusion properties of a model plant material system – areca palm sheath. To advance this goal, the following specific objectives are addressed in the thesis.

Microstructure Firstly, we characterize the external (morphology) and internal (anatomy) structure of the sheath material and compare it with those of other natural plant-based materials.

In addition, because the sheath connects the stem and the leaf, we investigate how the structure of the sheath differs from the structure of the stem and leaf. Since the sheath is a plant material, it is expected to have a heterogeneous microstructure. Consequently, structure characterization is done at various length scales using techniques such as optical microscopy, scanning electron microscopy (SEM), (micro) computer-aided tomography (μCT), Fourier transform infrared spectroscopy (FTIR), optical profilometry and contact angle measurements. An expected outcome here is improved understanding of how structural features at different length scales influence formability, diffusion and associated parametric effects. Understanding microstructure-property relationships could also be of value for identifying other plant-based materials that can be directly formed like the areca palm sheath.

Deformation response Secondly, the deformation response of areca palm sheath is characterized using different loading configurations – tension, compression, rolling and biaxial stretching (Limiting Dome Height testing) – typical of loading in metal forming processes and structural applications. This is used to establish structural properties such as strength, stiffness (Young's modulus) and failure strain; and a forming limit diagram (FLD) for in-plane loading such as stretching and bending. Based on analogy with bamboo, perhaps the most widely studied plant material to date for structural applications, the deformation response of areca palm sheath is expected to be anisotropic, and influenced by temperature and hydration. The effects of hydration are also expected to influence the formability of the sheath, see ensuing discussion as to how the sheath is currently formed based on visits to manufacturers. Hence the effect of these parameters on structural and formability properties, and deformation anisotropy, is characterized in these loading configurations. A combination of *ex situ* and *in situ* measurement techniques is used for the deformation characterization. An expected outcome is an FLD for areca palm sheath that will be valuable for determining the range of product shapes that can be formed. The FLD, together with the structural property data, will also be useful for product design.

Diffusion properties Thirdly, we examine the response of the palm sheath material when in contact with water. Water is known not only to permeate through the material but also decrease its stiffness. The rate at which water permeates the material is measured using established diffusion measurement techniques. A characterization is made of the underlying mechanism by which this diffusion occurs, aided by knowledge gained of the sheath microstructure. Parametric effects that

are examined in this diffusion context are effects of salt concentration, water temperature and sheath heat-treatment. This line of investigation can, potentially, lead to strategies for decreasing the rate of water permeation through the sheath; controlling/calibrating the effect of hydration on sheath mechanical properties; and enhancing formability by optimizing the interactive effects of hydration and temperature.

The report is organized as follows. First, a brief background of areca palm and its uses in various products is provided in chapter 2. In this background chapter, we also give details of the manufacturing process for areca foodware based on the knowledge gained during site visits to manufacturers in and around Bangalore, India. In chapter 3, we report on studies carried out of sheath morphology and anatomy. In chapters 4 and 5, we discuss sheath formability, anisotropy in material deformation, and various parametric effects on mechanical response. In chapter 6, we present results from a study of water diffusion through the sheath. In chapter 7, we discuss thermal treatment of the sheath as a method to enhance product life and sustainability of foodware products. The report ends with a summary of results and suggestions for future work.

2. BACKGROUND

Areca refers to about 50 species of palm trees that grow mostly in South Asia, East Africa, the Arabian Peninsula, and some Southeast Asian countries. The most prominent amongst these - *areca catechu* - popularly called the areca-nut palm is a slender medium-sized tree, growing straight up to 20 m in height, and with a trunk that is 25–40 cm in diameter. The leaves are 1–2 m long, pinnate, with numerous, crowded leaflets. Traditionally, the palm is grown mainly for its nut, commonly known as areca or betel nut, which is used as a masticatory stimulant [7]. Besides the nut, the tree also produces 10-15 leaf sheaths every year. Areca sheaths are long slender structures (**Fig. 1.2**) that protect inflorescence (flower arrangement) during the early stage of development, but are shed in the later stage. Since the palm is grown mainly for its nut, the sheaths, as with other palms, are essentially waste products. Besides use of the sheaths in foodware such as plates and bowls, other current, albeit more limited, applications are in footwear, hats, and spoons.

Sheaths used in foodware production (**Fig. 1.2)** are usually mature, and have lengths of 0.5-1 m, width < 0.5 m, and thickness < 4 mm. It is this sheath that is formed by a punching or stretching type forming process into plates and bowls, very much analogous to forming of sheet metals. **Figure 1.2** also shows examples of commercially-available plates and bowls, with diameters in range of 10 cm to 20 cm. These product geometries highlight the large shape changes that the initially near-flat sheath material can undergo – illustrative of its extraordinary formability. The sheath has two distinct surfaces: the adaxial surface that faces the stem, and the abaxial surface that faces out (away from the stem). The adaxial side (surface) of the sheath forms the top (inner) side of a plate/bowl**,** while the abaxial side constitutes the bottom (outer) side of the plate/bowl. This latter surface has a much darker appearance than the adaxial surface, besides being stiffer and stronger. Both surfaces have striations that run along the length. The length direction of these striations will henceforth be referred to as longitudinal direction (LD), and the direction perpendicular to the striations, in the plane of the sheath, as the transverse direction (TD). The out-of-plane normal to the sheath surface is parallel to the depth direction (DD). The striations are the principal source of surface roughness, both in the sheath and in the formed products.

The foodware manufacturing process The manufacturing of areca palm leaf products is commonly done in small shops utilizing simple infrastructure, with women constituting most of

the workforce. The labor- intensive nature of the production makes the sector an important source of employment in India, Thailand, and Malaysia, where this palm is prevalent. To get a first-hand look at the manufacturing, we visited several palm-leaf plate manufacturers near Bangalore, India, a key region for plant-based foodware products. From these visits, and discussions with various trade-industry groups, it became clear that the forming of the leaf products has been developed largely on basis of tradition, and trial and error. After harvesting, the sheaths are cleaned and dried to prevent mold formation, which would otherwise render them useless, and then stored in a cool place. However, in the dried condition, the sheath is not amenable to deformation. To provide the flexibility (formability) needed for shape change, each sheath is first immersed in water for 1 to 2 hours. It is then removed from the water and covered with a cloth, or sealed, for approximately 24 hours. This hydration pre-treatment is critical for developing the requisite formability, as we learned from the manufacturers.

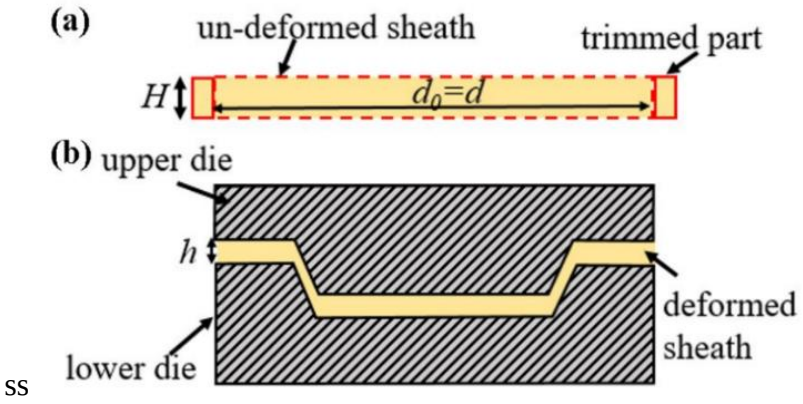

ss

Figure 2.1 Schematic of areca sheath forming process: a) sheath of thickness H prior to the deformation; b) final product of thickness h ($\sim 0.8H$) obtained by stretch forming (pressing) sheath between two dies (temperature ~100^0 C). The upper die acts as a punch, applying a force to the sheath in the pressing step.

A typical forming process, very similar to that used in commercial practice, is shown in **Fig. 2.1**. A hydrated "flat" sheath, of initial thickness H (**Fig. 2.1a**) is deformed into the desired product shape, between two dies (**Fig. 2.1b**), by means of a force applied to the upper (movable) die. This forming is akin to stretch-deformation of a plate by a circular punch. The formed product thickness is equal to the gap between the dies, h. If after this shape change the upper die (load) is released, then the sheath will typically spring back to its original flat shape. In order to have the sheath retain

the desired shape defined by the dies, one or both of the dies is kept heated at ~ 120 °C to drive away the moisture introduced during the water immersion [15]. A 3-4 minutes exposure to this temperature is sufficient to expel the moisture and "lock-in" the shape change. In this way, plates, bowls and other shapes are manufactured from the sheaths.

The manufacturing sequence described above highlights two material attributes that are central to the forming of shapes: the role of moisture in effecting ductility and achieving large-scale shape changes; and material heating, post-deformation, to "freeze" the shape change, akin to molding thermoplastic, but without the melting. The heating is both the rate-controlling step and the energy-consumption step in the production process. Our discussions with the manufacturers also brought to the fore several product manufacturing challenges, such as (1) predicting what shapes (e.g., high-aspect ratio cups, spoons) can be produced from the sheath; (2) understanding the interactive effects of hydration and thermomechanical process parameters on the sheath formability; (3) enhancing product service life (e.g., in plates, from ~ 60 minutes to 90-120 minutes), which is controlled by the rate of permeation of liquid food constituents (e.g., water, oil) through the sheath; (4) improving quality (e.g., finish, appearance); (5) reducing cost and improving throughput; and (6) identifying other palm species (e.g., coconut) and processing routes that could be exploited for producing sheath products on an even larger scale.

Embodied energy and sustainability attributes The areca forming suggests opportunities for opening a fundamentally new dimension of materials and manufacturing sustainability. This may be appreciated by comparing the embodied energy of palm sheath products to that of plastics and paper (in **Chapter 5**). Embodied energy includes the primary material production energy and the processing (shaping) energy [16,17]. In the case of plastics, this includes the energy to extract the raw mineral (natural gas), produce monomer feedstock and synthesize polymer resin. The processing energy represents the energy to convert the polymer resin pellets into a useful shape, such as a plate made by melting and injection molding. For most materials, the primary production dominates the embodied energy; in the case of molded polystyrene it represents over 85% of the total.

Paper products are often seen as the classic sustainable substitute for plastic foodware. Their primary production is accomplished mostly by nature (growth of wood). However, in the production of paper, the cellulose fibers of wood are delignified, pulped, and then pressed and

dried into fiber sheets. While the processing (shaping) energy is small, pulping is quite energy (and water) intensive, so the embodied energy of paper products is still about half that of plastics. Bagasse papers, produced from sugar cane stalks, are considered more sustainable. Although pulping is still involved, the fiber source is a by-product of cane sugar production, unlike trees, which are intentionally grown and harvested for fiber. These non-wood paper products have gained considerable traction among eco-conscious consumers as a more sustainable alternative for foodware, being derived from a plant by-product rather than primary harvest. Their cost is however higher than wood paper products.

Table 2.1 Sustainability factors for plastic, paper and palm sheath as food packaging materials [16]. (courtesy: Prof. Kevin Trumble)

	Plastic	**Paper**	**Areca sheath**
Embodied energy	Very high	High	Near zero
Water uses	High	Very high	Very low
CO_2 emissions	Moderate	Moderate	Near neutral
Disposability	Very poor	Moderate	Very high

The direct manufacture of foodware from palm sheath represents a fundamentally different class of materials processing from the standpoint of embodied energy. The palm tree sheds sheath naturally in seasonal growth cycles. Not only is the plant not sacrificed in harvesting the sheaths, but they are then formed directly without the energy-intensive pulping process necessary for production of paper (wood or bagasse). In this regard, the primary form of the material literally "falls from the tree." Similarly, direct use of plant materials, without pulping, circumvents the high water use of paper production. With only a small amount of energy needed for processing to shapes, the CO_2 emissions through the entire product lifecycle is essentially that emitted in the natural decay of the disposal process (composting), a process that would occur in any event. The sustainability attributes of the areca sheath compared to plastics and paper for foodware applications are further compared in **Table 2.1**. Indeed, the disposable (single-use) foodware/packaging application of the direct-use natural materials can be viewed as taking useful service from the material as only a brief interruption in the natural lifecycle of plant matter. This study will use the areca palm as a model system to explore these interactions systematically, and

from this basis identify the full scope of potential for such direct-use natural materials in Eco-Manufacturing.

3. STRUCTURE OF PALM LEAF-SHEATH

3.1 Abstract

A study has been made of the morphological (external) and anatomical (internal structure) features of areca palm leaf-sheath. There is very little information in the literature on the structure of the sheath, which connects the leaf with the stem of the plant. In contrast, the structure of palm leaf and stem has been characterized extensively. The areca sheath features were examined at various length scales using imaging techniques such as optical microscopy, optical profilometry, and electron microscopy. Additionally, the main constituents of the sheath such as cellulose, lignin, hemicellulose and wax, were analyzed compositionally. The sheath is slender, typically < 4 mm thick, with two distinct external surfaces – the adaxial (inner) surface which faces the stem, and a stiffer abaxial (outer) surface. The internal structure resembles a composite material of the fiber-matrix type. This internal structure exhibits a variation from the abaxial to the adaxial side. The morphological features of the sheath are similar to those of a leaf while the anatomical features more closely resemble those of the stem. The observations suggest that the sheath structure is intermediate between that of the leaf and the stem and resembles a hybrid of the two structures.

3.2 Introduction

A study of the external and internal features of areca sheath was undertaken to better understand how it compares structurally with the stem and leaf of the palm. There is very little information in the published literature about the structure of areca palm sheath, and, more broadly, even of any type of palm sheath. Furthermore, in the present study, we are interested in sheath properties of relevance to areca foodware applications such as formability, strength and diffusion. Since these are structure sensitive, it was felt that a study of the areca sheath anatomy and morphology would be of value also for better understanding these properties. Unless otherwise stated, the data reported about the sheath samples in this chapter are all taken from mature sheath collected after they were shed by the palm tree.

Plant morphology is the study of external features of plants, while anatomy pertains to the study of the internal structure of the plant materials at the cellular/microscopic level. Detailed morphological and anatomical data on components of the palm tree such as stem, leaf, and root,

are widely available [14] . However, with regard to palm sheath, the data available is essentially limited to morphology only [14]. In many instances, the sheath which connects the stem and the leaf of the plant is referred to as leaf-sheath. This terminology is likely based on some level of morphological similarity between sheath and leaf. To the best of our knowledge, no detailed anatomical studies have been undertaken of the sheath material analogous to studies of the leaf and stem. In a few instances**,** references have been made to anatomical features of the sheath, primarily the fiber and matrix, in order to relate them to mechanical properties [18,19]. This chapter is devoted to a discussion of sheath external and internal structure, characterized by various microscopy, profilometry and indentation testing methods; and sheath composition.

3.3 Sheath Morphology and Composition

3.3.1 Sheath material

Areca sheaths were collected from a plantation near Bangalore, India, during the summer of 2019. The sheaths were in a matured condition and had been shed by the tree. After the collection, dust and other contaminants were removed from the sheaths by cleaning with compressed air and dry air. The sheaths were then sealed inside a plastic zipper bag to protect them from atmospheric moisture. Samples for the various experiments – structure and composition characterization, mechanical testing, and diffusion - were prepared, as needed, from this lot.

Figure 3.1a and b show the areca palm tree with the leaf, stem and sheath labeled. The areca sheath has a green exterior in its early stages of growth. The sheath external surfaces turn brown upon maturity. **Figure 3.1b and c** show the mature (brown) sheaths that are used for making foodware products. The inter-linkages between the stem, sheath and leaf, and their relative sizes on the tree can be inferred from these images. The length of a mature sheath is typically between 0.3 meter to 1 meter, with a maximum width of half a meter at the middle (**Fig. 3.1d**). Various locations in the sheath (e.g., center, base, middle, tip etc.) that are referred to in the thesis are marked in the **Fig. 3.1c and e.**

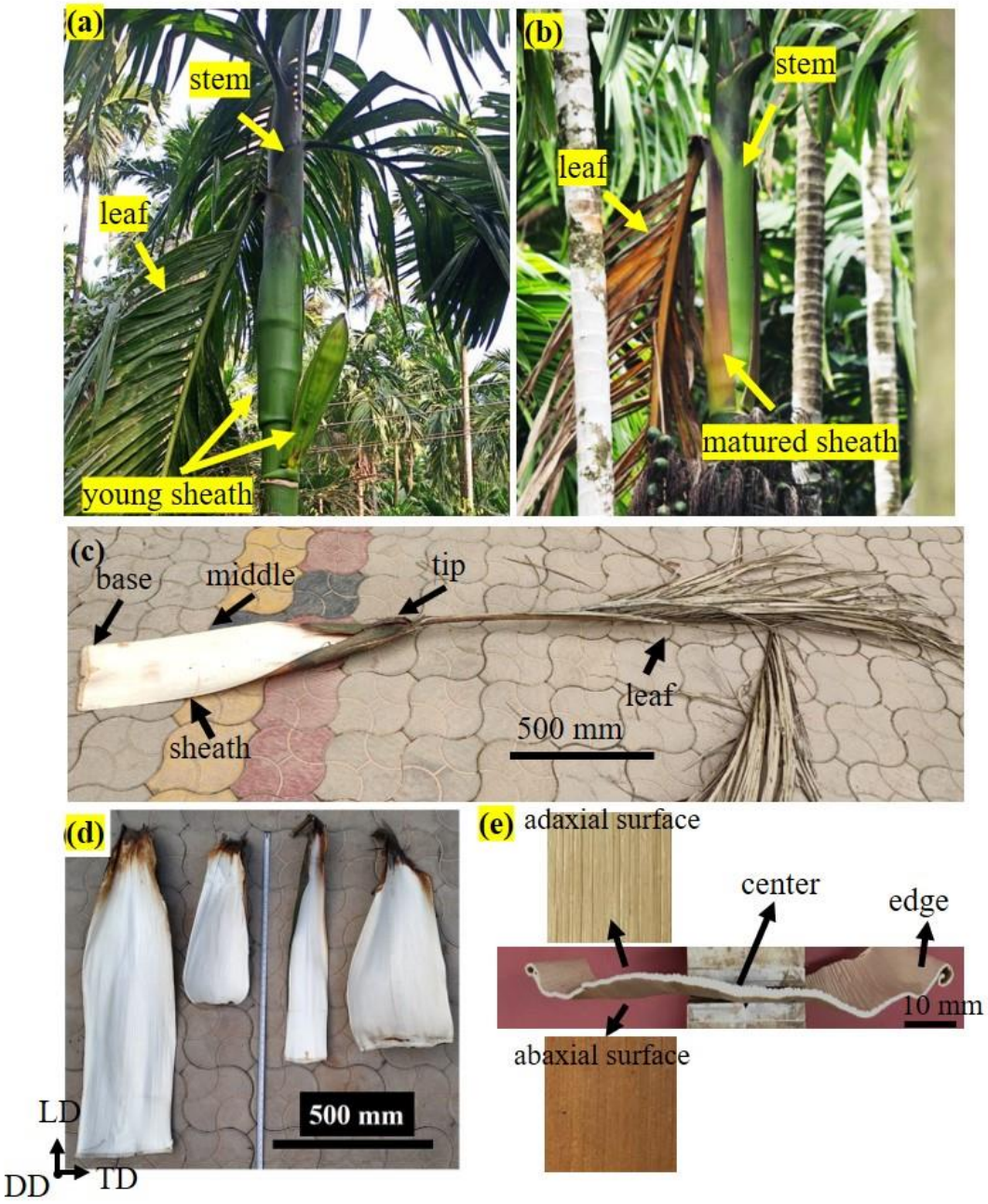

Figure 3.1 Overview of areca catechu palm tree and sheath - (a) tree showing various parts and young (green) sheath (b) tree with matured (brown) sheath still attached. (c) matured sheath and branch/leaf detached from the tree (d) Sheath of different sizes displaying long slender structure. The sheath length direction the longitudinal direction (LD), and width direction is the transverse direction (TD); the out-of-plane normal to the surface is the depth/thickness direction (DD). (e) Image of the sheath along width direction showing thickness; and adaxial and abaxial surfaces with striations. Note the sheath is thinner at the edges.

The base of the sheath connects to the stem while the tip connects to the leaf. The region that is approximately half way between the tip and the base is defined as the middle part. The two extremities along the transverse direction are called the sheath edges. The region midway between the sheath edges is called the central region **(Fig. 3.1e).** The longitudinal (LD), transverse (TD), and thickness (DD) directions of the sheath are the directions parallel to its length, width, and thickness (into the plane), respectively; these directions are defined in **Fig. 3.1d**. The LD × DD plane is called the longitudinal plane while the TD ×DD plane is referred to as the transverse plane.

Figure 3.1e shows the two main external surfaces (adaxial, abaxial) of the sheath, and the sheath thickness dimension along one of its edges. The sheath is usually thicker (~3 mm) in the center and thinner at the edges (~1.5 mm). The inner surface of the sheath which faces the stem of the is called the abaxial surface, while the outer sheath surface is called the adaxial surface. The abaxial surface is darker in appearance compared to the adaxial surface. Both the adaxial and abaxial surface have striations or grooves that run along the length of the sheath – the LD direction. The grooves are more prominent on the adaxial surface.

The internal structure of the sheath broadly resembles a composite material composed of matrix, fiber and porosity. An overview of this internal structure, at different length scales from the bulk sheath down to the cellulose microfiber level, is shown in **Fig. 3.2**. The cellulose microfibers are the structural elements constituting the cell wall. We will elaborate on both the morphology and anatomy of the sheath in the ensuing.

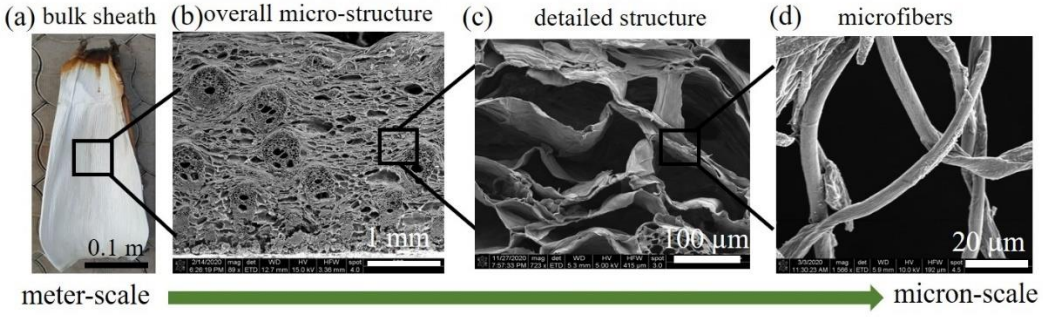

Figure 3.2 Sheath structure at different length scales; from meter to micrometer scale. a) bulk sheath b) overall microstructure in thickness cross-section (SEM image, transverse plane) c) and d) SEM images at higher magnification showing cellulose microfibers that are structural element of the cell wall.

3.3.2 Morphology

The thickness of sheath was measured at various locations in the sheath (e.g., edge, center), along its length, using a digital Vernier caliper with resolution of 0.001 mm. **Figure 3.3** shows the measured thickness data from six different sheaths. The thickness of the entire sheath is not uniform along its width. It is typically greater at the center (~3 mm, black bar) than at the edge (~1.7 mm, red bar). Also, the thickness is highest at the base of the sheath and decreases toward the tip.

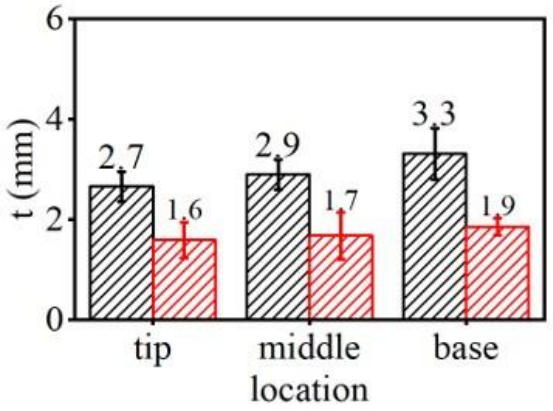

Figure 3.3 Thickness (t) of sheath at different locations. Black and red bars represent measurements done at the center and edge of the sheath.

Fig. 3.4 shows the external features of the sheath from the adaxial and abaxial surfaces. The top row of images in the figure is from the adaxial surface and the bottom row from the abaxial surface. The optical microscope images (left column) show that the abaxial surface is darker than the adaxial surface. Both surfaces have striations running parallel to the sheath LD.

The surface topography of the adaxial and abaxial surfaces, at center and edge, was measured by optical profilometry (Zygo NewView 8300; white light interferometry). For obtaining the profile, the sample was scanned with a 10X objective lens at 1X zoom. The 3D topography of the surfaces at center and edge is shown in **Fig. 3.4**. The scanned area was 10 mm × 2 mm in size, with the lateral resolution of the profilometer ~0.4 micrometers. Various details of the striations such as mean amplitude and wavelength were obtained from the profile using equivalent roughness parameters that the profilometer software computes. This roughness was obtained in terms of the parameters R_z, and λ_d , estimated along line traces in the profile made perpendicular to the

striation lengths. R_z is estimated as the mean of the five largest peak-to-valley heights along a line, while λ_d is the mean lateral spacing between adjacent peaks or adjacent valleys. R_z is thus a measure of the mean amplitude of the striations while λ_d gives the striation wavelength (spacing).

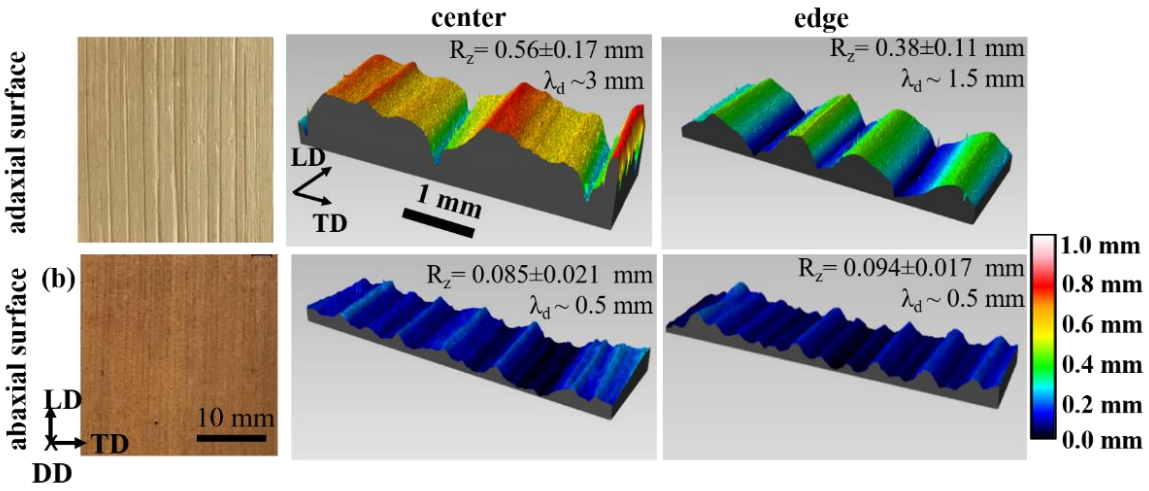

Figure 3.4 Optical image and 3D profile details of surface topography of (top row) adaxial surface and (bottom row) abaxial surface. Striations on the adaxial and abaxial surfaces run parallel to the sheath LD.

The average value of R_z measured on the adaxial surface of six different sheaths was 0.56±0.17 mm at the sheath center, and 0.38±0.11 mm at the edges. On the abaxial surface, R_z was 0.085±0.021 mm and 0.094±0.017 mm, at the center and edge, respectively. The λ_d values were ~3 mm and ~1.5 mm, at the center and edge, respectively, of the adaxial surface. On the abaxial surface, this wavelength was ~ 0.5 mm at both the center and edge of the abaxial surface. These results are summarized in **Fig. 3.4**.

It is clear from these measurements that on the adaxial surface, the striations have much larger amplitudes and wavelengths than on the abaxial surface. Furthermore, the striations are deeper at the center than along the edges on this surface. On the abaxial surface, the striations are very similar, both in amplitude and wavelength, across the whole width of the surface – indicating a surface with more consistent or uniform roughness.

3.3.3 Hardness and stiffness

Besides the morphological differences such as roughness and color, the adaxial and abaxial surfaces of the sheath show differences in stiffness and hardness. Both of these mechanical property parameters were characterized by nano-indentation using a Hysitron (UBi 1) system and a Berkovich diamond pyramidal indenter. For the hardness measurements, sheath samples (mature) of size 1 cm^2 (in-plane dimension) was prepared from both the abaxial and adaxial surface. The sheath was attached to the sample holder using super glue. Each surface was indented at 25 different points with a peak indentation load of 5 mN. The indenter loading and unloading rate was 0.5 mN/sec. The structure stiffness and Young's modulus (E) of the material are obtained from the slope of the unloading curve at the maximum penetration depth, i.e., initial unloading point.

Figure 3.5 shows the load-displacement (penetration) curves for the two surfaces. The slope of the unloading curve at maximum depth is much higher for the abaxial surface than the adaxial surface, indicating that the abaxial surface material has a higher stiffness and E than the adaxial surface material. The estimated stiffness value was $\sim 8.9 \times 10^{-3}$ mN/nm for the abaxial surface, approximately ~3 times the stiffness of the adaxial surface ($\sim 3.2 \times 10^{-3}$ mN/nm). The corresponding E modulus values are 1.67 GPa for the abaxial surface and 0.67 GPa for the adaxial surface. The hardness of the abaxial surface was also greater (0.81 GPa) than that of the adaxial surface (0.35 GPa). It should be noted that while these modulus and hardness values are suitable for relative comparison, the absolute values themselves should be taken with a note of caution. This is because both the hardness and modulus values are derived from the indentation load-displacement curve using a material deformation model that is not universally applicable to all material types.

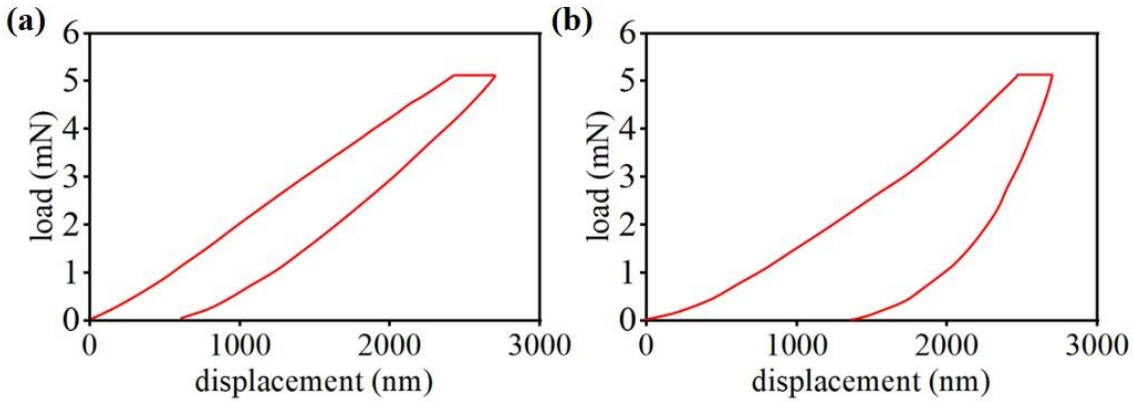

Figure 3.5 Nanoindentation load-displacement curves for (a) adaxial and (b) abaxial surface. The stiffness is obtained from the slope of the curve at initial unloading. Abaxial surface stiffness is ~3 times that of the adaxial surface.

3.3.4 Composition

Cellulose, hemicellulose, and lignin are the main constituents of the plant material cell wall (solid region). An analogy can be drawn between the constituents of the plant material and those of structural reinforced concrete. The cellulose microfiber (**Fig 3.2d**) is a structural element that is analogous to the steel rod in concrete. The hemicellulose and lignin are natural fillers and binding elements that keep the cellulose microfibers together. These are analogous to cements and other additives that serve as binder in concrete. Furthermore, wax is also often a constituent in some of the palm trees [20,21]. In fact, the well-known Carnauba wax comes from the leaves of the Carnauba palm. The areca sheath also contains wax. In the present composition characterization, we first removed the wax by treating the sheath sample with an acetone-ethanol solution. Subsequently, we separated the cellulose microfibers by alkali treatment and bleaching [22,23].

The reagents used for the various constituent extraction were acetone, ethanol, NaOH and hydrogen peroxide, all purchased from Fischer Scientific. Samples of the sheath were cut and crushed into small pieces using a manual hand crusher. The pieces were then rinsed with distilled water for 1 hour and vacuum dried. For the dewaxing (wax removal), the dried samples were agitated in a mixture of acetone-ethanol (2:1 v/v) at 80^0C for 3 hr. The solution was then filtered through a Buckner funnel and vacuum dried for 2 hr. This dewaxing process was repeated four times to remove the wax completely. The amount of wax was estimated as equal to the weight loss of the sample after this acetone-ethanol dewaxing treatment.

The dewaxed sample was then soaked and stirred vigorously in 7% NaOH aqueous solution at 80^0C using a magnetic stirrer (2000 rpm for 4 hr). This process was repeated three times. At the end of each step, the sample was filtered in a Buckner funnel and then rinsed with distilled water multiple times until the sample achieved a neutral pH. As a final stage, a bleaching process was carried out to remove residual lignin. This process resulted in discoloration of microfibers. The bleach solution was prepared by adding NaOH (7% wt.) to aqueous hydrogen peroxide (11% v/v), maintaining pH level at 11. The extract from the previous step was stirred in the bleached solution for three times (3 hours each time). After each treatment, the microfibers were filtered and washed with distilled water until neutral pH was attained in the sheath material. The microcellulose fibers were then vacuum dried to remove residual water. At the end of this extraction process, the cellulose microfibers are left as a residue. The solution removes hemicellulose and lignin, and other substances as well, during the alkali treatment and bleaching process. We did not separate and measure the individual amounts of hemicellulose and lignin in the slurry.

Based on this analysis, the weight fractions of wax, cellulose and other constituents (mainly hemicellulose and lignin) in the sheath were estimated as 4.65±1.75 %, 22.41±3.93 %, and 72.93±2.75 %, respectively.

3.4 Sheath Anatomy

3.4.1 Method

The anatomical features (internal structure) of the areca sheath were examined using a high-resolution field emission gun-SEM (Quanta 3D) operating in low-vacuum mode. For this examination, thickness cross-sections of the sheath in the transverse plane were prepared by dissecting the cut-out samples with a fine scalpel. The SEM images were processed and analyzed using ImageJ software, an open source image analysis software.

Various "microstructure" parameters were computed to describe the anatomy. The sheath porosity (p), that is the area fraction of pores, was computed after converting the image on transverse plane to a binary image by using the ImageJ software **(Fig. 3.6)**. In this binary image, the solid regions (cell walls) and pores appeared as white and black, respectively. The area fraction of fiber (A_f), fiber size (d_f), mean distance between the fibers (λ), and perimeter of fiber per unit measured

area (S_V) were estimated from the images taken in transverse plane cross-section using Tomkeieff's equation [24]. The area fraction of the fiber (A_f) is equal to the total cross-sectional area of the fiber divided by the cross-sectional area of the sample over which the measurement is done. The area fraction of the matrix (A_m) is then obtained as $1 - A_f$. Based on theory of stereo-metallurgy (quantitative metallography), the area fraction of fiber is always equal to the volume fraction and linear fraction measured in the test region [24].

The density (ρ) was estimated by dividing mass of the sample, measured with a balance (0.001 gm resolution), by the sample volume obtained from measurement of sample dimensions. By the rule of mixtures, the sheath density is related to area fraction of fiber and matrix, and their individual densities, by [25]:

$$\rho = \rho_f A_f + \rho_m A_m = (\rho_f - \rho_m) A_f + \rho_m \qquad 3.1$$

where, ρ is the sheath density, and the subscripts f and m refer to fiber and matrix, respectively. Based on measurements of the overall sheath density and area fraction of fiber and matrix, the matrix and fiber density could both be estimated using **Eq. 3.1**.

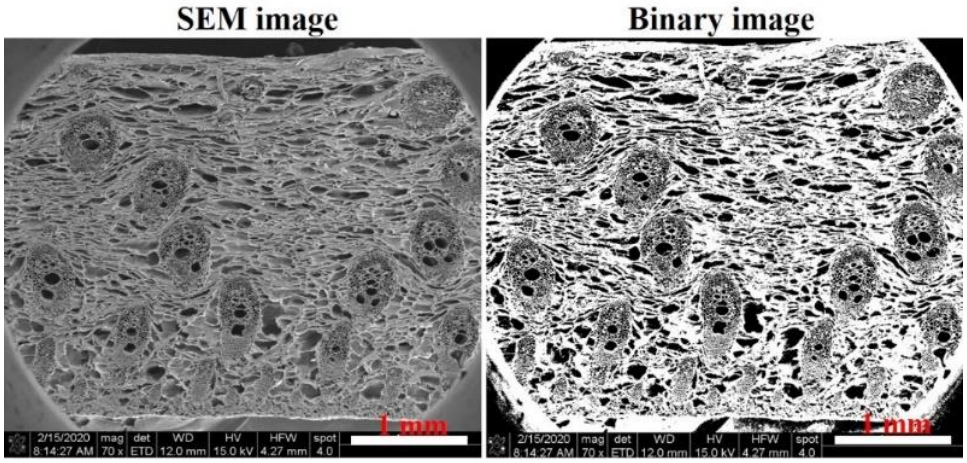

Figure 3.6 SEM image of sheath cross-section converted to a binary image by using the ImageJ software.

3.4.2 Results

Figures 3.7a and b show the principal anatomical features of the sheath, as obtained from SEM images of transverse and longitudinal plane cross-sections of the sheath. The epidermis,

hypodermis, ground tissue, and fibers (vascular and non-vascular type) are the principal features. The schematic diagram in **Figure 3.7c** is a representation (not to scale) of these internal features of the sheath, reconstructed from the SEM image of the transverse plane cross-section (**Fig. 3.7a**). We will discuss the sheath structure, sequentially, as we go from the outer adaxial and abaxial surfaces into the interior of the sheath.

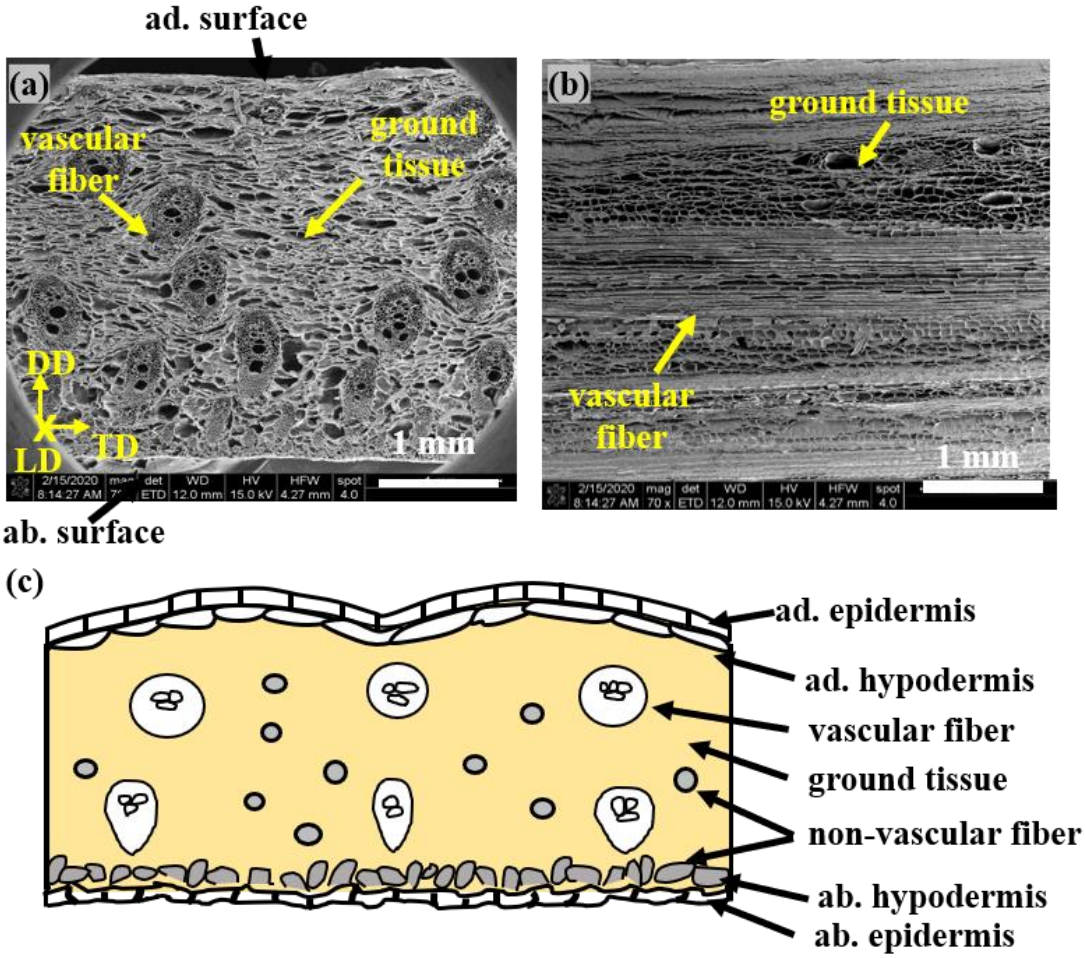

Figure 3.7 Internal structure of areca sheath in thickness cross-section. SEM images of cross-section in the (a) transverse and (b) longitudinal planes showing vascular bundle (fiber) and ground tissue. (c) Schematic diagram of sheath cross-section in transverse plane showing various structural features and their variation from adaxial (ad.) to abaxial (ab.) surface (picture reconstructed from the SEM images).

Overall structure of the sheath The epidermis is the outermost layer of the sheath (skin layer) on both the adaxial and abaxial sides (**Fig 3.8**). From the SEM images in this figure, the thickness of the epidermis layer on both these sides is seen to be ~ 0.02 mm. **Figures 3.8a and d** (left column)

show images of the epidermis layer on the adaxial and abaxial sides, respectively, in surface (plan) view. Stomatal (surface) pores can be seen in both these epidermis layers (inset **Figs. 3.8a and d**). The stomata facilitate flow of gases into and out of the plant. The typical stomata pore size is ~ 0.02 mm. From the surface view images, it is possible to obtain the areal density of the stomata. The areal density of stomata on the abaxial surface (58±8 /mm^2) is higher than the density on the adaxial surface (28±6 /mm^2). **Figures 3.8b and e** show the corresponding images of the adaxial and abaxial epidermis in the transverse cross-section plane. Both the adaxial and abaxial epidermis are seen to be composed of a single layer of cells. The adaxial epidermis cells appear as hollow rectangular features with thin cell walls. Each of the cells extends for a distance of ~ 0.1 mm along LD, see surface view in **Fig. 3.8a**; in this surface view, each cell is outlined as a rectangle. The abaxial surface cells appear as irregular tube-like structures in the transverse cross-section of **Fig. 3.8e**. They have thicker cell walls than the adaxial cells. The abaxial cells also extend along LD.

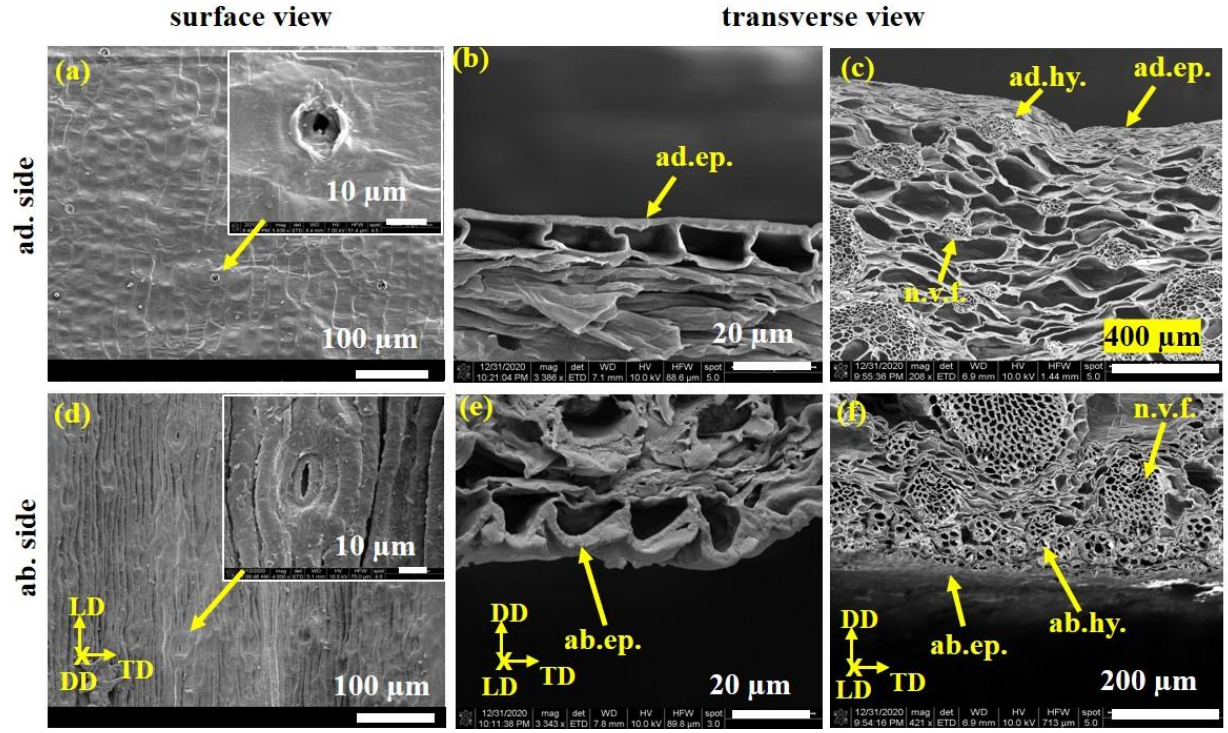

Figure 3.8 SEM images of adaxial (top row) and abaxial (bottom) sides of the sheath and adjoining skin layers. (left column) (a) adaxial and (d) abaxial surfaces showing stomata at higher magnification. (middle column) Structure of (b) adaxial and (e) abaxial epidermis (ep.) that forms the outermost layer of the sheath. (right column) Structure of layer adjacent to epidermis (hypodermis) (c) adaxial and (f) abaxial hypodermis (hy.). nvf stands for non-vascular fiber.

The layer adjoining the epidermis is the hypodermis. The thickness cross-section SEM images in **Figs 3.8c and f** show the adaxial and abaxial hypodermis, respectively, in the transverse plane. The thickness of the adaxial and abaxial hypodermis are ~ 0.1 mm and ~0.2 mm, respectively. The adaxial hypodermis is seen to be composed of compact and densified cells, while the abaxial hypodermis is made up of non-vascular fibers (*nvfs*) grouped together in clusters. The structure of the non-vascular fibers is discussed in greater detail in the ensuing. The higher stiffness/Young's modulus of the abaxial surface, as estimated by nano-indentation, could be a consequence of the thicker cell walls of the abaxial epidermis and/or due to the presence of non-vascular fibers as a cluster in the hypodermis layer immediately below the epidermis layer.

The bulk of the sheath (interior) bounded between the adaxial and abaxial hypodermis is mainly composed of ground tissue and fibers **(Fig 3.7**). The ground tissue in a plant usually refers to all the (other) tissue in that is not dermal tissue or vascular tissue. The ground tissue is made up of irregular, spongy, and porous parenchymatous tissue, with porosity fraction of 0.6 to 0.7. The parenchymatous tissue not only serves as storage space for food and minerals, but also as the matrix in which the fibers (tissue) are embedded.

There are two types of fibrous tissue in the sheath: vascular fiber and non-vascular fiber (*nvf*). Both of these fibers are oriented with their lengths along the LD of sheath. The fiber lengths are typically > 10 mm. The vascular fibers serve two functions: transporting water and minerals via the vascular tube, in this sheath case from the stem to the leaves; and providing for strength via lignified cell walls. The vascular fibers in the sheath have an elliptical cross-section near the abaxial side, but become circular towards the adaxial side **(Fig. 3.7).** The non-vascular fibers provide additional strength to the sheath [14,26]. Typically, the vascular fiber is always lignified whereas the cell wall of non-vascular fibers is variously lignified or sometimes not lignified [14,26]. Based on these observations, we can describe the sheath material as a composite with fiber–matrix type structure in the bulk, bounded by very thin (skin) dermal layers **(Fig 3.7**).

In the lower magnification SEM images (70 ×) of the sheath thickness cross-sections (**Fig. 3.7a** and **b**), only the vascular fibers are clearly visible. The non-vascular fibers are not prominent in these sections since their size is much smaller than the vascular fiber size. The non-vascular fibers (*nvfs)* can however be seen in the higher magnification (400 ×) SEM cross-section images (**Fig.**

3.8). In the matrix, the non-vascular fibers are found to appear individually and isolated from one another (**Fig 3.8c**), while they occur as clusters in the abaxial hypodermis (**Fig 3.8c**).

Fiber size characteristics We now turn to a discussion of fiber size and size-related characteristics. Both vascular and non-vascular fibers are analyzed. We measured the A_f, d_f, λ and S_V of vascular fiber in three different sheaths, with measurements taken at the tip, middle, and base of each sheath, as well as along the center and edge. Here, S_V is perimeter of fiber per unit measured area. All of the parameters are defined in **Sec. 3.4.1** and also are reproduced as part of **Table 3.1** below.

SEM images of transverse plane cross-sections, as in **Fig 3.7a,** were obtained at each of these locations to get the various fiber parameters. The plots in **Fig 3.9** show, for the vascular fibers, the variation of A_f, d_f, λ and S_V of vascular fiber with sheath thickness. The black data points correspond to measurements done at the center of the sheath while the red data points are from the sheath edge. The directions of the arrows in the plots represent the direction of measurement - from the base (thicker part) of the sheath towards the tip of the sheath (thinner part). The average values for A_f, d_f, λ and S_V measured at the center and edge of the sheath, corresponding to **Fig 3.9,** are summarized in **Table 3.1**.

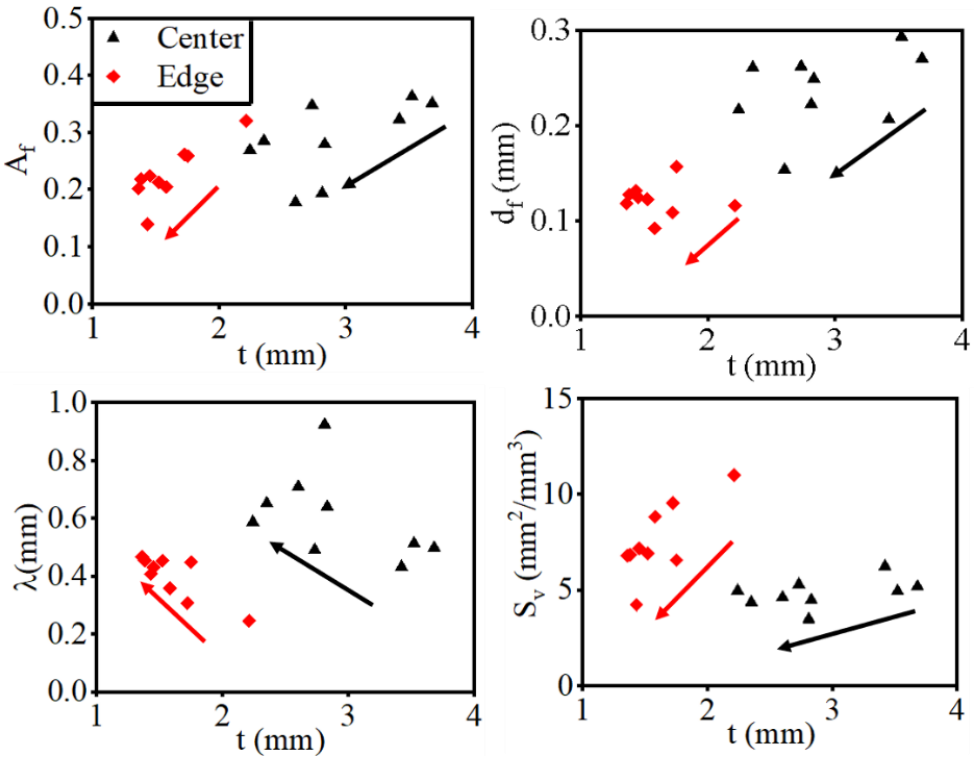

Figure 3.9 Variation of A_f, d_f, λ and S_v of vascular fiber with sheath thickness. The arrows in the plot represent the measurement direction- from base (thicker) of the sheath towards the tip (thinner).

Table 3.1: Average A_f, d_f, λ and S_v measured for vascular fiber at the center and edge of the sheath

Fiber size characteristics	**center**	**edge**
Area fraction of fiber, A_f	0.28±0.06	0.22±0.05
Fiber size, d_f (mm)	0.24±0.04	0.12±0.02
Mean distance between fibers, λ (mm)	0.60±0.14	0.39±0.07
Perimeter of fiber per unit measured area, S_V (mm/mm^2)	4.88±0.75	7.55±1.97

The measurements in **Fig. 3.9** show that A_f, d_f, λ for the vascular fiber are higher at the center of the sheath than at the edge. This tells us that the center of the sheath has larger fibers (dimension in transverse plane) than the edge and also the average spacing between the fibers is greater at the center than at the edge. Also, the area fraction A_f of the fiber is higher at the center then at the edge, suggest that area fraction of matrix $(1 - A_f)$ is higher at the edge (0.78) than at the center (0.72) . The S_V at the edge is higher than at the center. **Figure 3.9** also shows how these vascular

fiber parameters vary from the base towards the tip of the sheath. For example, S_V is highest at the base of the sheath and decreasing towards the tip, while λ increases towards the tip.

Turning to the non-vascular fibers, the cross-sections of *nvfs* found in the matrix in the sheath interior are circular, while near the adaxial side the cross-sections are elliptical. The average size (in transverse plane) of non-vascular fiber is < 0.03 mm and these fibers were found to account for less than 2% of the area fraction in the transverse plane. In contrast, the vascular fibers are much larger in size, 0.12 to 0.24 mm (**Table 3.1 and Fig. 3.9**).

Structure of the fibers As noted, one of the characteristics that distinguishes the vascular fiber from the non-vascular fiber is its size; vascular fibers are > 6 times larger than non-vascular fibers. Structural analysis of vascular (**Fig 3.10**) and non-vascular fibers (**Fig 3.11),** using transverse and longitudinal plane cross-sections (SEM), revealed additional important differences. **Figure 3.10a** shows an SEM image of the surface of a vascular fiber. When this fiber surface is examined at higher magnification along its length, arrays of particles (size ≈10 μm) are seen to be distributed along the length (**Fig 3.10b**). Energy dispersive X-ray spectroscopy (EDX) elemental analysis showed these particles to be Si-rich **(Fig 3.10c)**. The particles serve varied roles, including enhancing the mechanical strength of cells; increasing the abrasiveness of cell walls and reducing attack by various herbivores; and even enhancing the drought resistance of plants in certain cases (e.g., tomato leaves) by increasing the cell wall thickness [27–29].

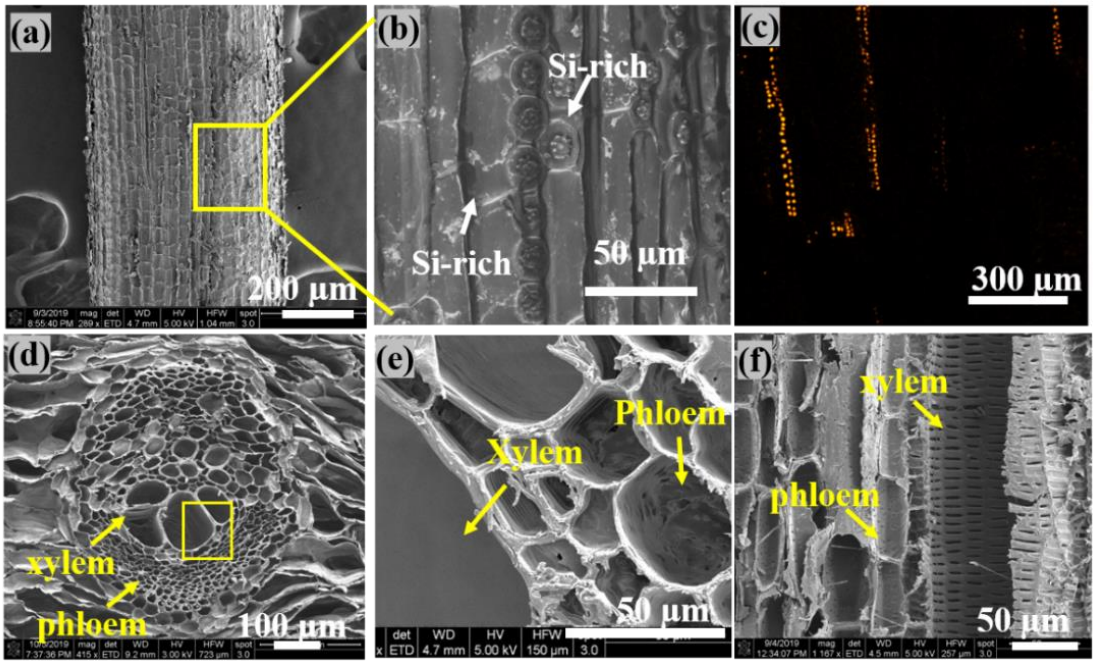

Figure 3.10 SEM images of vascular fiber showing details (a) surface of individual fiber; (b) Enlarged view of fiber surface showing array of particles on the surface. (c) EDX analysis showing particles to be Si-rich. (d) Cross-sections of vascular fiber in the transverse plane showing xylem and phloem, the conducting elements of the vascular bundle; (e) enlarged view of region inside the yellow square in (d) showing details of the xylem and phloem; (f) cross-section of an individual fiber in the longitudinal plane.

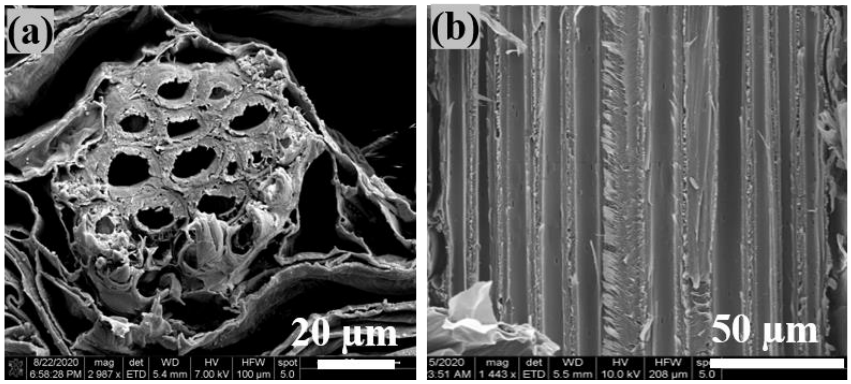

Figure 3.11 Cross-section of non-vascular fiber in a) transverse and b) longitudinal plane.

Fig 3.10d-f show cross-sectional views of vascular fiber in transverse and longitudinal plane. The vascular fibers are seen to consist of two tissues: xylem and phloem. Xylem is responsible for transporting water and other minerals to the plants from the root, while phloem is responsible for transporting food, sugar, and other organic materials prepared by the green parts of the plant to

other parts. Both xylem and phloem are hollow tubes oriented along the length of the vascular fiber. The xylem (length >1 mm, avg. diameter ~ 0.07 mm) are located near the central part of the vascular fiber, and are surrounded by the short- tube phloem (length ~0.10 mm, avg. diameter ~ 0.015 mm). The number of xylem in a fiber is typically 1 to 5. While the xylem is a continuous hollow tube allowing for unidirectional transport, the phloem is made up of shorter tubes known as sieve tubes with cross wall (**Fig. 3.10f**). The flow in the phloem is bidirectional [14,26]. The non-vascular fibers seen in the cross-section views (**Fig 3.11)** consist of multiple hollow tubes of diameter <0.01 mm, orientated along the length direction of fiber. The porosity of the vascular and non-vascular fibers, as measured from the images, are 0.5 to 0.6 and 0.4 to 0.5, respectively.

Density The density of sheath (ρ) was measured on the same sample set as that used for the dimensional study of fiber characteristics. The average densities of the sheath at the center and edge regions were obtained as 0.41 ±0.05 gm-cm^{-3} and 0.34 ±0.04 gm-cm^{-3}, respectively. This is consistent with the fact that center of the sheath has a larger fraction of fiber, and the fibers being typically denser than the matrix**. Figure 3.12** shows the density (ρ) plotted against A_f. Note that the A_f in **Fig 3.12** represent the area fraction of vascular fiber, as non-vascular fiber accounts for only a small fraction and has been neglected. The densities of the individual constituents, namely the fiber (ρ_f) and matrix (ρ_m), are also obtained from the data in this figure. For this estimation, the ρ vs A_f data points in **Fig. 3.12** were fitted with a straight line defined by the rule of mixtures (**Eq. 3.1**). The density of matrix (ρ_m) is first obtained as 0.26±0.05 gm-cm^{-3}, corresponding to the intersection of the fitted straight line with the ρ axis at $A_f = 0$. The density of the fiber (ρ_f) is then obtained as 0.78±0.23 gm-cm^{-3} from the slope of the straight line fit, as $\rho_f = slope + \rho_m$.

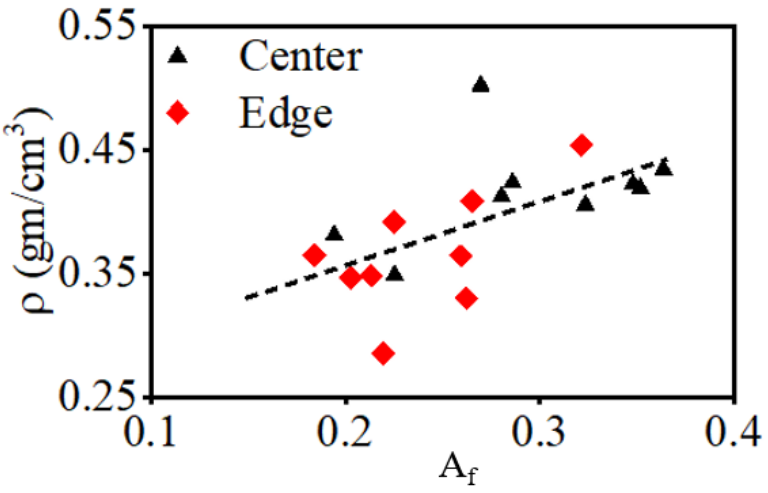

Figure 3.12 Plot of sheath density (ρ) against A_f. From the linear fit of the data points, the density of fiber (ρ_f) and matrix (ρ_m) are obtained as 0.78±0.23 and 0.26±0.05 gm-cm^{-3}, respectively.

3.5 Is the palm sheath a leaf or a stem or a hybrid?

A question of interest is whether the palm sheath material should be considered a leaf or a stem or a hybrid of the two. The characterization of the sheath morphology and anatomical features provides one basis for answering this question. With this question in mind, we compare the morphological and anatomical characteristics of the sheath with those of the areca stem and leaf [14,26].

Morphology Palm leaves typically have a flat and slender shape with length of 0.5 to 2 meters, width < 40 mm near the middle of the leaf, and thickness < 0.3 mm. They are also wider at the base and with a very narrow tip, analogous to the sheath. **Figure 3.13** shows a typical areca palm leaf from a young plant. Like the sheath, the palm leaf is green when young, and turns brown at maturity. The leaf has distinct adaxial and abaxial surfaces with striations oriented along the length direction, see **Fig. 3.13**, like the sheath surfaces. The abaxial surface of the leaf is also darker than the adaxial surface, analogous to the sheath material. Nanoindentation measurements on a young leaf showed both the Young's modulus (stiffness) and hardness of the abaxial side to be much greater than that of the adaxial side, as with the sheath material. Finally, the stomata are more diffusely distributed on the leaf surface compared to the sheath; more stomata occur on the adaxial

surface than the abaxial side in the leaf [14,26,30]. A summary of the morphology characteristics of the leaf are given in the first column of **Table 3.2**, and of the sheath in column 3 of the same table.

In contrast to the flat and slender leaf and sheath, the palm stem is a wood-like cylindrical structure with typical diameter of 25 to 40 cm, and height up to 20 meters. The outer surface of the stem shows radial scars, wherein the mature sheath has separated from the stem (fallen off) at different times [31,32]. the outer surface is also known to be stiffer than the core of the stem [26,33,34].

Based on the morphology (see **Table 3.2**), it is clear that the sheath is qualitatively similar to the leaf, with the exception of size.

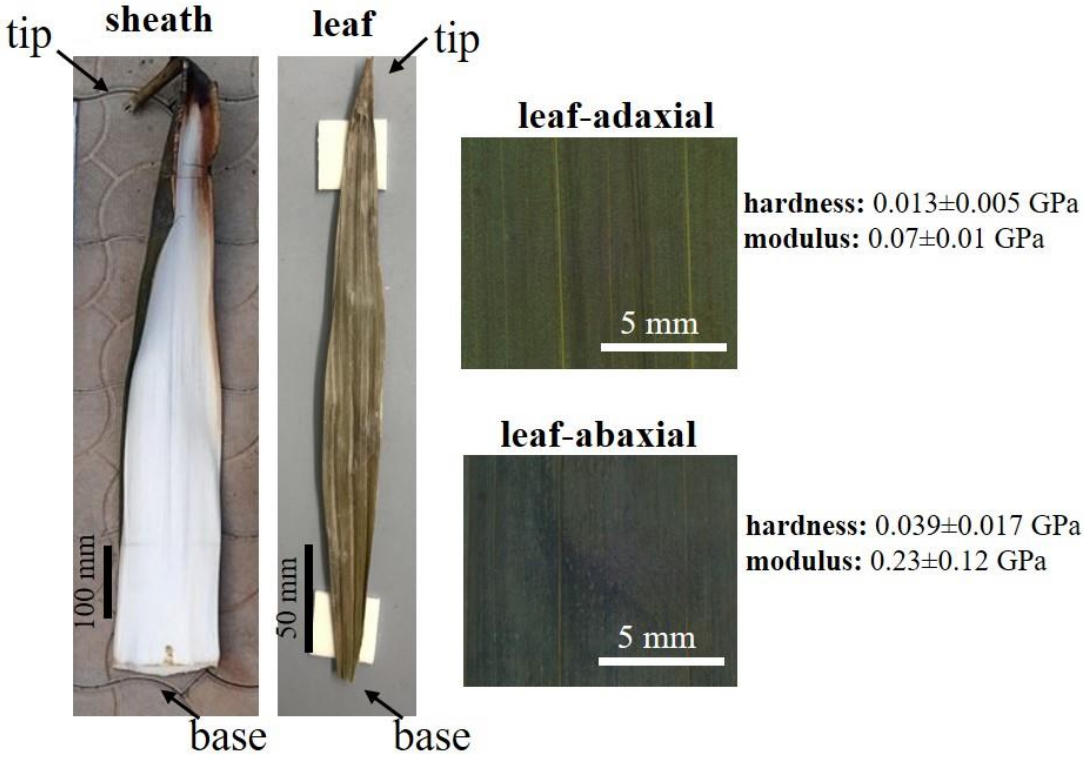

Figure 3.13 Comparison of the morphology of palm sheath and palm leaf. (left) Both the sheath and the leaf are wider at the base and very narrow at the tip. The width is greatest at the center. (right) Adaxial and abaxial surfaces of the leaf showing striations oriented along the length direction. For corresponding images of the sheath abaxial and adaxial surfaces, and striations thereof, see **Fig. 3.4**.

Table 3.2 Summary of the morphological characteristics of leaf, stem and sheath

leaf	stem	sheath	comments
• Flat and slender shape - inner (adaxial) and outer (abaxial) surface. 0.5 to 2 meters, width < 40 mm near the middle of the leaf, and thickness < 0.3 mm • Wider at base, and very narrow at tip; greatest width in the middle. • Abaxial surface darker than adaxial surface. Both surfaces have striations along the length. • Abaxial surface is stiffer and harder than adaxial surface.	• Cylindrical shape with outer surface and inner part • Outer surface is stiffer than central region	• Flat and slender shape - inner (adaxial) and outer (abaxial) surface. 0.3 to 1 meters, width < 0.5 meter near the middle of the leaf, and thickness < 4 mm • Wider base narrow tip, widest at middle. • Abaxial surface darker than adaxial surface. Both surfaces have striations along the sheath length direction. • Abaxial surface stiffer and harder than adaxial surface.	If scale bar is removed (e.g., Fig.3.13), the sheath and leaf look similar to each other.

Anatomical features We have also studied, broadly, the anatomical features of the areca leaf and stem (**Figs 3.14a and b**), and compared their structures with that of the sheath (**Figs. 3.7 and 3.8)**. The areca leaf structure in **Fig. 3.14a** is shown in a transverse cross-section plane, across the leaf thickness. The stem internal structure in **Fig. 3.14b** is shown in a cross-section plane perpendicular to the stem axis, at two locations - near the stem center and close to its outer surface. Both the adaxial and abaxial sides of the areca leaf have a single layer of epidermis and hypodermis. A single ~0.2 mm diameter vascular fiber spans almost the entire thickness of the leaf. The ground tissue consists of polygonal open cells. Non-vascular fibers are occasionally seen on the abaxial side of the leaf [14,26].

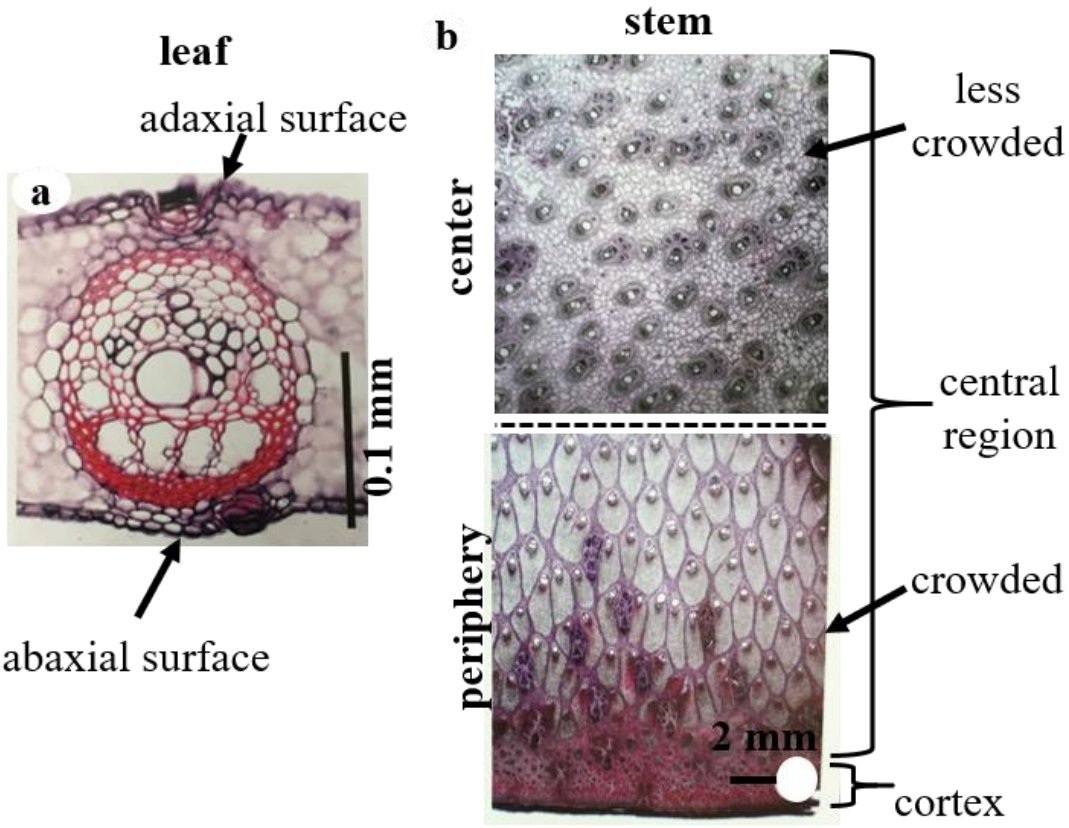

Figure 3.14 Internal structure of (a) areca leaf in transverse plane (thickness cross-section) and (b) areca stem in cross-section plane perpendicular to the axis of the stem (ref: Tomlinson [26], permission obtained).

The stem shows three distinct regions in terms of structure: the outer (surface) epidermis, the cortex, and a central region, which is divided into a crowded region towards its periphery and a less crowded region near its center. At the outer surface, the epidermis is a single-layer structure with a narrow cortex forming a layer adjacent to the inner side of the epidermis. The cortex consists of non-vascular fibers similar to the hypodermis of the sheath. The region on inner side of the cortex consists of ground tissue and fibers (vascular and non-vascular). The ground tissue of the stem is composed of open and polygonal cells. Vascular fibers can be seen in **Fig 3.14b -** near the center of the stem, the vascular fibers are circular and sparsely distributed in the matrix; while they are more elliptical in shape and crowded near the stem periphery. The average size of the vascular fiber ranges from 0.5 to 2 mm. The principal details of the anatomical features of the sheath, stem

and leaf are summarized in **Table 3.3**, along with a comparative assessment of the features in the last column of the table.

Table 3.3 Summary of the anatomical characteristics of leaf, stem and sheath

leaf	stem	sheath	comments
• Single layer epidermis on both adaxial and abaxial surface • Stomata present on both the outer surfaces, more on abaxial than adaxial surface	• Single layer epidermis on outer surfaces • Stomata present on outer surfaces.	• Single layer epidermis on both outer surfaces • Stomata present on outer surfaces, more on abaxial than adaxial surface	• Epidermis and stomata are similar in leaf, sheath and stem
• Single layer hypodermis on both abaxial and adaxial surface	• Multilayered cortex adjoining outer surface, cortex is equivalent to hypodermis layer of sheath.	• Multilayered hypodermis on both adaxial and abaxial surface	• Hypodermis of both sheath and stem are similar (multilayer) while in leaf it is single layer.
• One vascular fiber across the entire thickness (dia ~ 0.1 mm).	• Many vascular fibers across stem cross-section (dia ~ 0.5 to 2mm) • Vascular fibers are circular near center. Elliptical and more crowded in peripheral region.	• Many vascular fibers in thickness section (dia~ 0.25 mm) • Vascular fibers circular near addax surface. Elliptical and more crowded near abaxial side.	• Vascular fibers and distribution similar in stem and sheath. Much different in leaf.
• Non-vascular fiber absent within ground tissue. Occasionally, few of these fibers seen near abaxial hypodermis.	• Non- vascular fibers smaller as compared to vascular fibers. Distributed within ground tissue as a single fiber and seen as a clustered in cortex	• Non-vascular fibers much smaller compared to vascular fibers. *nvfs* distributed within ground tissue as single fibers, but clustered in abaxial hypodermis	• Similarity in non-vascular fibers between stem and sheath.

A comparison of the anatomy of the stem with that of the sheath shows that the stem has epidermis at the outer surface only whereas sheath has epidermis on both adaxial and abaxial sides. Unlike the open cells in the matrix of stem, the cells in the matrix of the sheath appear to be compressed between two outer surfaces. With regard to the vascular fibers - their distribution (less crowded to more crowded) and shape variation (circular to elliptical) as one moves from the center of the stem to the peripheral region are both similar to the corresponding variations seen in the sheath as one proceeds from the adaxial to abaxial surface. Also, similar to the abaxial hypodermis of the sheath, the cortex of the stem is made up of clusters of non-vascular fibers. The cortex of the stem may thus be taken to analogous to the sheath hypodermis. The leaf internal structure does not show much correspondence with that of the sheath.

In summary – from a morphology standpoint, the sheath has commonality in features with the leaf. However, with respect to anatomical features, especially considering distribution and shape of vascular fiber, and structure of cortex and epidermis, the sheath more closely resembles the stem. It would appear therefore that the sheath can be structurally considered as a hybrid of the stem and the leaf. While serving as a physical link between the stem and the leaf (**Fig.3.1**), the sheath appears to have also adopted the morphology of the leaf and the anatomy of the stem.

3.6 Discussion

Our characterization of the structure of the areca palm sheath at various length scales has provided a detailed picture of the external (morphology) and internal (anatomy) features of the sheath. In its early stage, the areca sheath resembles a closed tube. It subsequently grows into a long flat (slender) structure that partially covers the stem at the base and merges into the leaf at its tip. The sheath is initially green, similar to a leaf, and then turns brown (matures) with age. The sheath is thicker at the base and gradually thins toward the tip. The center of the sheath is also thicker than the edge. The areca sheath is like a sandwich structure with distinct adaxial and abaxial (darker) outer sides, and a bulk interior composed of matrix and fibers. The thin outer epidermis layers on both the adaxial and abaxial sides are stiffer and support the internal (bulk) material. Both the adaxial and abaxial surfaces have striations, which are the main source of surface roughness in the sheath. The roughness on the abaxial surface is quite uniform throughout its length, whereas the roughness on the adaxial surface is greater at the center of the sheath than at the edge.

The areca palm sheath has a hierarchical anatomical structure that is similar to that of other palm species and plant materials such as bamboo [35–37] **.** As in a directional fiber-reinforced composite material, the fibers are oriented along the length direction of the sheath and distributed in the matrix. There are two types of fibers – vascular and non-vascular, as with other palm species. The vascular fibers are of closed type and composed of the xylem and phloem. The vascular fibers are distributed uniformly in the bulk of the matrix, but more crowded near the abaxial side than the adaxial side. They also show a change in shape – from elliptical near the abaxial side to circular in the bulk of the sheath and the adaxial side. The non-vascular fibers are sparsely distributed in the matrix and also non-uniformly. These fibers are more crowded in the region adjoining the abaxial epidermis; this region constitutes the abaxial hypodermis.

The area fraction of vascular fiber varies from 20% to 35%; it is higher at the center and smaller along the edges of the sheath. Thicker sheaths have larger vascular fibers and higher fiber fractions. For comparison, the fiber area fraction in oil palm stems and meso bamboo is 25–50% and 30–70%, respectively. Hence, the areca sheath has a larger matrix fraction (65-80%) than the oil palm or the meso bamboo stem. It also has a larger fraction of matrix than the areca stem and leaf (<50%). The density of sheath (ρ) varies between 0.25 and 0.45 gm-cm^{-3}, increasing with fiber fraction. This type of density change indicates that the fiber is denser than the matrix; in fact, the density of the fiber is predicted to be three times that of the matrix. The porosity in areca sheath is 0.6 to 0.7. This falls midway between that of balsa wood (0.95, very high porosity) to 0.12 in lignum vitae (guayacan) representing a low porosity [33,38]. Bamboo wood, one of the most widely used structural plant materials, has a porosity in the range of 0.3–0.7 [35,36,39]. The area fraction of fiber, as well as the density of stem and leaf, are greater than those of the sheath. The higher density of stem and leaf is most likely due to the higher fiber volume fractions therein.

A qualitative comparison of the sheath structure with that of the leaf and stem has revealed that the sheath is closer to the leaf, morphologically, and to the stem, anatomically. In the literature, the sheath has sometimes been referred to as palm-leaf perhaps based on the morphological similarities. Also, commercially, foodware products made from the sheath are commonly referred to as palm-leaf products. As we have seen, sheath morphological characteristics such as its flat and slender shape, with wider base tapering off to a narrow tip; distinct adaxial and abaxial surfaces with striations; color changes from green to brown with age, all show similarity with those of the leaf. On the other hand, key anatomical characteristics such as distribution and shape of fibers, and structure of cortex, show qualitative similarity with those of the stem. The similarity of fiber distribution at the center of the stem to the adaxial side of the sheath, the periphery of the stem to the abaxial side of the sheath, and the cortex of the stem to the abaxial hypodermis of the sheath, also suggest that the central part of the stem could have grown to become the adaxial side of the sheath and the outer part of the stem to become the abaxial side of the sheath. This type of growth is consistent with the physical placement of the sheath in the tree, being an outgrowth from the stem [14,26,32].

The structural analysis strongly suggests that the sheath structure is intermediate between that of the leaf and the stem. Hence, it may be appropriate to consider the sheath as a hybrid of the leaf and the stem, and not as leaf-sheath.

3.7 Conclusion

Sheath morphology and anatomical features have been studied at different length scales using imaging techniques such as optical microscopy, profilometry and SEM. The sheath is green and slender at an early stage, but turns brown at maturity. The sheath has two distinct outer surfaces - adaxial and abaxial surfaces – marked by striations that run along the sheath length. The sheath has an internal structure that is composed of fibers distributed in a matrix. This bulk material is supported by a thin and stiffer epidermis on the outside. The sheath material resembles a sandwiched, unidirectional fiber-reinforced composite. The similarity of the sheath morphology to that of the leaf, and of the sheath anatomy to that of the stem, suggests that the sheath should be considered a hybrid of the leaf and stem from a structural viewpoint, and not as a palm-leaf.

4. MECHANICAL BEHAVIOR AND FORMABILITY OF SHEATH

4.1 Abstract

The proliferation of single-use plastics has stimulated interest in sustainable material substitutes with sufficient ductility and structural integrity. Herein, the mechanical behavior and formability of the leaf sheath from palm species—*Areca catechu*—and its immense potential for manufacturing of eco-friendly food packaging are reported on. Using microstructural analyses and under different loading conditions such as tensile test, compression test and rolling it is shown that this leaf can accommodate forming strains as large as 200%, similar to ductile metals. The sheath deformation response is highly sensitive to hydration, with up to 400% increase in forming strain. Mapping the initial configuration of the sheath to the final product, forming strain in existing commercial foodware product such as plates and bowls are calculated. The results establish the microstructure basis for the formability and the contours of a forming limit diagram that delineates product shapes that can be formed in a single step from this plant material.

4.2 Introduction

From a scientific standpoint, perhaps the most intriguing aspect of the areca palm sheath is its capacity for shape change, i.e., formability, which resembles that of ductile metals like aluminum or copper. Strength and formability are the two key property attributes of a structural material for product design and manufacturing. While strength is critical for structural integrity, and often widely recognized as a mechanical property attribute, the less-recognized formability is what determines whether a material can be manufactured sustainably and in a variety of shapes.

In this chapter, we study the mechanical deformation response of areca palm sheath in different loading conditions, such as tensile test, compression and rolling. We construct a picture of the sheath formability for these loading conditions, that is complemented by an evaluation of stretch formability in the next chapter. We also obtain an assessment of formability based on the deformation of surface topographical features. Lastly, we estimate the strain in commercially available products such as plate and bowl by shape mapping. The analyses also highlight the capability of areca sheath to withstand large strains, sometimes as large as 2 prior to failure. Some insight is obtained into how such large strains are accommodated. The high formability, together

with other intriguing aspects of the mechanical response of areca sheath, suggest opportunities for use of palm tree materials in eco-friendly food packaging, and for unlocking the sustainable manufacturing potential of various plant-based materials.

4.3 Method

4.3.1 Deformation response: mechanical properties and formability

The deformation response of areca sheath was studied using multiple mechanical loading tests — tension, compression, and rolling. These provide comprehensive information about strength, ductility and formability; and of anisotropy in deformation response. Additionally, observations of deformed microstructure constituents reveal how macroscopic shape changes are accommodated at the micro-scale. The loading configurations capture key features of the forming processes (e.g., punching, stretching and compression) relevant to product manufacturing.

Uniaxial tensile testing was performed (MTS tensile tester, 2kN capacity) to obtain stress strain-curves, as well as strength, Young's modulus and uniform elongation of the sheath. Test samples were in the form of rectangular strips of dimension 35 mm×2 mm×sheath thickness (~3 mm), and were cut from the central region of a sheath in the LD-TD plane. Special loading grips for the sample were prepared by casting a coldmount acrylic resin (LECOSET 100) around the sample ends. The casting was one part of liquid monomer and two parts of resin polymer powder, the mixture being allowed to air-cure around the sample ends for 24 hours. Each grip was approximately 10 mm in length × 10 mm in width × 7 mm in thickness. This type of grip ensured correct clamping of the sample in the machine jaws, without any slippage or sample failure at the grips during loading. The sample gauge length was maintained at 15 mm and tests were conducted in displacement control mode with cross-head speed of 1 mm/minute (strain rate ~ 10^{-3}/s). The gauge displacement was measured in two different ways — from the cross-head motion, and via digital image correlation (DIC) using markers imprinted at the ends of the gauge length. Both measurements were in very close agreement; the strain data reported is that obtained from the cross-head displacement. From the load-displacement measurements, an engineering stress-strain curve was computed along with properties like strength, uniform elongation (ductility) and Young's modulus. The effects of anisotropy and water exposure (hydration) were evaluated by

testing sheath samples cut at different orientations to the longitudinal direction (LD), and samples that had been submerged in water for 2 h and 12 h prior to the testing, respectively.

Sheath formability in the dry condition was examined in two different ways: via uniaxial compression, and plane-strain rolling.

Uniaxial compression response was studied by loading the sheath (dry condition) parallel to the depth direction (DD) between steel platens. Test samples (5 mm× 5 mm × ~ 3 mm thickness) were compressed to 25%, 50% and 70% of their initial thickness. The deformation of the principal sheath microstructure constituents, viz., fibers, pores and matrix, was quantified by SEM observations of sample cross-sections in the transverse plane. Since individual fibers are typically >50 mm in length, it was possible to track deformation of specific fibers (markers) in the SEM images by compressing multiple samples cut out from the same sheath to varying reduction strains (each sample with dimension 5 mm in the fiber length direction).

Rolling response was studied using rectangular sheet samples 30 mm length × 10 mm width × ~ 3 mm thickness, cut out of the central portion of the sheath, and then dry-rolled parallel to LD and TD orientations in a rolling mill with steel rolls of 100 mm diameter. Rolling was done in incremental steps of 0.3 mm thickness reduction until failure. The length of the sample was kept parallel to the rolling direction, and the sample thickness was equal to the sheath thickness, so that the abaxial and adaxial surfaces of the sheath comprised the surfaces in contact with the rolls. The thickness strain imposed in the material was calculated as $ln\left(\frac{1}{1-r}\right) = ln\frac{t_i}{t_f}$, for no change in the dimension along width direction. Here t_i and t_f are initial and final thickness of the sheath sample, respectively, and r the reduction ratio. After each incremental reduction, the rolled samples were examined under the optical microscope to identify onset of cracking and the failure mode. The formability was quantified in terms of the strain to failure in the TD and LD orientations.

Surface topography analysis provided another complementary estimation of the formability, in terms of a local (surface) deformation strain. This was obtained based on measurement of changes in height and width of the surface striations in the sheath due to the rolling. These dimension changes were derived from measurements of surface topography, made on the rolled surfaces, after each incremental thickness reduction. Surface topography on the unformed sheath, rolled samples, and formed surfaces of plates and bowls, was characterized using a stylus profilometer (Rank

Taylor-Hobson Talysurf), by making line profiles in the transverse direction and across the striations (sample lay). The sampling length for each profile was 10 mm. The topography is reported in terms of the actual profiles over the sampling length, and as the roughness parameter R_z. The topography measurements provided a direct measure of surface roughness evolution (finish) in a typical forming process, a key quality parameter in product manufacturing. It also provided a characterization of formability based on local deformation data obtained from changes in surface profile heights.

4.3.2 Shape mapping of formed products

The strain imposed in the foodware forming process was directly estimated from measurements of shape change occurring in processing of sheath into plates and bowls. For this purpose, a special method was developed to map product shapes and displacements.

We considered two geometries – plates (circular) and bowls (elliptical) – made from sheaths (see **Fig. 1.2**). The plate has a circular flat-bottomed surface in the middle (diameter ~ 150 mm) and a straight slanted surface at the periphery. The outer diameter and depth of the plate are ~ 220 mm and 30 mm, respectively. In contrast, bowls are elliptical in plan-view and lack a central flat region. The minor and major axes (diameters) of a bowl are ~140 mm and ~160 mm, respectively, with its height changing gradually from the center (bottom) to the periphery by a vertical distance of 30 mm. The minor and major axes in a bowl are parallel and perpendicular to the striations, respectively.

Macroscopic details of the forming process were first established using measurements of sheath thickness in the *z*-direction, before and after the deformation. In a typical process, sheath of initial thickness H is formed by a punching/stretching process (see **Fig. 2.1**) into a plate/bowl with wall thickness $h \sim 0.8\,H$. The thickness values H and h were directly measured at multiple locations on the sheath and plate/bowl, respectively. The standard deviation on measured thickness was < 10%. These thickness values are input data needed for estimating the strain in the bowls and plates.

Next, the final shapes of the plate and bowl samples were mapped using an imaging technique, see **Fig. 4.1**. Each sample was first filled with a colored liquid to a known depth (z_0) and then imaged from above. The sample adaxial surface was coated with a layer of thin plastic sheet to prevent

water from seeping into the sheath. By tracing the boundary of the liquid, the loci of points at constant z_0 from the bottom were determined. This procedure was repeated for various z_0 values; by collating the results, an accurate 3D representation of the sample was obtained. For the imaging, a camera was placed vertically above the center of the sample. The origin ($x = y = z = 0$) was fixed at the center of the sample, on the adaxial surface. The x and y axes were taken parallel to LD and TD, respectively (**Fig. 4.1**), while the z-axis was perpendicular to the adaxial surface and coincided with the optical axis of the camera. The resolution of this representation is determined only by the height intervals at which the measurements are made; in the present study, this height interval was 1 mm. Digitized images were then analyzed using ImageJ to obtain the x and y coordinates of the pixels at the liquid-sample boundary. These pixel coordinates were then transformed into actual distances from the origin as $x = \alpha(i - i_0)$ & $y = \beta(j - j_0)$. Here, (i, j) and (i_0, j_0) are pixel coordinates of the surface and center points respectively; and α and β represent the pixel scale (mm per pixel) in the x and y directions, respectively. The strain field at every point on the plate or bowl surface is then derived from this shape data.

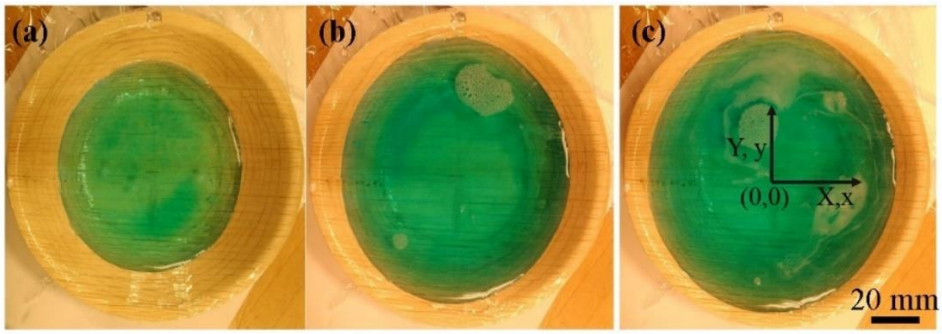

Figure 4.1**.** Imaging technique used for constructing the 3D shape of a bowl. The bowl is filled with colored liquid to different heights as measured from the inner surface a) 2 mm, b) 10 mm and c) 28 mm. The contours of the liquid are mapped at the various heights and then collated to obtain the bowl shape. The z-axis is perpendicular to the inner surface at the center, while x- and y- axes are parallel (LD) and perpendicular (TD) to the striations, respectively.

4.4 Results

4.4.1 Deformation response

The deformation response of the sheath at room temperature, under the various loading modes, has provided a characterization of the large strains (shape changes) that the sheath can accommodate and the underlying pathways.

Uniaxial tension The uniaxial tensile stress-strain response of the sheath in LD and TD orientations is shown in **Fig. 4.2,** in both dry and wet conditions. In the dry condition, the tensile strength of the sheath (maximum stress) is ~ 32 MPa, and the Young's modulus is ~ 780 MPa, in the LD orientation. The corresponding values for TD are considerably smaller, only 2 MPa and 30 MPa, respectively.

The uniform elongation strain (strain at peak stress) is ~ 4% for the LD and ~ 7% for the TD; although not all of this strain is plastic strain, it nevertheless provides a useful measure of ductility/formability. This strain is greatly increased in the wet condition, with LD strain doubling to 8% and TD strain increasing by more than four-fold to 35%. For reference, the corresponding true (logarithmic) strains in the dry condition are 4% and 7% in the LD and TD directions, respectively; and 8% and 30% in the wet condition. While the sheath strength in both LD and TD directions is reduced by the hydration, this is more than offset from a deformation processing standpoint by the corresponding gain in ductility, see **Fig. 4.2**. The TD ductility is much greater than the LD ductility in both dry and wet conditions. The mechanical properties are thus strongly anisotropic and quite sensitive to the hydration condition, akin to many woods [40,41].

From a forming perspective, the strain response is a more critical parameter since it directly encodes dimensional changes. The TD tensile ductility of ~ 35% in the wet condition is very similar to that of metals like Al and Cu [42–45]. While the material strength plays a key role in determining the forming process requirements, in the present case, even the higher LD strength values of ~ 32 MPa are quite small, as to be of little consequence for the forming both in terms of energy consumption and equipment design specifications. The stress-strain data thus strongly suggest that larger shape changes can be achieved in the wet condition, and that a 2-hour exposure is more than sufficient to obtain the requisite formability gain. This is consistent with what is done in practice, where the sheath material is submerged in water, albeit for a longer period of 12 hours, prior to the forming. During the 2-hour and 12-hour exposure, water content in the sheath increased by ~0.15 gm/cm^2 and ~ 0.25 gm/cm^2 respectively, as estimated using mass gain measurements.

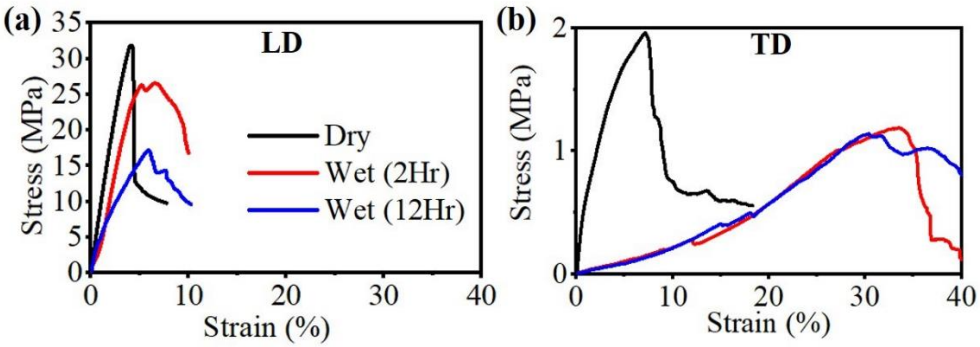

Figure 4.2 Stress-strain curves for areca sheath loaded in uniaxial tension in (a) longitudinal (LD) and (b) transverse (TD) directions. Results are shown for both dry and hydrated conditions. The peak stress is taken as the strength, and strain corresponding to this peak as measure of uniform elongation (ductility/formability).

Uniaxial compression The sheath material, in the dry condition, was found to withstand much greater strain prior to failure (formability) when loaded in compression than in the corresponding than in the uniaxial tension case. This compression was applied parallel to the depth direction (DD). The samples typically failed at a thickness reduction of ~ 70%, corresponding to an axial strain $\varepsilon = -ln(1/0.3) = 1.2$.

Fig. 4.3a-c show SEM images of typical sheath cross-sections in the DD-TD plane after various thickness reductions in the range of 0-50% (= 0 to 0.7). By tracking both the deformation of individual (specific) fibers and changes in porosity (matrix/fiber), using the cross-section images, it was possible to reconstruct a picture of how the compression strain was accommodated.

Firstly, we tracked deformation of specific fibers at various stages of the deformation; two of these fibers are outlined in red and yellow in **Fig. 4.3**. A change in shape and cross-section of the fibers is evident, especially beyond 25% reduction. With increasing deformation, the fiber cross-sections are reduced, and the "minor axes" of the deformed fibers tend to align parallel to DD. This type of fiber deformation is also observed in compression tests with structural composites [46].

Secondly, the porosity decreases significantly with increasing thickness reduction. The table in **Fig. 4.3** gives the fraction of porosity and solid material after 25% and 50% reduction, as measured by analysis of the SEM cross-section images. Up to this 50% reduction, there was negligible change in the in-plane dimensions of the sample. It is clear from the table that the initial 25% reduction is accommodated mostly by pore size (and volume) reduction, mainly in the matrix. The

fiber porosity shows negligible change, consistent with the very small level of deformation seen in individual fibers (**Fig. 4.3**). However, subsequent reduction to 50% thickness lowers the area (volume) of both the pores and solid region, accompanied by a reduction in porosity in both the matrix and the fibers. Thirdly, at 70% reduction (compression $\varepsilon = 1.2$), all the pores in the matrix and fiber have mostly collapsed; compression beyond 70% typically resulted in sample failure in the matrix, with the fibers separating in the TD orientation perpendicular to the loading axis.

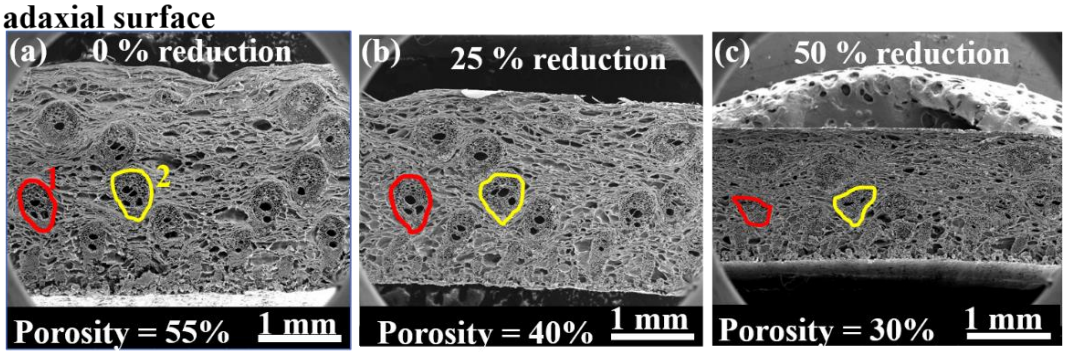

Thickness Reduction (%)	Total area	Pore area	Solid area
0	A	0.55 A	0.45 A
25	0.75 A	0.3 A	0.45 A
50	0.5 A	0.15 A	0.35 A

Figure 4.3 Structure of deformed sheath after various reductions in uniaxial compression, revealed by SEM crosssection images: (a) before compression; and after (b) 25% and (c) 50 % reduction. The images also highlight deformation of two specific fibers 1 and 2, whose outlines are delineated in the cross-section. The compression was applied parallel to DD in the sheath thickness direction. Table below gives area fraction of pores obtained from analysis of SEM cross-section images for various compression reductions (sheath cross-section area before deformation is designated as A).

Rolling The rolling test, wherein a dry areca sheath was deformed in both LD and TD orientations, further confirmed the high formability. This test provided two independent measures of the strain to failure, one based on bulk deformation (thickness reduction) of the rolled sample, and the second from local deformation of striations on the sheath surface, see **Fig. 4.4**. The surface deformation was inferred from profilometric traces across the striations **(Fig. 4.4a)** for a 50% (bulk) sheath thickness reduction. The peak-to-valley height (R_z) on the sheath adaxial surface is seen to decrease significantly, after the reduction, from a R_z of $\sim 400\ \mu$m to $\sim 80\ \mu$m, for the LD rolling orientation, mainly due to flattening of the striations. This translates to a local (surface) rolling

strain of $\varepsilon \sim ln(400/80) = 1.6$. The local strain in the sample rolled in the TD direction is essentially the same, since the profile height decrease is very similar to that in the LD sample (**Fig. 4.4b**).

The variation of rolling strain with r in the bulk of the sheath is shown by the red curve in **Fig. 4.4b**. This is a plot of $\varepsilon = \ln\left(\frac{1}{1-r}\right)$ vs reduction (r) and the individual points are the mean values (error bars +/− one std. dev.), up and until just before the final failure. When rolled parallel to LD, the sheath typically failed at r = 80 to 85%, i.e., a strain of 1.6 to 1.9. The rightmost point on the rolling curve in **Fig. 4.4b** represents the strain point just before failure. An example of a failed sheath for this rolling orientation is shown in the optical micrograph in **Fig. 4.4c**. The fracture is seen to run parallel to the rolling direction with very little deviation, and the fibers adjacent to the fracture surface separate in the transverse direction. Interestingly, this bulk failure value is similar to the local surface of 1.9. The sheath failed at a lower of ~ 1.2 (thickness reduction ~ 70%) when the rolling was done parallel to TD (**Fig. 4.4d**). In this case, the failure is coincident with occurrence of a gross wrinkling instability, with fibers again separating along TD; note also the large change in sample length in this case. These results also highlight strong anisotropy in sheath deformation in the LD-TD plane, consistent with the anisotropy observed in the sheath structure (see **Fig. 3.7**) and uniaxial tension test. The topography of the sheath abaxial surface was negligibly affected by the rolling (hence only initial profile shown in **Fig. 4.4a**), indicating minimal local straining of material on this surface.

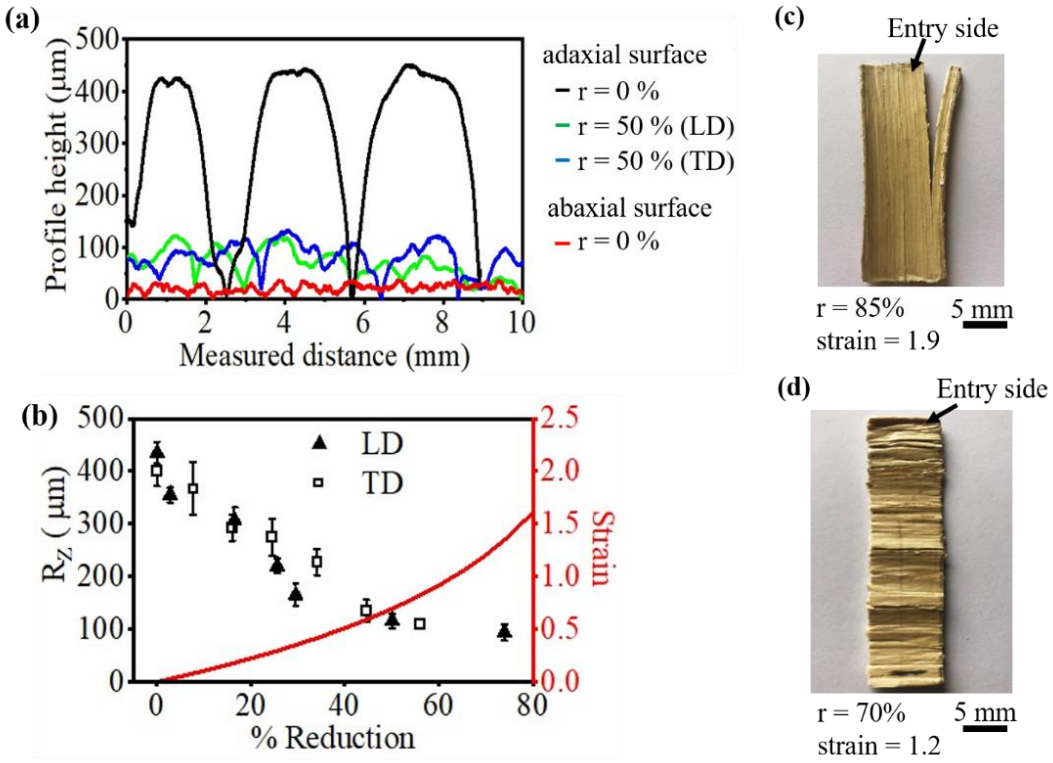

Figure 4.4 Deformation of sheath in rolling and sheath failure: (Left) (a) Surface profiles of adaxial and abaxial surfaces after 0% and 50% thickness reduction; these are used to analyze local surface deformation. The profile of abaxial surface is shown only for the initial sheath as it remained unaffected by the rolling. (b) Variation of peak-to-valley height R_Z on adaxial surface (left axis) and bulk rolling strain (red curve, right axis) with thickness reduction (r). LD and TD denote rolling parallel to longitudinal and transverse directions, respectively. (Right) Optical microscope pictures showing failure of sheath sample in rolling: (c) fracture in LD rolling, and (d) wrinkling in TD rolling. The initial sample length was 30 mm in both cases; note the significant length change in the TD rolling.

4.4.2 Deformation strain in formed products

The strain imposed in the forming of plates and bowls can also be directly estimated by idealizing the forming process as one of biaxial stretching, see **Fig. 2.1** [47–51]. For this estimation, we need the initial (sheath) and final (product) configurations of the sample and, a model for the deformation that maps material points from initial to final state. The latter, in the present stretching problem, is determined principally by contact friction conditions at the die-sheath interface. Resolution of this friction condition, as also in the LDH test, requires measurements of deformation at various locations on the sheath. Since such measurements are not currently available, we consider two extreme cases of these contact boundary conditions – zero friction (frictionless) and high friction

(sticking, or no slip tangential to die face) – to estimate the forming strain. This approach provides characterization of limits to the forming strain, as has been demonstrated in sheet metal stretching [47]. For analysis of the strain limits, we assume the initial state of the sample, the raw sheath, to be a flat disc of thickness H, neglecting any intrinsic variations in sheath thickness and curvature. The final state of the sample (plate/bowl) is obtained using the 3D shape reconstruction technique described in **Fig. 4.1**. **Figure 4.5a and b** show an example of this reconstruction for a bowl.

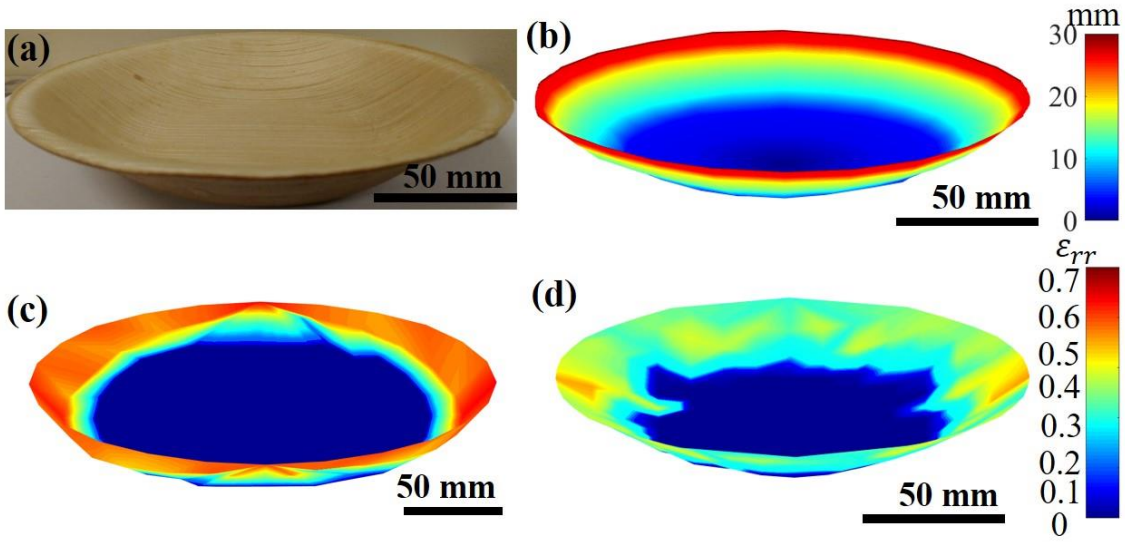

Figure 4.5 Strain distribution in plate and bowl: (a) Optical image of bowl, and (b) bowl-shape reconstruction (see Materials and Methods) used for strain estimation (Scale bar defines height contours with respect to the base). Radial strain (ε_{rr}) contours in (c) plate and (d) bowl.

High friction (no-slip) case If there is no slip tangential to the die interface, then material points are displaced only along the die axis (z-direction) during the punching (**Fig. 2.1**). The material points then map as: $x = X, y = Y$ and $z = cZ + f(X,Y)$, where (X,Y,Z) and (x,y,z) represent coordinates in undeformed and deformed configurations, respectively (**Fig. 4.1**). The origin is taken at the center of the bowl/plate adaxial-surface. The parameter $c = h/H$, is the fractional compression in the z −direction; in the forming of the bowls and plates, $c = 0.8$. The Lagrangian (Green) strain (ε), radial strain (ε_{rr}) and circumferential strain $(\varepsilon_{\theta\theta})$ are calculated using the measured shape, deformation mapping and standard coordinate transformation formulae [52].

The radial strain distribution (ε_{rr}) is shown in **Fig. 4.5** for the plate and bowl. In the plate (**Fig. 4.5c)** the maximum radial strain is ~ 0.7 and occurs at the slant surface along the periphery,

whereas the strain in the central region is zero due to the high friction (no-slip). The radial stretching at the slant surface is related to the angle that this surface makes with the *z*-axis, with the strain increasing with increasing slant angle. A similar radial strain distribution is seen in the bowl (**Fig. 4.5d**), with the maximum radial strain ~ 0.5 again occurring again at the periphery. This maximum strain value is smaller than in the plate because the bowl periphery is not as steeply inclined as the slant surface of the plate. Also, because the plate is axially symmetric, the radial strain in **Fig. 4.5c** is independent of θ; whereas in the bowl, due to its somewhat elliptical shape, there is a θ dependence of this strain (**Fig. 4.5d**), with the strain values being greater along the longitudinal axis compared to the transverse axis. With regard to the other two strains $\varepsilon_{\theta\theta}$ is zero for this case since material displacement is purely in the *z*-direction; and ε_{zz} is constant throughout the sample, due to the homogenous compression imposed by the die. Specifically, $\varepsilon_{zz} = |c^2 - 1| = 0.36$

Frictionless case The deformation strain for the frictionless case may be obtained by considering uniform stretching and bending of the sheath [53]. We denote the initial radius of the undeformed sheath by R_0, and the final radius in the deformed product by R. The latter is the radius of a circle with the same surface area as the final deformed shape. The total strain can then be written as:

$$\varepsilon_{\alpha\beta} = \gamma_{\alpha\beta} + \frac{h}{2}\kappa_{\alpha\beta} \tag{4.1}$$

where $\gamma_{\alpha\beta}$ is the uniform stretching component of the strain, $\kappa_{\alpha\beta}$ is the curvature tensor and the second term in the equation is the bending strain. The strain due to uniform stretching, $\varepsilon_{rr} = \varepsilon_{\theta\theta} = \ln(R/R_0)$, is calculated as 0.10 and 0.11, respectively, for the plate and bowl. The bending strain has a maximum value of 0.05. Together, the total strain is ~ 0.15. This compares well with Hill's solution for bulging of a circular sheet [54], $\varepsilon = \ln(1 + (2h/d)^2)$, which gives the maximum strain in the plate and bowl as 0.11 and 0.16, respectively. Here, h is the depth, and d is the diameter of the foodware corresponding to its periphery. The solution applies to isotropic materials, and for small sheath thickness to diameter (d) ratios (diaphragm case) when shear and bending stresses can be neglected.

The permanent deformation in the sheath is not volume conserving, unlike metals. The ratio of the final volume (product) to the initial volume (raw sheath) in the above forming is c. Since both the matrix and fibers have significant porosity, the permanent deformation is accommodated by pore

closure and significant volume change. We have already seen evidence of this type of structural accommodation in compression (**Fig. 4.3**).

4.4.3 Summary of deformation data and forming limits

The strains realized in tension, compression, rolling and sheath forming processes are summarized in **Table 4. 1**, and provide a characterization of sheath formability.

Table 4.1 Formability summary: failure strains in various loading conditions.

Test	**Loading**	**Dry**	**Wet**
Tensile	uniaxial	0.04 (LD) 0.07 (TD)	0.08 (LD) 0.35 (TD)
Compression	uniaxial	1.2 (DD)	1.2 (DD)
Rolling	plane strain compression	bulk strain (from thickness) 1.9 (LD) 1.2 (TD)	
		local strain (surface profile) 1.6 (LD) 1.6 (TD)	
Foodware	biaxial stretching no slip		Plate: 0.70
			Bowl: 0.50
	biaxial stretching zero-friction		Plate: 0.15
			Bowl: 0.16

4.5 Discussion

Our multi-pronged characterization of the deformation response of areca palm sheath has provided a detailed picture of how this material is strained to large values in loading conditions typical of deformation processing, and the accommodation of these strains by internal structure changes.

The deformation observed in various loading tests, and the direct estimates of strain in formed products, have shown that the areca sheath has high formability akin to that of ductile metals. Strains as large as 0.35 in uniaxial tension, 1.2 in uniaxial compression, 1.6 to 2 in rolling and 0.5 to 0.7 in biaxial tension have been demonstrated (**Table 4.1**), providing a measure of formability in different orientations. With the exception of the uniaxial tension, these strain values are not quite

the forming limits for the various loading cases since they do not always represent the strain at failure. Importantly, the role of hydration, which greatly increases the failure strain in tension, has only been partially explored (**Table 4.1**). The observed two- to four-fold increase in ductility/formability in tension due to hydration is much greater than, for example, that documented in bamboo (~ 67%, from 0.04 to 0.067), or Sisal fiber (from 0.02 to 0.04) used in rope and twine [55]. We expect to see similar increases in failure strain and formability due to hydration in the other loading configurations. While prolonged hydration (12 h) reduces the strength significantly, a short (2 h) duration hydration treatment is just as effective as the long duration one in increasing the formability (**Fig. 4.2**).

The areca sheath is quite deformable at the local (surface) scale too, for example, withstanding strains as large as 1.6 at the striation level, as seen in the rolling experiments. This local deformation characteristic has implications vis-a´-vis modifying the die-sheath contact condition and product quality. By tailoring the die surface topography and/or enhancing die contact pressure, it may be feasible to reduce the striation heights and therefore, the surface roughness. Also, the striations could act as natural grooves for holding lubricant, which can reduce friction at the die-leaf interface in lubricated forming; this will be beneficial for imposing larger shape changes and improving surface quality (e.g., finish, minimizing defects). Lubrication is not used in current areca leaf forming processes.

Examination of changes in structure with increasing deformation in uniaxial compression have shown that the imposed large strains are initially accommodated by pore-size reductions (dilatation strain), followed by deformation of non-porous areas as well as pore closure, see **Fig. 4.3**. At 70% thickness reduction, nearly all the pores in the matrix and fibers are closed, followed by failure soon thereafter. More generally, this condition of complete pore closure, followed by failure in the matrix, or fiber-matrix interface, may well represent the strain limit for any type of compressive deformation process with the palm . In conjunction with direct observations (e.g., SEM, μCT), the changes in structure could also be tracked by analysis of the load-deformation response in the test, though the results are not presented here. Like other plant materials, the deformation response of areca sheath showed significant anisotropy [33,36], consistent with its fibrous, hierarchical structure – the strength and Young's modulus in the LD orientation (also, fiber length) are as much as 1.5 orders of magnitude larger than in the TD orientation. The effect of hydration on these properties

is also influenced by the loading direction, with a larger hydration influence observed for the TD than the LD orientation.

The structure-deformation correlations observed with the areca palm leaf-sheath suggest certain attributes that favor high formability in plant materials, critical for product manufacturing by single-step deformation processing. These include sufficient porosity in the material structure to accommodate dilatational strains; hydration to increase failure strain (in tension); relative orientation of the plant material relative to loading direction, e.g., as with fibers lying in the plane of the sheet (sheath) being stretched; suitable heat application to minimize material spring back after the forming-load release; and sufficient material wall thickness and strength to ensure product integrity.

4.6 Conclusion

In summary, a study has been made of the deformation response of a model plant material system - areca palm leaf-sheath – with the goal of developing new single-step deformation processing routes for plant-based materials. The areca sheath is shown to have remarkable forming withstanding strains of 0.5 to 2 in loading configurations such as stretching, compression and rolling, typical of forming processes. This large strain accommodation is observed both at the bulk and surface length scales. It has been possible to reconstruct a conceptual picture of how the large forming strains are accommodated, e.g., dilatation in compression, thus providing a basis for the high formability of areca sheath and of its deformation anisotropy. The forming limits can be significantly enhanced by hydrating the sheath prior to the deformation. With further development of a detailed forming limit diagram for in-plane stretching (see next chapter), and utilizing the interactive effects of hydration, temperature and material anisotropy on deformation, it will be feasible to manufacture a wider range of sustainable foodware from the palm leaf materials, including high-aspect ratio product shapes. Furthermore, the results can potentially be used to improve and optimize the current heuristically-devised manufacturing process.

5. A STUDY OF FORMABILITY USING LIMITING DOME HEIGHT (LDH) TESTING

5.1 Abstract

Deformation response of *areca catechu* palm leaf-sheath under biaxial stretching is evaluated using Limiting Dome Height (LDH) testing. It is shown that the leaf material has high formability, with biaxial limit strains of ~ 0.4 at failure, comparable to that of ductile sheet metals. Hydration of the leaf-sheath prior to the forming increases the limit strains by as much as 500% and lowers deformation forces by up to 85%. The results also demonstrate the potential of the LDH test, originally developed for understanding formability of sheet metals, for characterizing the stretch-forming response of plant materials. Using the deformation force data, we estimate the embodied energy of areca sheath foodware and show it is 4 to 5 orders of magnitude smaller than for equivalent plastic or paper products.

5.2 Introduction

The ability to create areca foodware by direct stretch forming of sheath points to the high formability of this sheath material. This high formability is also emphasized by manufacturers in discussions. One question frequently posed by manufacturers is what kinds of high-aspect ratio shapes can be produced from areca sheath using the stretch forming approach or other similar approaches. To answer this question scientifically, it is useful to know the forming limits of this sheath material in different types of loading configurations. Such knowledge of forming limits has been critical in advancing the use of metals in many products in everyday use, from car body panels to wire windings to packaging and storage shelves. In Chapter 4 we began exploring this formability question and showed that the leaf-sheath can undergo uniform elongation of as much as 35% in uniaxial tension, and thickness reduction of ~ 70% in compression and rolling, prior to failure, especially under suitable hydration conditions (**Chapter 4**). We build on these results in the present chapter by directly characterizing the stretch-formability limits of areca sheath using limiting dome height (LDH) testing (**Fig. 5.1**).

The Limiting Dome Height (LDH) is a classical test that is widely used in the sheet metal forming sector to assess formability under conditions of plane-stress loading [47–51,54]. It also closely mimics

the punch stretch-forming process used to manufacture areca foodware such as plates and bowls, compare **Fig. 5.1** and **Fig. 2.1**. In this chapter, we present the forming limits for sheath obtained from the LDH testing. Parameter effects on formability such as arising from hydration of the sheath, step-wise loading, and NaOH treatment of the sheath are also studied. The NaOH treatment as a parameter effect is based on observations that show NaOH to be a good wood softener**,** and reported increases in bending-formability of wood due to the NaOH [56–58]. The results, besides providing basic limits on formability of the sheath for stretch-forming, should also be of value for improved systematic design of product shapes that can be manufactured from the leaf materials, and forming process optimization to maximize shape changes and produce high-aspect ratio foodware products.

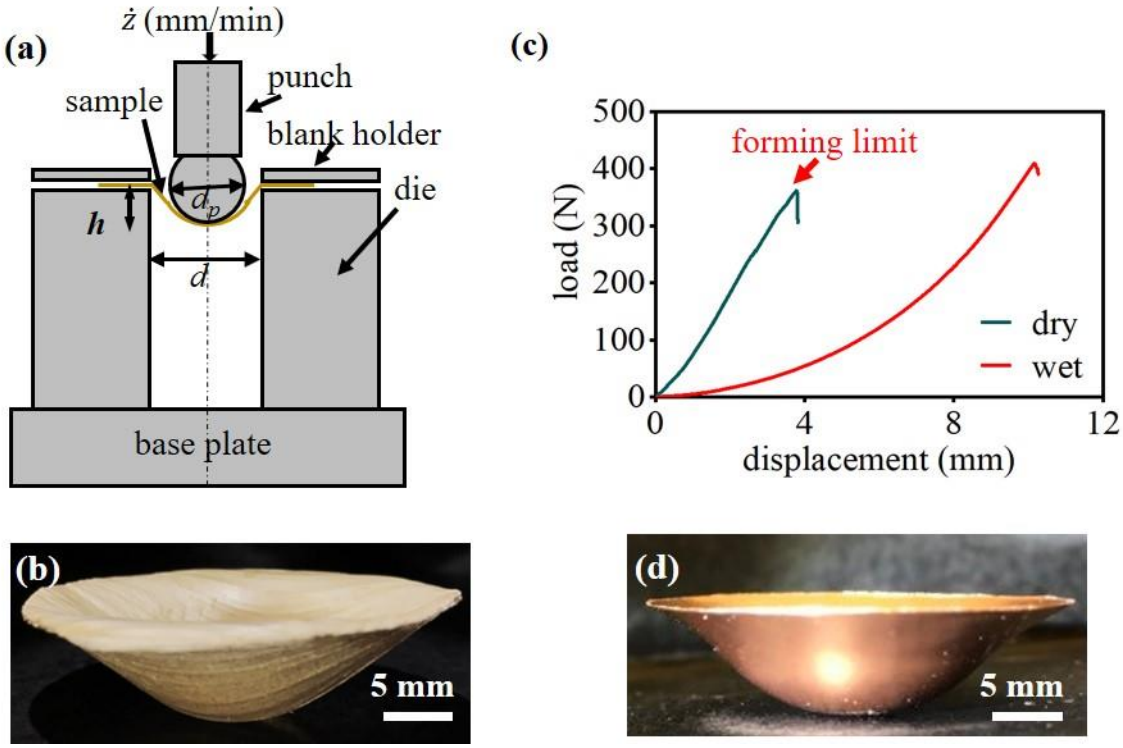

Figure 5.1 Limiting Dome Height **(**LDH) testing (a) Schematic of experimental setup with spherical punch used in the LDH test for biaxial stretching. (b) Cup of depth 9 mm formed by stretch-forming of areca sheath. (c) Load vs displacement curves for dry and hydrated (wet) sheath. Punch velocity $(\dot{z})$ is 5 mm/min. (d) Copper sheet (thickness ~ 30 micrometers) formed into cup of depth 9 mm in LDH.

5.3 Method

The formability of the sheath was characterized by measuring forming limit, i.e., punch penetration to failure, in a Limiting Dome Height (LDH) test, see **Fig. 5.1a**. The LDH test samples were of size 40 mm × 40 mm × 3 mm (thickness) that were cut out of the sheaths just prior to the experiments

5.3.1 Limiting Dome Height (LDH) test

The Limiting Dome Height (LDH) test is one of the most widely used methods for characterizing formability of sheet metals [47–51]. In this test, a thin sheet of material, the test sample, is clamped along its periphery and then axi-symetrically stretched (expanded) into a cup/bowl form, see **Figs. 5.1a and b**. The stretching is accomplished by application of a hemispherical punch that is pressed onto the unclamped central (disk-shaped) region of the sample; this loading is commonly described as one of biaxial stretching. The LDH test configuration of **Fig. 5.1a** closely resembles the actual sheath forming process **(Chapter 2)** that is used to make foodware such as cups, plates and bowls, except that there is no bottom die in the LDH in contrast to the actual forming process.

An MTS tensile tester (maximum load – 2 kN) was adapted to carry out the LDH test. The hemispherical punch of diameter, $d_p = 25$ mm, was held in the movable upper jaw of the tensile test machine, while the lower jaw was replaced with the LDH die with hole diameter (d) of 30 mm. The sheath test sample was clamped along a circular peripheral region using a blank holder and formed into a cup by the punch-loading applied in displacement control mode (**Figs. 5.1a and b**). The diameter of the unclamped sample central region of the sheath was equal to the diameter of the hole in the die but slightly larger than the punch diameter, as is typical of LDH testing. The sheath that forms the inner side of the cup is thus in contact with the punch, while the other side is free. A thin Teflon film (solid lubricant) was placed between the sheath and punch surface to reduce the interfacial friction.

In a typical test, the punch was moved downward at a velocity of $\dot{z}$ mm/minute until the sample failed (**Fig. 5.1c**). The load was observed to increase with displacement over much of the test duration up and until onset of sample failure at a maximum penetration depth (h). At this point, a sharp load decrease was usually noted (**Fig. 5.1c**). In contrast to the areca forming process, which uses heated dies to prevent sample spring-back and lock in the sample shape [15], the punch in the

LDH test was kept at room temperature. Spring-back of the sample was prevented by flowing hot air at 120^0C for 3 minutes, at the maximum load/displacement, before releasing the load.

The formability is reported and assessed in terms of the maximum (limit) strain developed at the sample pole (bottom-most point of cup), at failure. Based on assumptions of zero friction at the interface between the punch and sheath, and isotropic material response, the maximum in-plane strain (ϵ) at the pole is obtained using a solution for this loading case provided by Hill [47,54], as $\varepsilon = \ln(1 + (2h/d)^2)$. Here, h is the maximum punch penetration depth, and d is the diameter of the bowl corresponding to its periphery at this limiting depth. The solution is applicable for bulging of a diaphragm wherein the ratio of the diaphragm thickness to the sample diameter (d) is very small, that bending and shear stresses can be neglected (For our LDH testing case, this ratio is ~ 10). Both d and h were measured under load in the LDH tests for each sample. It is this pole strain from Hill's solution that is reported as the forming limit strain in the ensuing.

5.3.2 Parametric effects

Several parameters, of potential relevance to areca leaf formability, were studied in a series of LDH tests. These parameters and associated test conditions are listed and described below. Unless otherwise noted, the LDH tests were done with a punch velocity ($\dot{z}$) of 5 mm/min, monotonic continuous loading, and with hydrated (wet) sheath samples. The hydration treatment was a 2-hr immersion of the sheath test sample in water just prior to the test.

- Forming of areca foodware is typically carried out by applying the punch-load to the adaxial surface. Hence, the adaxial side becomes the inner surface of the formed product, i.e., the surface in contact with the food. Since the adaxial and abaxial surfaces have different structural and physical attributes [26,59]**,** the LDH tests were conducted with both adaxial and abaxial sides loaded by the punch to determine differences, if any, in the formability.
- The effect of hydration was evaluated by testing dry sheath samples, i.e., without hydration, and comparing the measured forming limits against those of hydrated samples.
- The effect of loading (deformation) rate was studied using punch velocity $\dot{z}$ of 1, 5, 10 and 20 mm/min.

- The effect of stepwise loading was studied in a set of experiments wherein the punch was loaded in incremental displacement steps of 3 mm up to the sample failure. Furthermore, at the end of each 3-mm step, the displacement was held fixed for durations of 15 sec, 30 sec and 60 sec.

5.4 Results

5.4.1 Forming strain in LDH

Figure 5.1b shows a cup, with aspect ratio h/d of 0.33, produced by the biaxial stretching in LDH test. No failure was seen on the surfaces of the cup. For reference, a cup produced by stretching of ductile copper (30 micrometers thick) in the LDH test is shown in **Fig.5.1d**. The areca cup from the LDH test shown in **Fig. 5.1b** is analogous to a bowl produced by a commercial (small-scale) areca sheath forming process. But its aspect ratio is higher than that of commercial bowl products $(h/d < 0.2)$. Interestingly, dimension/shape measurements showed the cup in **Fig. 5.1b** to closely resemble a hemispherical cap, except in the very vicinity of the clamped sample periphery, even though a lower die was not used to confine the deformation and constrain the shape change as in the commercial forming process.

Typical load-displacement curves to failure obtained for the hydrated and dry samples in the LDH test are shown in **Fig. 5.1c**. The failure in both cases always occurred at the pole of the cup. The penetration depths at failure (h) in the dry and hydrated conditions are seen to be 3.8 mm ($h/d = 0.13$) and 10.1 mm ($h/d = 0.34$), respectively, corresponding to maximum (pole) strains of 0.06 and 0.38 in the corresponding sheath samples. For reference, the maximum strain in a commercial bowl product is ~ 0.15. It is clear from the load-penetration curves and the strain values that the hydration treatment produces a significant increase in the formability and forming limit – an approximately 500% in the pole strain at failure. Similar large increases in the strain at failure with hydrated samples have also been observed in uniaxial tensile testing of this sheath material [34]. **Figure 1c** also shows that the force required to produce a given shape change or punch-penetration is significantly lowered by the hydration. For example, the maximum load, occurring almost at the failure limit, with the dry sample is ~ 350 N; whereas the corresponding load at the same penetration depth of 3.8 mm with the hydrated sample is < 50N, an ~ 85% load decrease. Thus,

both from a shape change standpoint and force/energy considerations, the hydration treatment has a remarkably beneficial effect on formability.

Figure 5.2 summarizes the key formability results from the parametric studies involving loading rate and stepwise loading. The top row in **Fig. 5.2** shows the load-displacement curve and strain data for the various loading rates. The pole strain at failure is seen to decrease with an increase in the loading rate, from ~ 0.38, at the smaller loading rates of 1 and 5 mm/min, to ~ 0.25, at the highest loading rate of 20 mm/min. This represents a decrease of ~ 30% in formability. Concomitantly, there is a small increase in the punch (deformation) force. These results are somewhat analogous to the effects of strain rate on ductility and (yield) strength of metals. Note also that at the two smaller deformation rates, the load-displacement curves in **Fig. 5.2** (top left) essentially overlap one another.

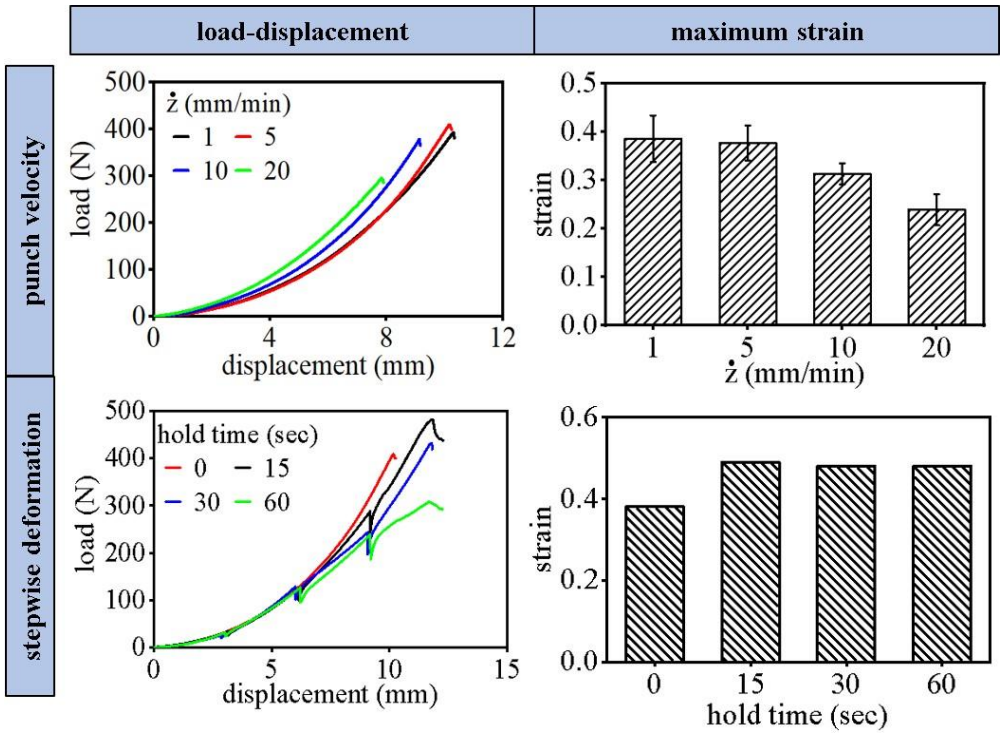

Figure 5.2 LDH Load-displacement curves and forming limit strains. (top row) Effect of punch velocity $(\dot{z})$. (bottom row) Effect of imposing stepwise deformation.

The effects of stepwise loading on the load-displacement curve and forming limit strain are depicted in the bottom row of **Fig. 5.2**. There is an ~ 30% increase in the limit strain when the loading is imposed under stepwise displacement control compared to the monotonic continuous

loading case (hold time = 0 sec., **Fig. 5.2** bottom left). This increase in failure strain is seen to be independent of the hold-time duration. The effect of stepwise loading on the deformation force is negligibly small in the initial stages of loading, up and until 6 mm of punch penetration. Beyond this point, and until sample failure, the deformation force is seen to be smaller for the larger hold times.

Figure 5.3 encapsulates the formability results for punch-load application to the adaxial and abaxial surfaces. The former corresponds to the loading configuration used in the commercial areca-forming process. The load-displacement curves (**Fig. 5.3a**) show that the penetration depth at failure is somewhat larger when the load is applied to the abaxial surface ($h = 11.8$ mm) than the adaxial surface ($h = 10.1$ mm). This is reflected in the higher strain at failure in the abaxially-loaded sample ($\varepsilon \sim 0.48$) compared to the adaxially-loaded case ($\varepsilon \sim 0.38$). The larger strain at failure in the abaxially loaded sample is likely due to the outer cup surface, the adaxial surface, being more ductile, due to its structural characteristics, as noted earlier.

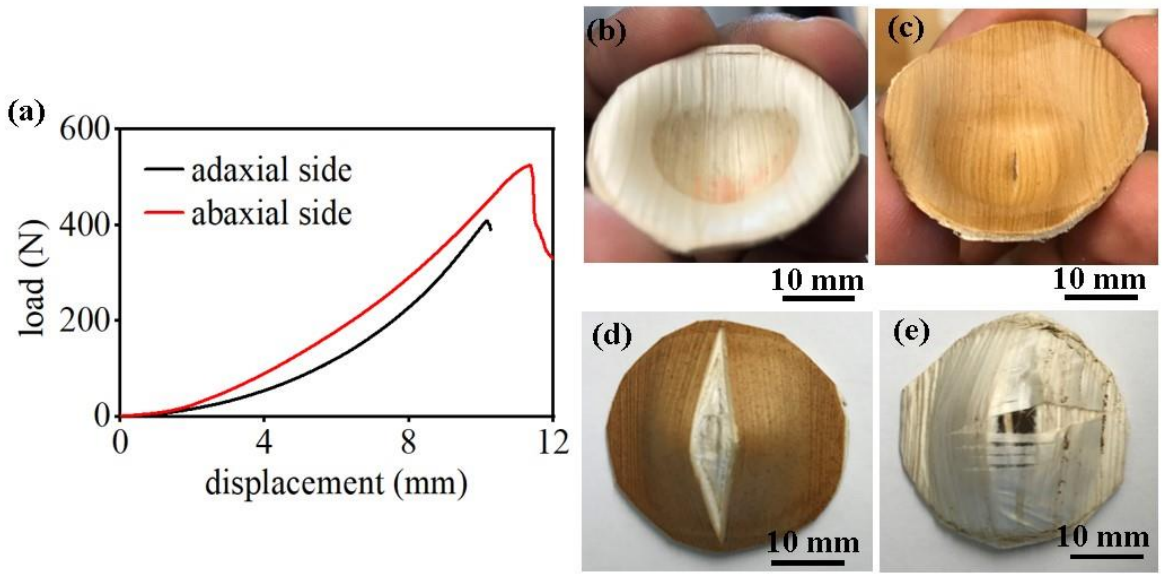

Figure 5.3 Deformation response of sheath in LDH for adaxial and abaxial surface loading. (a) Load-displacement curves. (b) and (c) Inner surface of the bowl when load is applied to (b) adaxial and (c) abaxial surface. (d) and (e) Corresponding failure regions on the bowl outer (d) abaxial surface and (e) adaxial surface. Failure in both loading cases occurs at the pole. Note, however, the difference in failure morphology.

Fig. 5.3b-e show macrographs of the formed products and the failure regions for the two loading cases. The inner surfaces of the formed products are shown in **Fig. 5.3b** (adaxial loading) and **Fig. 5.34c** (abaxial loading). The surfaces are smooth in both cases, but with pronounced differences in the surface texture and shading. The latter characteristics reflect the inherent differences in the physical attributes of the sheath adaxial and abaxial surfaces. The region of punch load application, that is the contact region between the punch and the sheath surface, is also well-demarcated in the figures as a contrast between the central region of the cup and the peripheral region. Besides the formability change, the other striking difference is in the failure mode, see **Fig. 5.3d and e**. In both the loading cases, the failure is seen to occur on the outer surface of the cup and at the pole. For the adaxial loading, the failure occurs by "splitting" of the outer abaxial surface; this splitting involves displacement of material in a direction perpendicular to the fiber length orientation (**Fig. 5.3d**). In the abaxial loading case, the failure on the outer adaxial surface involves tearing of the epidermis skin layer (**Fig. 5.3e**). These types of outer-surface failures were observed consistently across multiple specimens.

5.4.2 NaOH treatment

We studied the possibility of increasing the formability of areca sheath via a treatment with an aqueous solution of NaOH, prior to the deformation, analogous to the hydration treatment. NaOH treatment is commonly used for softening wood and for increasing its bending [57]. Furthermore, specific NaOH solution treatments, in combination with compression loading of the wood after the treatment, have also been used for enhancing the structural properties of bulk natural wood, especially strength [58]. This is because the NaOH treatment enables the wood to be compressed easily, with significant densification resulting. Since the action of the NaOH solution in all of these cases weakens the bonding between cellulose by partially removing cellulose and lignin from natural wood, we hypothesized that there could be an increase in formability due to this treatment [57,60,61].

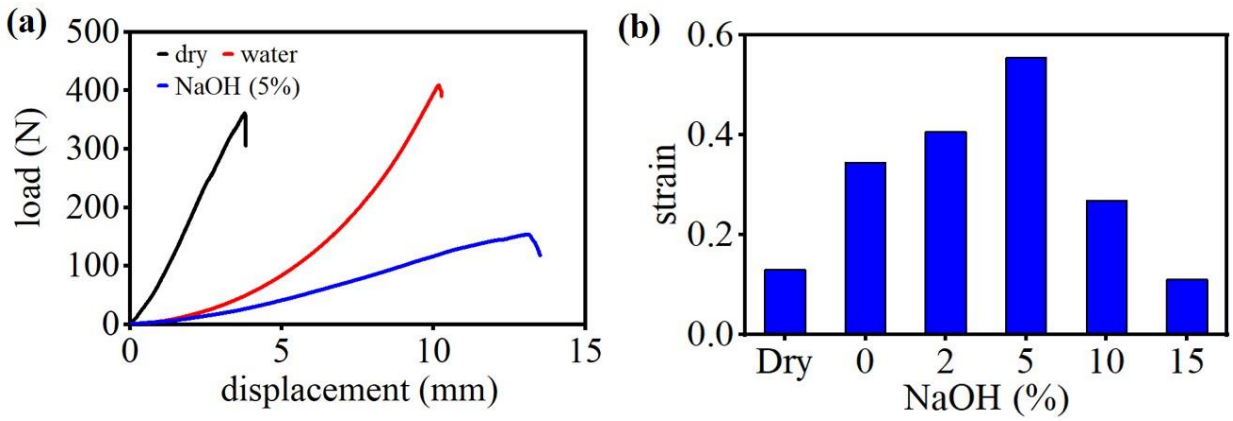

Figure 5.4 LDH data for dry sheath, sheath hydrated with water, and sheath treated with 5% NaOH aqueous solution for 2 hr. Punch velocity $(\dot{z})$ is 5 mm/min. a) Load vs displacement curves (b) Effect of NaOH concentration on forming strain. Left bar in figure (b) correspond to the strain in dry sheath.

To explore the hypothesis, we added 2%, 5%, 10%, and 15% by weight of NaOH to the water during the hydration process and treated the sheath in this aqueous NaOH solution for 2 hours. **Figure 5.4a** shows the load-displacement curves obtained in LDH testing of the sheath for the dry, hydration (water) and 5% NaOH solution cases. Based on this data, the forming limit strains were obtained as before using the Hill solution. **Figure 5.4b** summarizes the LDH forming limit strains for the various NaOH concentrations. The 0% NaOH limit strain in this figure corresponds to the pure water (hydration) treatment.

It is clear from **Fig. 5.4b** that when the sheath is treated with the NaOH solution, the limit strain increases, relative to the pure water case, up to a concentration of 5% NaOH. In fact, the maximum forming limit strain of ~ 0.55 occurs at this concentration. Concurrently, the forming force needed to produce a given shape change decreases significantly, see **Fig. 5.4a** for the 5% NaOH case. Both of these effects – limit strain increase and force decrease - are quite significant (up to 5% NaOH), representing a substantial improvement in sheath formability over the pure hydration treatment case. Beyond 5% concentration, however, the NaOH treatment has an adverse effect on the limit strain. For example, with 15% NaOH solution treatment, the limit strain is < 0.1, almost approaching the dry sheath limit.

SEM analysis of the sheath samples was performed to investigate changes in the microstructure of the sheath due to the 5% and 15% NaOH concentrations, that may have influenced the forming

strain. **Figure 5.5a** shows SEM images of the original sheath, and sheaths treated with the 5% and 15% NaOH solutions for 2 hours. There is no discernible change in the sheath microstructure between the dry and 5% NaOH solution treated sheath. However, in the sheath treated with the 15% NaOH solution, the cell walls appear to have disintegrated and dissolved, with significant structural damage to the material.

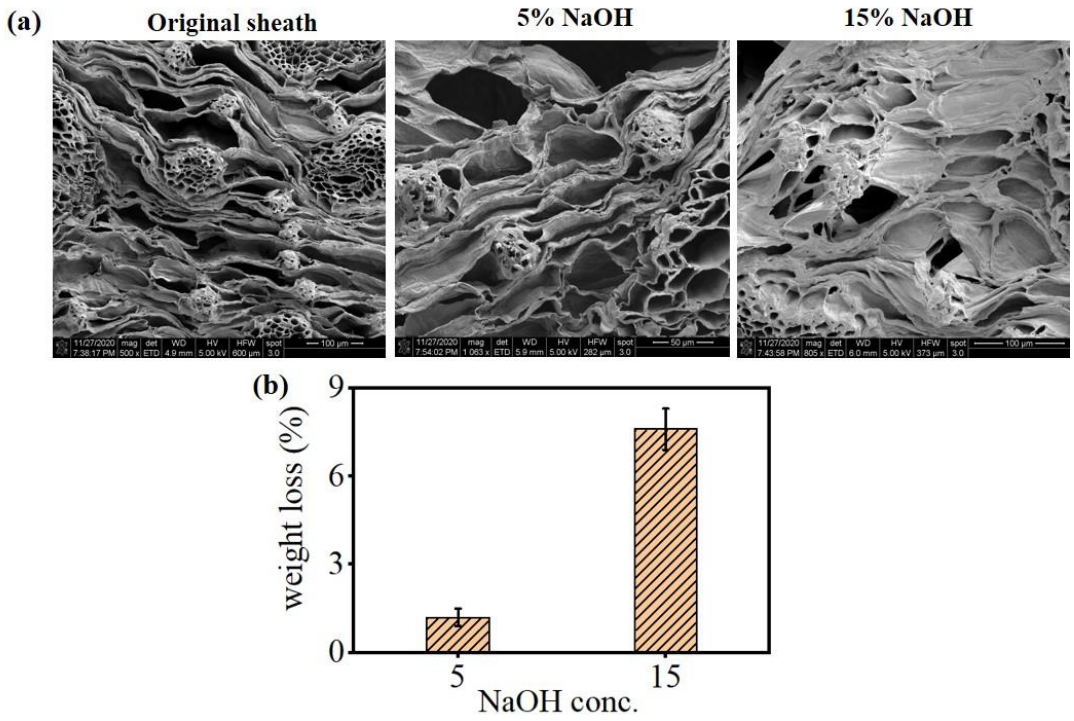

Figure 5.5 Effect of NaOH concentration on sheath structural characteristics (a) SEM images showing microstructure of original sheath, and sheath treated with 5% and 15% NaOH solution for 2 hours. (b) Weight loss of the sheath due to the 5% and 15% NaOH solution treatments.

We also measured the mass of the sheath after the NaOH solution treatments. This was done as follows. In each experiment, we measured the mass of the dry sheath initially. Each sheath sample was then immersed in the 5% and 15% NaOH solutions. After 2 hours of immersion, the samples were removed from the NaOH solution and washed several times with distilled water to remove all traces of the NaOH. The sheath samples were then dried in lab ambient environment for 48 hours before being weighed. A loss of weight was seen in the samples after the NaOH treatments. **Figure 5.5b** shows the weight loss (percent loss); this loss is ~1% with the 5% NaOH solution and ~8% with the 15% NaOH solution treatment. The results indicate that more mass in the form of hemicellulose and lignin is removed when the sheath is treated with the 15% NaOH solution. This

larger scale removal of hemicellulose and lignin with the 15% solution damages the material structurally, in addition to weakening the bonds between cellulose. Whereas the 5% NaOH solution treatment only weakens the bond between cellulose, while removing only negligible amounts of hemicellulose and lignin [56,57,60,62–64]. This explains why the forming limit strain increases with %NaOH for the lower concentrations (5% and below) and decreases rapidly beyond the 5% threshold concentration. The optimum treatment is one that just results in a weakening of the between cellulose but without causing large-scale structural damage to the material (as seen with the SEM image corresponding to the 15% NaOH case in **Fig. 5.5a**.

5.4.3 Modified LDH testing: Forming limit with cylindrical indenter loading

We carried out another type of "modified LDH" experiment wherein the load was applied by a cylindrical of diameter 20 mm, see **Fig. 5.6**, rather than a spherical punch. In this test, an ~ 3mm thick, rectangular hydrated areca sheath, the test sample, was clamped at the extremities along the length, and then indented (stretched) with the cylindrical indenter. Since the loading is now not axially symmetric, but more closely resembles uniaxial bending/stretching, the experiment could be used to examine anisotropy in the forming limit strain, and failure mode, by using two different (specimen) orientations of the striations (grooves) with respect to the load axis as shown in the figure.

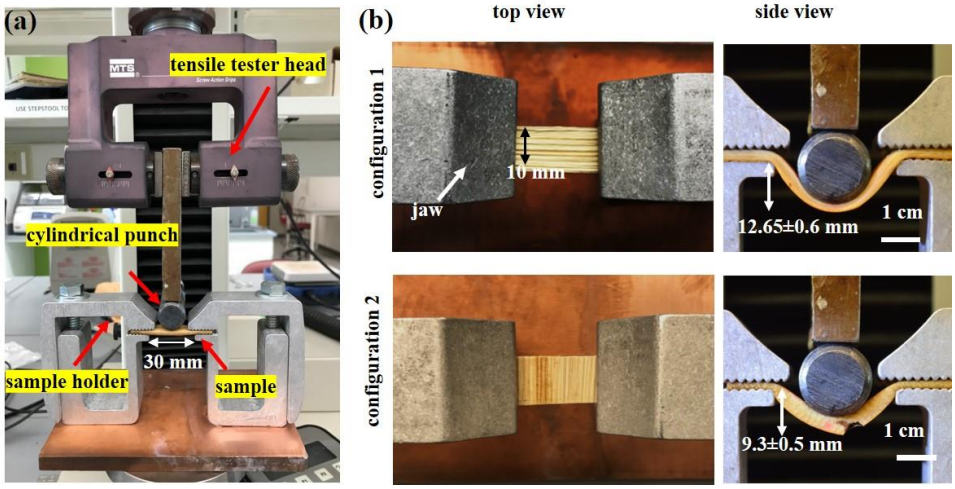

Figure 5.6 Modified LDH test (uniaxial stretching) with cylindrical indenter (a) experimental setup (b) Top view (before deformation) and side view (after deformation) of sheath in two configurations: length of sample (30 mm dimension) is along the direction of the striations (configuration 1) and sample length perpendicular to the direction of striations (configuration 2).

The cylindrical indenter of diameter, 20 mm was held in the movable upper jaw of the MTS tensile test machine. The loading was applied to the sheath adaxial surface in the unclamped central region of the sample as shown in Fig. 5.6b. The unclamped (forming) region of the samples was 30 mm × 10 mm × 3 mm (thickness), where the 30 mm is the dimension along the length direction (**Fig 5.6a**). The 10 mm dimension is along the width direction (**Fig 5.6b**). The length of the unclamped region (30 mm) was slightly larger than the diameter of the cylindrical indenter. A thin Teflon film (solid lubricant) was placed between the sheath adaxial surface and the indenter surface to reduce interfacial friction. The modified LDH experiment was performed with two different sample configurations: Configuration 1 – the length direction of the sample is along the direction of striations (LD of sheath); and configuration 2- the length direction of the sample is perpendicular the direction of striations (TD of sheath). Both of these configurations are shown in Fig. 5.6b. The loading was applied by moving the indenter downward with speed of $\dot{z} = 5$ mm/minute until the sample failed.

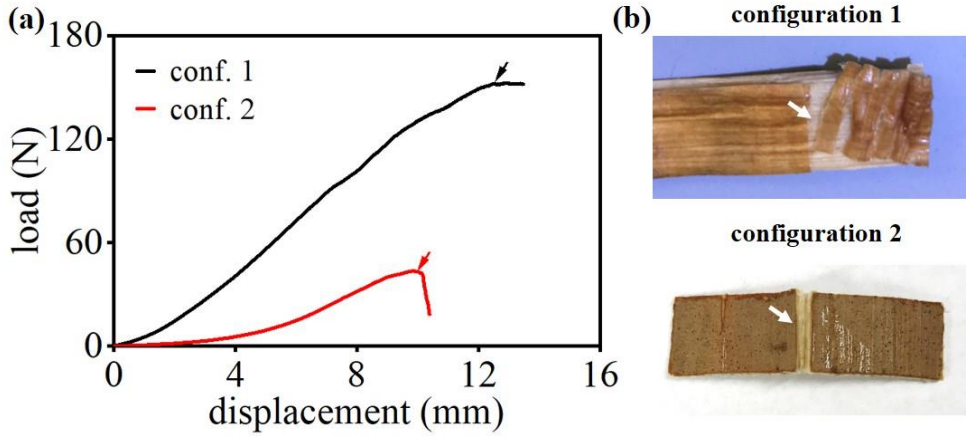

Figure 5.7 Modified LDH test results **a)** Load - displacement curve for the two configurations, sample size 30 mm × 10 mm × 3 mm (thickness). b) Failure modes (see white arrow): configuration 1- failure by tearing on the adaxial surface in between the clamped sample ends; configuration 2- splitting of the fiber on the abaxial surface.

Figure 5.7a show the load-displacement curves to failure for the two sample configurations 1 and 2. The load increases with displacement until the onset of sample failure, see at arrow in **Fig. 5.7a**. Both the load and failure depth are much higher for configuration 1 than configuration 2. **Figure 5.6b** shows side views of the deformed sheath samples at the maximum (failure) depth. The maximum depth (h) at failure in configuration 1 and configuration 2 are 12.65±0.6 mm ($h/l =$

0.42) and 9.3±0.5 ($h/l = 0.31$) mm, respectively (**Fig 5.6b**). Note that the sample length (l) is 30 mm. Using Hill's equation (see earlier LDH discussion) for the zero interfacial friction case, the maximum in-plane strain (ε) at the pole is approximately obtained as $\varepsilon = \ln(1 + (2h/l)^2)$. This gives the forming limit strain (at pole) values as ~ 0.54 and 0.35, respectively, for configuration 1 and configuration 2.

Figure 5.7b shows the failure mode for the two sample/loading configurations. In configuration 1, the failure is seen to occur on the adaxial surface by tearing. While in configuration 2 the failure occurs by "splitting" at the outer abaxial surface; the splitting occurs at the pole, with displacement of material in a direction perpendicular to the fiber orientation (along TD). The splitting mode of failure on the outer abaxial side (with configuration 2) is also evident in the sample side view shown in **Fig. 5.6b**.

It is important to note here that the failure strain and mode of failure (splitting of fiber along TD) in configuration 2 of the modified LDH test (cylindrical indentation) are the same as that observed in the LDH test with the hemispherical punch (**Fig. 5.3d**). This indicates that the formability of the sheath is determined by the failure strain along TD.

5.4.4 Embodied energy

It is useful to estimate the embodied energy for foodware produced from the palm sheath and compare it with that of equivalent plastic and paper products. The forming LDH data enables us to do this for the palm sheath products. The embodied energy of a product includes the energy of primary material production and the processing (shaping) energy.

Comparative first-order estimates of the embodied energy for foodware produced from various materials are shown in **Fig. 5.8** [59]. With plastics, for example, the primary material production contribution includes energy consumed in extracting the raw mineral (natural gas), producing monomer feedstock, and synthesizing polymer resin. The processing/shaping contribution represents the energy needed to convert the polymer resin pellets into a useful shape (e.g., plate) by melting and injection molding. For most materials, the primary production dominates the embodied energy; with molded polystyrene, for example, it represents over 85% of the total. With paper products, often seen as the classic sustainable substitute for plastic foodware, although the

processing energy is small, the embodied energy is still about half that of plastics (**Fig. 5.8**) because intermediate processes such as pulping are quite energy (and water) intensive.

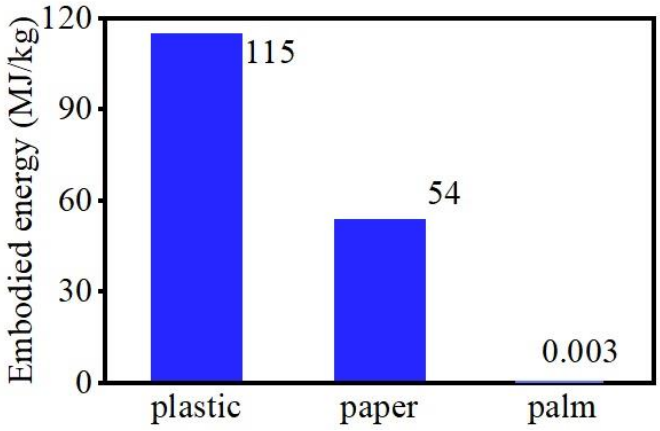

Figure 5.8 Comparison of embodied energy of areca palm sheath foodware with that of plastic and paper products [16].

Coming to the case of the palm-leaf products, as the areca palm tree is grown primarily for its nuts and sheds sheath (waste) naturally in seasonal growth cycles, the energy associated with material extraction, that is, primary material production energy, is essentially zero. Therefore, the embodied energy is just the specific energy (deformation work/mass) expended in the forming process. The load–displacement data (in wet condition) of **Fig. 5.1c** from the LDH test can be used to estimate the (forming) process specific energy, since this process is also representative of the foodware forming process (**see Figure 2.1, Section 2**). The deformation work per unit mass can be estimated as the area under the load–displacement curve in **Fig. 5.1c (**hydrated condition) divided by the mass of the dry cup (0.7 g). This calculation gives the process specific energy as ≈0.003 MJ kg^{-1}, which can be taken as the embodied energy for the palm leaf products (**Fig. 5.8**). The embodied energy for the plant leaf products is seen to be four to five orders of magnitude smaller than that of equivalent plastic or paper products.

5.4.5 Summary of deformation data and forming limit

We can now update Table 4.1 from the previous chapter with the LDH test data and forming limit strains measured for this biaxial stretching. Table 5.1 is the updated table.

Table 5.1 Formability summary: limit strains in different loading conditions (Loading usually on adaxial surface unless otherwise noted).

Test	Loading	Dry	Wet
Tensile	uniaxial	0.04 (LD) 0.07 (TD)	0.08 (LD) 0.35 (TD)
Compression	uniaxial	1.2 (DD)	1.2 (DD)
Rolling	plane-strain compression	bulk strain (from thickness) 1.9 (LD) 1.2 (TD)	
		local strain (surface profile) 1.6 (LD) 1.6 (TD)	
Foodware	biaxial stretching no slip		plate: 0.70
			bowl: 0.50
	biaxial stretching zero-friction		plate: 0.15
			bowl: 0.16
LDH (spherical punch)	biaxial stretching (zero-friction)	0.06	loading adaxial: 0.38
			loading abaxial: 0.48
			5% NaOH solution: 0.55
LDH (cylindrical indenter)	uniaxial bending/stretching (zero-friction)		length along LD: 0.54
			length along TD: 0.35

5.5 Discussion

The LDH tests have provided a first-of-a-kind, quantitative characterization of formability for areca palm sheath under stretching conditions that mimic the commercial sheath-forming process. The results have shown that the sheath material is quite formable under this type of loading, with forming limit strains as high as ~ 0.4. These strain values are similar to the limit strains reported for highly ductile and formable alloys such as Al and Cu (0.2 to 0.5) [44,45]. It is also much greater than estimated strain values (0.15) in commercial sheath products such as plates and bowls, suggesting possibilities for forming high-aspect ratio products such as deep cups and tumblers.

Hydration treatment of the sheath prior to the LDH loading has been shown to have a strong and beneficial effect on the formability, with the hydrated-sheath limit-strain being ~ 6X that of dry (non-hydrated) samples. Concomitantly, the deformation force to realize a given shape change is also lowered, by as much as 85%. Both of these beneficial effects of hydration, also observed in

uniaxial tension/compression and rolling, can be of value for expanding the scope of areca leaf products. Further increases in formability can be achieved by an aqueous NaOH treatment similar to the hydration treatment. The use of small NaOH additions to the water, e.g., 5% NaOH aqueous solution treatment, is shown to produce an ~ 50% increase in the LDH limit strain compared to the hydration case, without altering the sheath microstructure. Other parameters that increase the forming limit strain, but to a smaller degree than hydration and the NaOH treatments, are stepwise deformation and small loading-rates.

The experiments have also shown that when the punch-loading is applied to the abaxial surface, a greater forming limit strain can be achieved compared to adaxial-surface loading. The latter corresponds, however, to the loading configuration used in the commercial sheath-forming process. By turning the material inside out for forming, so to say, relative to the commercial process, the limit strain can be increased by ~ 25%, representing a significant improvement in formability. While there are factors likely related to diffusion, aesthetic features, and structural integrity, that make areca foodware manufacturers settle for the less formable adaxial loading configuration in practice, the results suggest that there are opportunities also for forming using the abaxial-surface loading for special product cases.

Modified LDH experiments (akin to uniaxial bending/stretching) using cylindrical indenter loading have shown that the failure strain is higher when length of the sample is along LD of sheath. The experiments also suggest that splitting of fibers on the abaxial surface, with material displacement along TD, likely controls the forming limit (sheath failure) in stretch forming of the sheath.

The forming limit strains for various loading conditions are summarized in **Table 5.1**. They can be used to construct a first-order forming limit diagram (FLD). This Table can be used as a design aid for determining what high-aspect ratio structures (e.g., tumblers, coffee cups) and shapes can be formed out of the sheath, and potential limits to commercial products from sheath material. Grid-deformation LDH experiments planned for the near-future will enable strain mapping across the sample surface, detailed analysis of material-response anisotropy and further refinement of the strain estimates, enabling a more complete FLD.

The study has shown that classical formability tests, used to evaluate sheet-metal forming limits, can also be applied to study formability of plant leaf materials and woods in quantitative terms.

This sets the stage for understanding the structural basis of high formability in select plant material systems. The availability of FLDs for plant materials, analogous to sheet metals, can help accelerate the development of new eco-friendly and sustainable products, besides enhancing current forming processes for plant materials. We plan to explore these aspects in the near future.

The manufacture of foodware from palm leaf represents also a fundamentally different class of materials processing from the standpoint of embodied energy and various sustainability attributes. The palm tree sheds leaf-sheaths naturally in seasonal growth cycles. Not only is the plant not sacrificed in harvesting the sheaths, but the sheath is then formed directly without the energy intensive pulping process necessary for production of paper (wood or bagasse). In this regard, the primary form of the material literally "falls from the tree". The forming forces are quite small because of the relatively low strength of the sheath. Hence, the embodied energy (~ 0.003 MJ/kg) estimated from the cup-forming process (LDH test) is 4-5 orders of magnitude less than that of paper and plastic foodware (**Fig. 5.8**) [16,17]. Similarly, the direct use of plant leaf materials, without pulping, circumvents the high water use of paper production. With only a small amount of energy needed for processing to shapes, the CO_2 emissions through the entire product lifecycle is essentially that emitted in the natural decay of the disposal process (composting), a process that would occur in any event. Lastly, the sheath material bio-degrades in ~ 100 days. These sustainability attributes of the palm material could make it especially attractive for production of food packaging [44].

5.6 Conclusion

The deformation response of *areca catechu* palm sheath under biaxial stretching has been characterized using the Limiting Dome Height (LDH) test. The leaf material is found to have high formability with limit strains (~0.4) comparable to that of ductile sheet metals. A strong beneficial effect on formability is demonstrated by hydration and aqueous NaOH treatments of the sheath just prior to the deformation processing. The hydration produces as much as a 500% increase in the forming limit strain compared to that of a dry sheath, while simultaneously lowering the forming force by as much as 85%. Smaller improvements in formability are observed under stepwise loading, low deformation rates and by turning the sheath material "inside-out". The

results also show that the Limiting Dome Height test can be a valuable tool for screening the forming response of plant materials.

Besides highlighting the potential for optimizing manufacturing of palm leaf products, the results suggest wide-ranging opportunities for plant leaf materials, with near-zero embodied energy, in manufacturing of eco-friendly foodware products using direct deformation processing routes.

6. DIFFUSION IN PALM SHEATH

6.1 Abstract

Diffusion of water into plant materials is known to decrease their mechanical strength and stiffness but improve formability. Here, we characterize water diffusion through areca palm leaf-sheath - a model plant material, with hierarchical structure, used in eco-friendly foodware. The diffusion process is studied using mass gain measurements and *in situ* imaging of water transport. By treating the areca sheath as homogeneous ensemble, and incorporating effects of material swelling due to water absorption, a factor typically neglected in prior studies, the diffusion coefficient D_w for water is estimated as $(6.5 \pm 2.2) \times 10^{-4}$ mm^2/sec. It is shown that neglecting the swelling results in gross underestimation of D_w. Microstructural effects (e.g., fiber, matrix) on the diffusion are characterized using *in situ* imaging of the water transport at high resolution. The observations show that the water diffuses an order of magnitude faster in the matrix (8.63×10^{-4} mm^2/sec) than in the fibers (7.19×10^{-5} mm^2/sec). This non-uniformity is also reflected in the swelling-induced strain in the leaf, mapped by image correlation. Lastly, we vary salt concentration by controlled additions of NaCl and note a non-monotonic dependence of the diffusion on concentration. Implications of the results for improving foodware manufacturing processes and product life are discussed.

6.2 Introduction

Diffusion of liquids through plant materials is of scientific and technological interest because of the important role they play in growth of plants, drying of wood, pulping of wood chips, and various treatments of wood products to realize specific functions (e.g., fire retardation, bending) [65–67]. The penetration of liquids such as water can also have an adverse effect on mechanical properties of plant matter, especially strength and stiffness [68]. This change in mechanical properties is of concern in applications ranging from load-bearing structures, e.g., boats and construction materials [68,69], to eco-friendly plant-based foodware (e.g., plates, bowls) and packaging [59]. In the foodware applications, the product life is determined largely by the time taken for semi-solid and liquid elements (e.g., water, oils) in the food to penetrate through the walls of the foodware; and resulting deterioration in structural. However, liquid (e.g., water) treatments can also be beneficial

such as in enhancing formability of plant materials for manufacturing. This aspect is exploited in direct, single-step forming of foodware from plant leaf materials by pressing. The varied applications and nature of liquid effects point to a critical need for accurate characterization of liquid diffusion through plant materials, including measurement of diffusion coefficients. Such characterization should be valuable for elucidating mechanisms of liquid transport, understanding mechanical property changes, estimating product life as with foodware, and improving product design and manufacturing.

To date, the majority of diffusion studies with plant materials has focused on moisture (vapor) transport through woods[69–71], with only a few studies on diffusion of water that has been brought in direct contact with woods [72–74]. Using mass gain measurements, diffusion coefficients have been estimated for various woods. Given the hierarchical structure of plant materials [33,38], it is quite likely that the diffusion process is strongly influenced by the microstructural constituents such as fiber and matrix. Furthermore, while occurrence of swelling in these materials due to water exposure is well-recognized, the effect of swelling on water transport and diffusion coefficient has largely been ignored in the prior studies[70,71,75,76]. The inclusion of swelling in the diffusion characterization should greatly improve the accuracy of diffusion coefficient measurements.

In this study, we analyze diffusion/permeation of pure water through areca palm sheath. We directly address the aforementioned gaps in the diffusion characterization using this material system. The selection of this particular leaf material for the study is motivated by its hierarchical structure that is representative of the broad class of plant materials, and the use of the sheath in single-use foodware applications. Areca palm leaf-sheath (~ 3 mm thick) has emerged in recent years as a sustainable alternative to plastics, for eco-friendly foodware and packaging. Plates, bowls and cups, can be produced in a single step, directly, by forming of the leaf-sheath, analogous to stretch-forming of sheet metal**.** To accomplish the stretch-forming, the leaf material is subjected to an initial hydration treatment – water exposure for several hours - to enhance its formability. Currently, the selection of hydration parameters, e.g., duration, temperature, is largely based on empiricism and historical practice. An understanding of the mechanisms of water diffusion, including parametric effects, could enable improvements in forming process efficiency through optimization of hydration parameters. Besides its influence on formability, water diffusion into the sheath is the single most important factor governing foodware product life and applications scope.

For example, plates and bowls made of areca leaf-sheath become soggy, losing their structural integrity in about 60 minutes (life) when brought into contact with water-rich foods. Discussions with areca leaf product manufacturers suggest that if the product life can be doubled to 120-180 minutes, then the range of foodware applications for this material would be greatly enhanced. A study of water diffusion is therefore of value both for enhancing manufacturing capability (formability) and predicting/enhancing product life.

To characterize the diffusion, we use a novel *in situ* optical imaging technique, that tracks the water front as it diffuses into and around various microstructural components such as fiber and matrix, complemented by mass gain measurements. The imaging directly reveals that the water diffuses much faster through the matrix than in the fibers. The rate of water diffusion determined by the imaging is shown to be consistent with that estimated from the conventional mass gain measurements. We account for the effect of material swelling in the diffusion characterization, and show the importance of including this parameter for accurate estimation of the diffusion coefficient. By analyzing the image sequences, we also compute the deformation strain due to swelling, and find that the strain is higher in the matrix than in the fibers. Finally, we examine parametric effects associated with water temperature and salt concentration, effects relevant for foodware applications. The diffusion characterization methodology and the results obtained should be applicable to the broad class of plant materials. The results also suggest technological opportunities for advancing the use of plant materials in production of eco-friendly foodware and optimizing associated manufacturing processes.

6.3 Method

6.3.1 Characterization of diffusion process

The diffusion of pure distilled water (laboratory grade) through the sheath of thickness 3 mm was studied in two ways: 1) by estimation of diffusion coefficient from measurements of mass gain, after exposure of the sheath adaxial surface to the water for varying time durations (**Fig. 6.1a**); and 2) by direct *in situ* observations of movement of water from the adaxial surface through the sheath material, using an optical microscope; these observations were made from a side of the sample (**Fig. 6.1b)**.

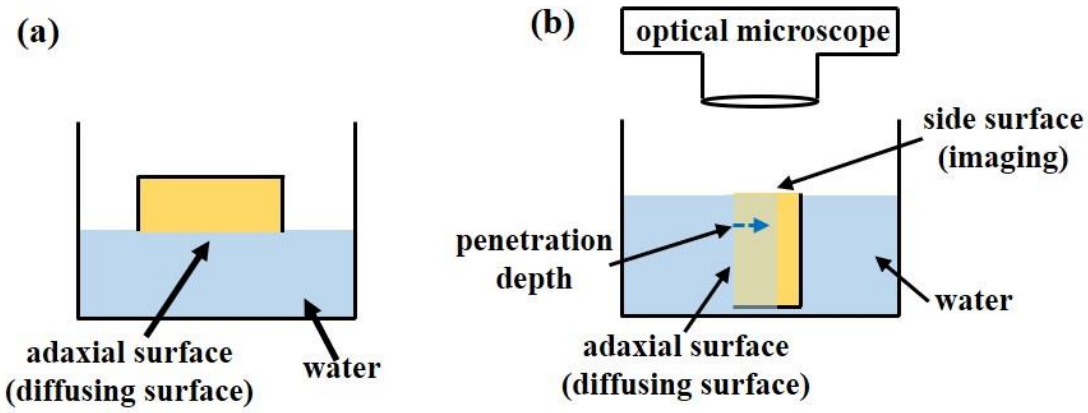

Figure 6.1 Schematic of setups for (a) mass gain measurements and (b) in-situ observations of water penetration through the sheath. The light gray region in (b) is the region penetrated by the water. The black lines on the various surfaces represent the rubber sealant coating used to prevent entry of water via these surfaces.

6.3.1.1 **Mass gain**

To characterize the diffusion using mass gain, square samples of cross-section 10×10 mm^2, and thickness ~ 3 mm, were cut out of the sheaths using a sharp scalpel. The 10 mm × 3 mm sides and the abaxial surface of each sample were coated with a white water-resistant, rubber sealant (Flex Seal), and allowed to dry for 24 hours (**Fig. 6.1**). This coating ensured that the water could enter the samples only through the adaxial surface, and diffusion was essentially 1-D through the 3-mm sheath thickness direction (DD).

The adaxial surface of each sheath sample was then exposed to pure water as shown in **Fig. 6.1a.** In this arrangement, the sample is just floated on the water surface with the adaxial surface face downwards and in uniform contact with the water (**Fig. 6.1a**). For measuring the mass gain, each sample was withdrawn from the water at regular intervals and gently wiped with a cotton swab to remove any surface water. The sample mass was then measured with a micro balance (resolution 0.001 gm). The amount of water (m_t) diffusing into the sample per unit area is then obtained as:

$$m_t = \frac{M_t - M_0}{A} \tag{6.1}$$

where M_0 is the initial mass of the sample, M_t is the mass of the sample after it has been in contact with water for time t, and A is the area of the diffusing surface (10×10 mm^2). This m_t is used to compute the diffusion coefficient (D).

In the experiments, it took approximately 5-10 seconds to bring the sample out of the water, measure the mass and replace it back onto the water surface. That these periodic interruptions had a negligible effect on the diffusion process was established by making similar mass gain measurements in samples wherein the process was not interrupted in this manner. This is due to the interruption/measurement time being small compared to the time span of the diffusion. It was also verified that gravity had no measurable influence on the mass gain.

Measurement of swelling To accurately estimate D, it is necessary to account for swelling of the sample due to the water penetration. An initial series of measurements showed that there was negligible change in sample dimension along LD or TD after the input of water by diffusion. Hence, the swelling could be characterized by thickness measurements along DD after bringing the sample adaxial surface first into contact with the water surface, as in **Fig. 6.1a**, for varying time durations. After each exposure, the sample was removed from the water and its thickness parallel to DD was determined by measuring the displacement of five reference points on the adaxial surface using a dial-indicator. The thickness change $(-z_s)$ was computed from the mean of these readings for the various exposure times**.**

The measured $-z_s$ was plotted against $\sqrt{t}$ based on the assumption of a parabolic sheath expansion due to the water absorption [77,78]. The data (see ensuing) confirmed this parabolic expansion. The $-z_s$values are used to establish the adaxial surface location during the diffusion process for estimating D.

Effect of NaCl concentration and temperature The effect of salt concentration and temperature on diffusion was studied by conducting mass-gain experiments with 0%, 2%, 5%, 8%, and 12% NaCl (gm/100 ml) aqueous solution (NaCl in water) at 25^0 C (room temperature-RT), 50^0 C and 70^0 C. For the elevated temperature experiments, the solution was heated inside a thermally insulated chamber and each diffusion experiment was started after temperature of the solution had settled at the desired value. The temperature of the solution was monitored with a digital thermometer.

6.3.1.2 **In-situ observations of water penetration**

In situ observations of water penetration through the sheath thickness from the adaxial surface provided a direct means for monitoring the diffusion. These observations were carried out using the sample configuration shown in **Fig. 6.1b,** with square cross-section (3 mm × 3 mm) samples of thickness ~ 3 mm. For these experiments, only four of the six surfaces of each sample were coated with the water-resistant sealant. The two surfaces left uncoated were the adaxial surface, to allow for water entry; and one of the side-surfaces (imaging surface), through which the diffusion of water was observed using an optical microscope coupled to a CMOS high-speed camera, at spatial resolution of ~ 2.5 μm. The sheath was placed on the water surface as shown in **Fig. 6.1b**, with the imaging surface oriented upwards and slightly above the water surface. Images were recorded at 30 frames per minute, using the microscope-camera assembly, thus obtaining a complete record of the water penetration. As the water entered the sheath, there was a distinct change in the brightness over a segment of the exposed surface due to the penetration. By suitable image processing with ImageJ software, the diffusion front could be tracked as a line, dividing a dark region of water penetration from a relatively brighter (unpenetrated) region. The penetration depth (d_p), as a function of time, was obtained by averaging the positions of ten points located at equal separation intervals along the diffusion front. This depth was used to make another estimate of D, and compare with the D values calculated from the mass gain. The same experimental configuration, albeit by imaging at higher magnification, also enabled the penetration of water through the fiber and matrix to be separately analyzed, enabling diffusion constituents for these individual microstructural constituents to be estimated.

6.3.2 Image analysis for sheath deformation

The image sequences from the *in situ* imaging were analyzed using a digital image correlation (DIC) technique [79] to characterize the local deformation (von Mises) strain in the sheath samples induced by the water penetration. Essentially, these strains are those due to the swelling deformation. The DIC algorithm could also estimate other deformation field parameters such as strain-rate and rotation tensors.

6.3.3 Diffusion coefficient (D) estimation

The diffusion coefficient was estimated on the basis of one-dimensional (1D) diffuson of water into the sample thickness from the adaxial surface (**Figs. 6.1a and 6.2)**. This estimation incorporated the measurements of mass gain and swelling as follows [77,78,80,81].

Fick's law for one dimensional diffusion is

$$\frac{\partial c}{\partial t} = D\frac{\partial}{\partial x}\left(\frac{\partial c}{\partial x}\right) \tag{6.2}$$

where, c is the concentration of the diffusant at location x, x is distance coordinate in the sample thickness (diffusion) direction, D is the diffusion coefficient and $\partial c/\partial x$ is the driving potential. Since in the present problem, the location of the adaxial surface changes during the diffusion due to the swelling arising from the water penetration, it is useful to define the various parameters related to **Eq. 6.2.** This is done in **Fig. 6.2** which gives a snapshot of the boundary condition and various surfaces during the diffusion [77,78].

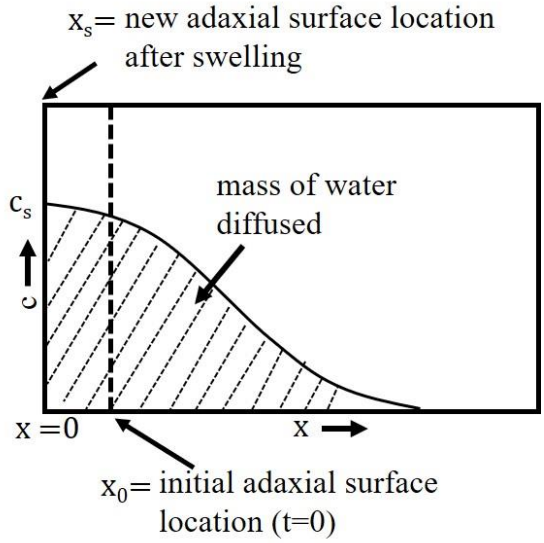

Figure 6.2 Schematic of coordinate system and boundary condition for the diffusion analysis.

The sheath sample is considered as a semi-infinite solid in contact with water of fixed concentration, c_s, on one side, the adaxial surface. The initial location of this surface, that is before the diffusion has begun, is x_0 (**Fig. 6.2**). Once the diffusion begins and the sample swells, the new

location of the adaxial surface is $x = x_s = 0$; where $x_0 - x_s = -z_s$, is the thickness change due to the swelling (**Fig. 6.3**). Note that $-z_s$ is measured in the experiments. The concentration boundary condition at the adaxial surface ($x = x_s$) throughout the diffusion is $c = c_s$. We take c_s to be the concentration of water that prevails in the sheath sample when it is fully saturated.

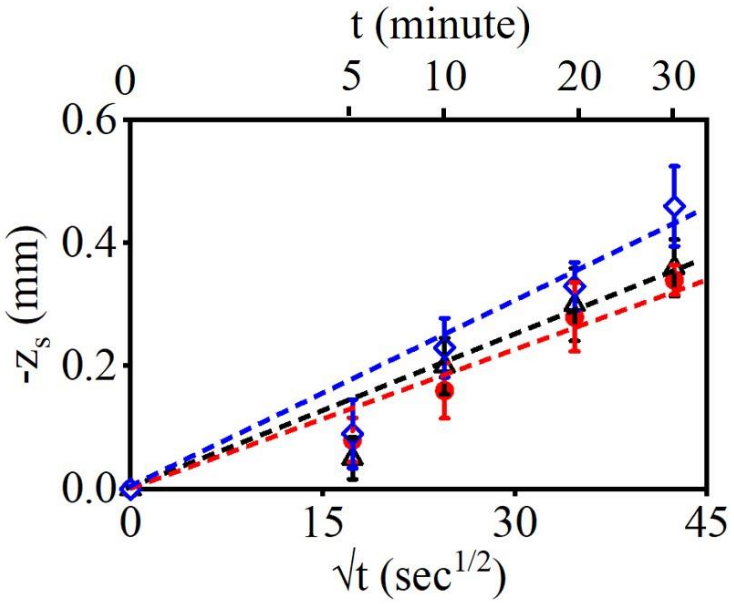

Figure 6.3 Swelling induced by diffusion of water. Sample thickness change induced by swelling ($-z_s$) plotted against square root of time, $\sqrt{t}$. The closeness of the straight-line fits is consistent with a parabolic expansion of the sample due to the water absorption.

Implicit in this formulation is the assumption that water saturation at the sample surface occurs essentially instantaneously at the beginning of the experiment, and that this c_s is maintained throughout the experiment. The value of c_s is obtained from the mass gain measurements as the mass of water per unit volume of the sample at saturation, that is after exposure of the sample to the water for a "long" time, see **Fig. 6.4**. **Figure 6.4** shows the variation of the mass gain per unit volume of the sample with time for three repeat water-exposure experiments. These experiments were performed for exposure times of 720 minutes. The data shows that the diffusion process slows down, and the mass gain becomes constant after a long exposure indicating saturation of the sample by the water. The average value of the mass gain per unit volume, for exposure times in the range of 600 minutes to 720 minutes, was found to be 0.55 gm/cm^3. This value is used for c_s when solving the diffusion equation.

The analytical solution to Fick's law for the 1-D diffusion case, with due consideration of the swelling, is now obtained as [77,78]:

$$\frac{c}{c_s} = \frac{1-erf\left(\frac{z}{2\sqrt{Dt}}\right)}{1-erf\left(\frac{z_s}{2\sqrt{Dt}}\right)} \tag{6.3}$$

where $z = x - x_0$.

By integrating the concentration profile over the penetration depth, the mass of water per unit area, m_t, that has diffused into the sample at time t is estimated as:

$$m_t = \frac{2c_s\sqrt{Dt}}{\sqrt{\pi}\left(1-erf\left(\frac{z_s}{2\sqrt{Dt}}\right)\right)} \tag{6.4}$$

The average value of $-\frac{z_s}{\sqrt{t}}$ is obtained from the slope of the swelling-thickness change plot (**Fig. 6.3**). **Equation 6.4** forms the basis for estimation of D from measurements of m_t and the swelling.

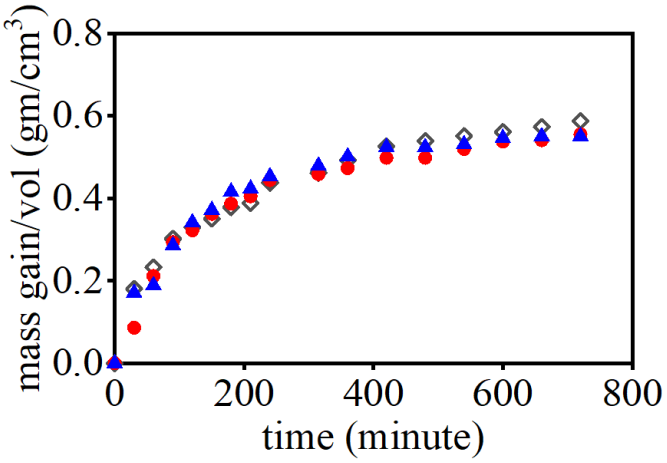

Figure 6.4 Variation of mass gain/volume with time used to estimate c_s.

6.4 Results

The mass gain experiments and *in situ* observations of water penetration have enabled quantitative characterization of the diffusion process in the palm leaf material and provided insights into the role of the sheath microstructure constituents (matrix, fiber) in influencing the diffusion.

6.4.1 Diffusion coefficient of water at room temperature (D_w)

Figure 7.3 shows the variation of $(-z_s)$ with $\sqrt{t}$ for three samples. The actual time *t* in minutes is also given along the top (horizontal) axis in the figure. The closeness of the straight-line fits to the data confirms a parabolic sheath expansion due to the water absorption. Based on this data, an average value for $\frac{-z_s}{\sqrt{t}}$ was obtained as $(8 \pm 0.8) \times 10^{-3}$ mm/sec$^{1/2}$.

Figure 6.5a shows the variation of m_t with time. The increase of m_t with time (**Fig. 6.5a**) is quite rapid initially before tapering off, as expected of a 1-D diffusion process [80,81]. The clustering of the data points in this figure, from five different experiments, is indicative of good repeatability. In order to estimate the diffusion coefficient, we fitted the data points from the initial phase of the diffusion experiments (**Fig. 6.5a**), between $t = 0$ and $t = 30$ minutes, using **Eq. 6.4** and the afore-estimated value for $\frac{-z_s}{\sqrt{t}}$. Based on this fitting, which was carried out with all the five experimental data sets, the diffusion coefficient (D_w) for pure water at room temperature was obtained as $(6.5 \pm 2.2) \times 10^{-4}$ mm^2/sec. The black dashed line in the figure is the curve fit using **Eq. 6.4** based on the average D_w value. This value should strictly be treated as an upper bound since it is based on a c_s boundary condition that corresponds to full saturation of the sheath sample with water ($t >> 30$ min.). If the swelling is neglected, then the diffusion coefficient is obtained as $(5.1 \pm 1.2) \times 10^{-4}$ mm^2/sec., an ~ 20% underestimate.

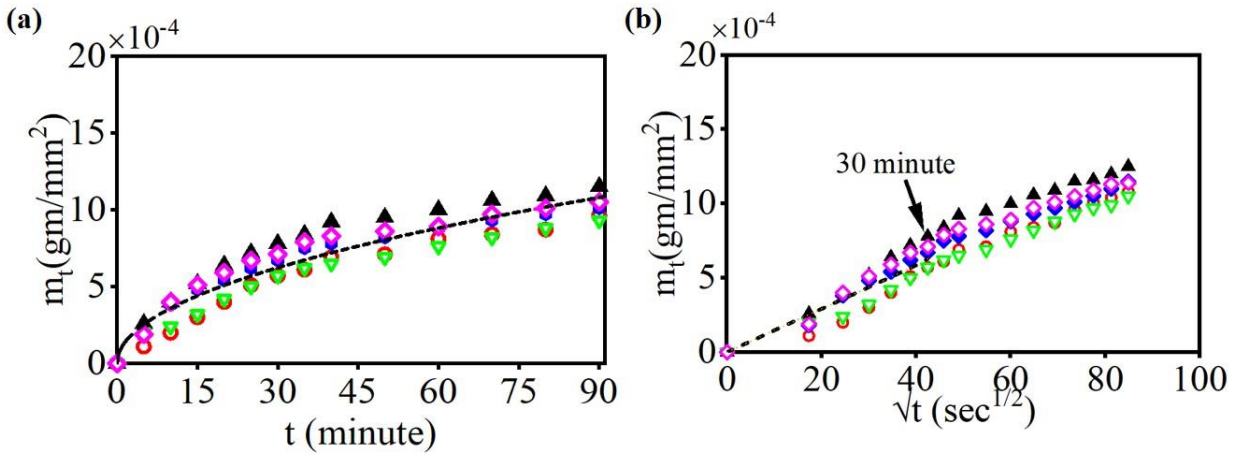

Figure 6.5 Results of mass-gain. (a) m_t vs t plot for water at room temperature for the five different diffusion trials. The initial mass of the sample before diffusion was approximately 0.1 gm. (b) Variation of mass gain (m_t) with square root of time $\left(\sqrt{t}\right)$. The very good linear fit of the data points in the initial diffusion phase (0-30 min.) supports 1-D diffusion in this phase. The slope of this straight line is $(14.8\pm4.7)10^{-6}$ gm/mm^2-sec$^{1/2}$. Note also a distinct change in the slope at t ~ 30 min.

The data from the initial phase of the diffusion (0-30 min.) alone is used in the above analysis since it is in this phase, the 1-D model underlying **Eq. 6.4** is expected to be valid. This can also be seen in **Fig. 6.5b**, wherein the mass gain data is replotted as m_t against $\sqrt{t}$. The very good straight line fit of the data in this figure for t in the range of 0 to 30 min. confirms a parabolic expansion consistent with 1-D diffusion. Note also the distinct change in slope in this figure for $t > 30$ min, indicative potentially of a deviation from 1-D transport at this point.

6.4.2 *In situ* observations of the diffusion

Figure 6.6 shows a sequence of images of water penetration into the sheath from the adaxial surface, as revealed by *in situ* observations made at different time intervals. A representative optical micrograph of the sheath sample (top left, $t = 0$ min) is also provided to show the location and distribution of the fibers in the sample. The subsequent images in the sequence are high-speed camera images, processed with ImageJ software, in order to track the permeation of water into the sample. The transverse and bottom faces of the sample in the image sequence are the sealant-coated regions, which are demarcated by the dotted green line. In the images, the region where the water has permeated appears black in color while the un-permeated regions are white in appearance.

The boundary between the black and white regions thus corresponds to the water diffusion-front and is highlighted with a pink-dotted line. The images reveal not only the progression of the diffusion front, but also various mesoscopic details of the water transport.

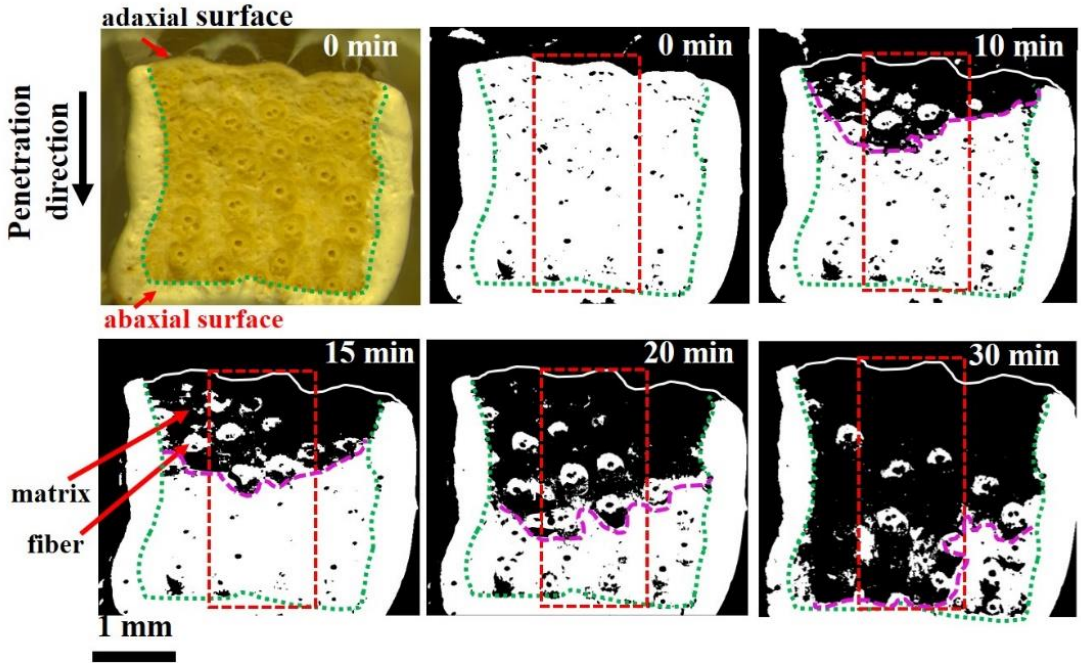

Figure 6.6 Image sequence showing water penetration into the sheath. (Top left) Optical micrograph of thickness cross-section before the diffusion, and corresponding gray scale image (top row, middle) generated by ImageJ. Note the fibers and matrix. The green dotted line demarcates the sheath region that is subjected to the water exposure, from the outer region coated with the rubber sealant. The sequence of five gray-scale images shows the imaged surface at t = 0, 10, 15, 20 and 30 minutes after the beginning of the diffusion. The dotted pink line tracks the position of the diffusion) front. The region within the red box is wherein the penetration depth (d_P) is measured.

The *in situ* images (e.g., **Fig. 6.6)** enabled us to directly measure the depth of water penetration (d_p) into the sample. For this purpose, and to eliminate sample edge effects, measurements of the diffusion-front location (pink) were made at ten different points in a central region of the sample, demarcated by the red boxes in **Fig. 6.6**. d_p was then estimated as the mean of these measurements, from three different samples. It is worth detailing important features of the water penetration in the figure. After 10 min of exposure, the water has entered about one-fourth into the sample thickness, mainly though the matrix. However, the penetration is not uniform as reflected in the measured depth values of 1.05 ± 0.28 mm. Many of the fibers still appear bright in the images

indicating that the water has not penetrated them although the surrounding matrix region is saturated with water. After 15 min exposure, the water has penetrated about one-third of the way into the sample thickness. The fibers close to the adaxial-surface are now beginning to darken indicating that the water is now diffusing into them. After 20 min, the water has penetrated ~ 2 mm into the sample thickness, and the fibers close to the adaxial-surface are now completely saturated with water. It is evident from the image sequence that water diffusion through the sample is not uniform, occurring significantly more rapidly through the matrix than through the fibers. This strongly suggests that the transport process through the matrix controls the overall diffusion.

Figure 6.7 shows the variation of d_p with time (data points), as obtained from the *in-situ* imaging. Also shown in **Fig. 6.7** is the value of d_p, as predicted using the diffusion coefficient (D_w) derived from the mass gain experiments. This prediction, shown as a red band between the two dotted curves, represents the range of d_p corresponding to the upper and lower limits of the measured D_w. In making this prediction, we have taken $2\sqrt{D_w t}$ as the measure of d_p as is typically done [80,81]; note that this corresponds to the depth over which the concentration is at least ~15% of the maximum (saturation) concentration (c_s). D_w can also be estimated from the *in-situ* measurements of d_p. This gives for D_w, a value of 6.2×10^{-4} mm^2/sec, which is close to that ($(6.5 \pm 2.2) \times 10^{-4}$ mm^2/sec) obtained from the mass-gain. It may be noted here that predictions made of d_p, neglecting the swelling contribution, fall below the lower limit (penetration) curve in **Fig. 6.7**. Hence, if swelling is neglected, D_w would be underestimated.

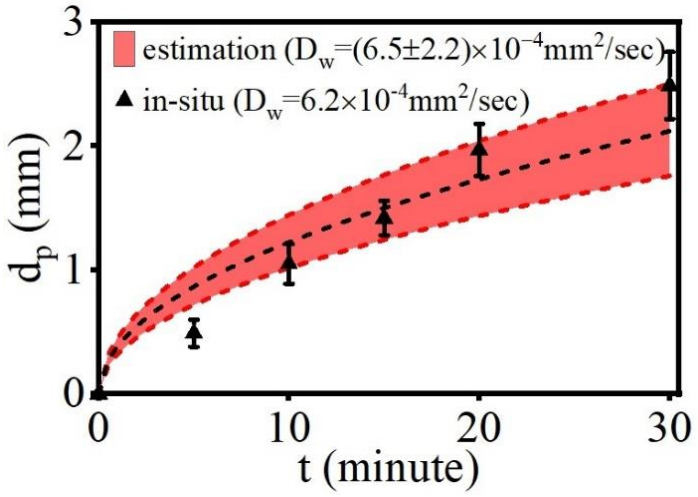

Figure 6.7 Depth of water penetration (d_p) with time. Data points are from the *in situ* imaging. The black dotted line is a curve fit of the data ($d_p = 2\sqrt{D_w t}$, 1-D diffusion)from which D_w is estimated as 6.2×10^{-4} mm^2/sec. The red band gives the predicted upper and lower limits of (d_p) for $D_w = (6.5 \pm 2.2)\times10^{-4}$ mm^2/sec; this D_w value is that obtained from the mass gain experiments.

The *in situ* measurements of the water penetration are thus consistent with those derived from the mass gain experiments. It is also worth noting in **Fig. 6.7** that the first two direct measurements of d_p are located near the estimated lower limit, while the last two measured points are close to the upper limit. This indicates that in the early stage of the diffusion, the swelling contributions are less critical than in the latter stage.

6.4.3 Penetration of water in fiber and matrix

The in-situ observations of **Fig. 6.6** have shown that the diffusion of water through the sheath is not uniform, occurring much faster through the matrix than the fibers. We now utilize these types of observations at high magnification to discriminate and resolve the water penetration through the fiber and matrix, individually, and estimate diffusion coefficients for the fiber (D_f) and matrix (D_m).

Figure 6.8 shows two sets of high-magnification images wherein penetration of water through two individual fibers could be tracked as a function of time. The images were processed with ImageJ as before to demarcate the penetrated and unpenetrated regions. In these images, the fiber-

boundary is highlighted with a red dashed line and the water penetration direction is indicated with an arrow. Times t_0 and t_1 correspond to the instants when the water begins to penetrate each fiber, respectively, and $t_0 + 7$ mins and $t_1 + 9$ mins to the instants when the diffusion front has completely traversed the corresponding fibers. Similarly, **Fig. 6.9** shows penetration of water through a selected matrix region. The diffusion front (dotted red line) is seen to traverse this region in ~ 2 minutes.

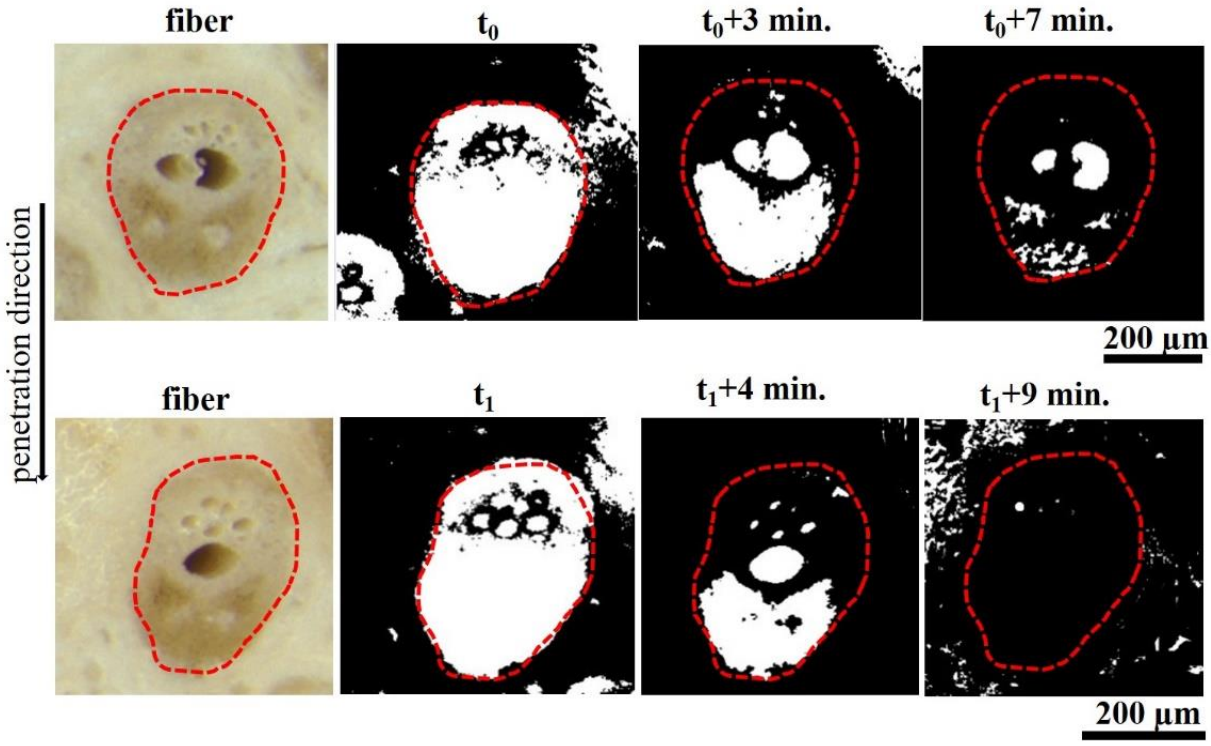

Figure 6.8 Select frames from image sequences showing penetration of water through two different fibers. The fiber boundary is highlighted by red dashed line. t_0 and t_1 represent the times when water begins to penetrate each fiber. The dark areas are the regions where water has penetrated. The leftmost frames in each row are optical micrographs of the respective fiber cross-sections.

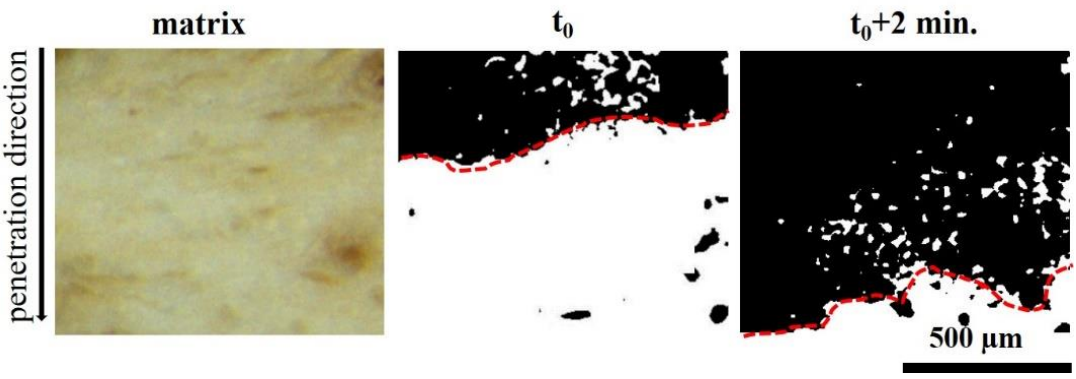

Figure 6.9 Select frames (right two frames) from an image sequence showing penetration of water through matrix region. The location of the diffusion front is demarcated by red dotted line. The black region in the frames is the region of water penetration. The left image is an optical micrograph of the same matrix region.

Based on such penetration time measurements from six different fibers and matrix regions, and noting that the diffusion front travels a distance proportional to $\sqrt{Dt}$ in time t [82], we estimated $D_m/D_f = 12$. Since the diffusion through one of the microstructural constituents, viz., the matrix, occurs much faster than through the other constituent, viz., the fiber, and, therefore, matrix diffusion regulates the overall diffusion process, we can write another equation (Eq. 5) linking D_m and D_f:

$$D_m V_m + D_f V_f = D_w \tag{6.5}$$

This equation assumes that the leaf-sheath is a composite with its two phases, viz., fiber and matrix, arranged parallel to each other along the diffusion direction.

Solving **Eq. 6.5**, for $D_m/D_f = 12$, $V_f = 0.27$, $V_m = 0.73$, and $D_w = 6.5 \times 10^{-4}$ mm^2/sec, we get the average diffusion coefficients for the matrix and fiber, respectively, as $D_m = 8.63 \times 10^{-4}$ mm^2/sec and $D_f = 7.19 \times 10^{-5}$ mm^2/sec. The diffusion coefficient for the fiber is thus an order of magnitude smaller than the coefficient for the matrix. The D_m value is however close to D_w for the sheath confirming that the matrix controls the overall diffusion of water through the sheath.

These diffusion coefficient values for the matrix and fiber are consistent with the earlier *in situ* observations which showed much more rapid penetration of the water through the fiber than the matrix. Importantly, they also suggest an experimental (observational) approach that can be

applied, broadly, to study diffusion through individual microstructural constituents of plant materials and woods.

6.4.4 Material deformation

The image sequences from the *in situ* observations were digitally correlated to estimate the local deformation (von Mises effective strain) in the areca sheath arising from the water diffusion (**Fig. 6.10**). A plane strain condition is assumed, since measurements showed negligible change in the sample dimension into the plane. **Figure 6.10a** is an optical micrograph of the sample thickness cross-section prior to the diffusion of water; note the location and size of the fibers before the water enters the sample. **Figures 6.10b-d** show the sample cross-section, with the strain-map superimposed, at $t = 10$, 20 and 30 minutes, after the adaxial-surface is exposed to the water. It is clear from the figures that the strain, locally, is quite large and highly non-uniform. And the swelling-induced deformation field is long-range, extending throughout the sample. After 10 minutes of diffusion, the maximum strain in the matrix is ~3, while in the fibers, it is ~1. With further diffusion, the strain in both the fibers and the matrix increases, reaching values as high as ~ 8 after 30 minutes of diffusion. But the strain in the matrix is always much higher than in the fibers. These large swelling-induced strains, and local high strain gradients between the matrix and fiber, will be detrimental to the structural integrity of the materials. For example, they can cause the fiber to decohere from the matrix. Also, the stiffness and strength of the sheath material will be lowered [68].

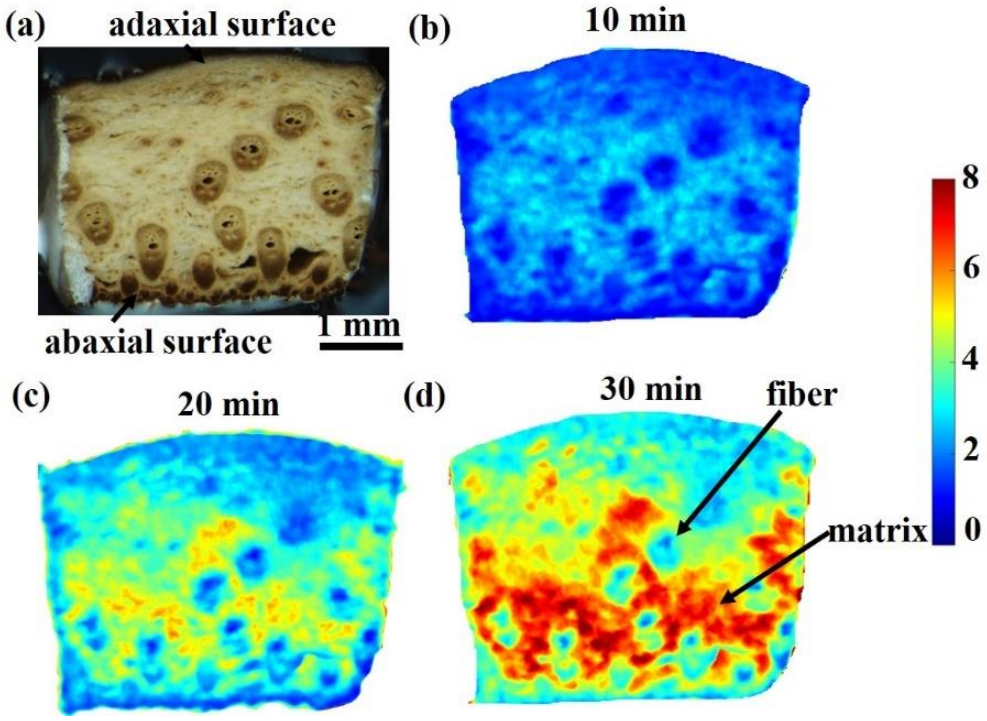

Figure 6.10 Deformation of sheath due to water diffusion. (a) Optical micrograph of sheath cross-section before diffusion. The images (b) to (d) show the strain after 10, 20 and 30 minutes of diffusion, respectively. Diffusion occurs from the adaxial surface downward.

6.4.5 Effect of NaCl concentration and temperature

The main applications domain of areca sheath is in foodware products like plates and bowls . In this context, there is interest in knowing how temperature and salt (NaCl) concentration influence the water diffusion. These parameter effects were examined by carrying out the mass gain and swelling measurements at different temperatures and NaCl concentrations, and estimating the diffusion coefficients.

Figure 6.11 summarizes the results of these experiments in the form of a plot of D_T^S/D_w against salt concentration (wt %) at different temperatures**,** where D_T^S is the diffusion coefficient at specific salt (S) concentration and temperature (T), and (D_w) is the diffusion coefficient measured for pure water at 0% salt concentration and room temperature (RT). As might be expected, the diffusion coefficient for the pure water as well as the various salt solutions show a strong increase with temperature – two- to three- fold between RT and 70^0 C. The largest increase is seen to occur for T = 70^0C and 5% salt concentration, wherein D_T^S is 3.5 times D_w. This surprising finding of a

local maximum in the diffusion coefficient at salt concentration of 5% was found to occur for all the three temperature conditions studied. At the other concentrations, that is greater or less than 5%, the diffusion is slower. A possible reason for this type of dependence of D_T^S on salt concentration is viscosity. It is well-known that salt increases the viscosity of water [83], with an associated effect on the diffusion**.** However, further experimentation is needed to better understand this peculiarity in the diffusion process.

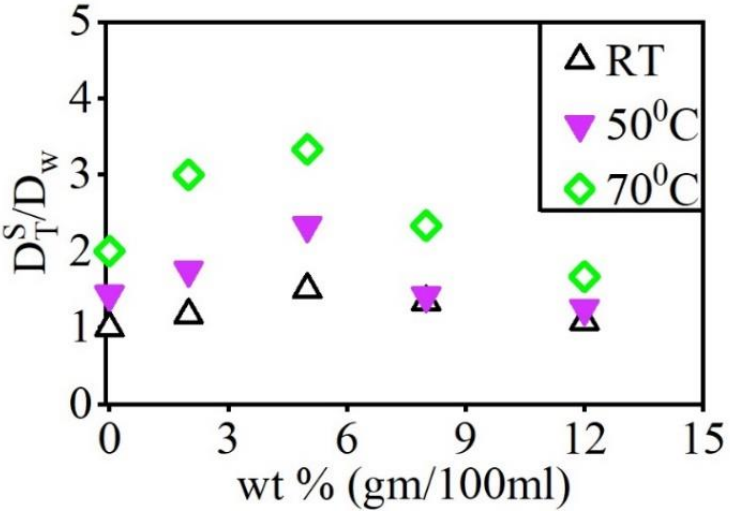

Figure 6.11 Diffusion coefficient (D_T^S) of salt solution and water at different temperatures (T) and NaCl (S) concentrations. The D_T^S is normalized by diffusion coefficient of water at room temperature (D_w).

6.5 Discussion

The study of water transport through areca palm leaf-sheath using *in situ* imaging of the transport process, complemented by mass gain measurements, has yielded important insights into water diffusion through a hierarchically structured plant material. It has also enabled quantitative estimation of diffusion coefficients for water transport through both the sheath (ensemble), as well as its microstructural constituents (fiber and matrix).

The mass gain measurements have shown that the diffusion coefficient (D_w) for pure water through the leaf-sheath is $(6.5 \pm 2.2) \times 10^{-4}$ mm^2/sec. This value is of the same order, but somewhat higher than the diffusion coefficients for water in various woods, be it in liquid or vapour forms. For example, the diffusion coefficients reported for moisture in radial direction (drying

experiments) in hard woods - black tupelo, bass and red oak - are 1.8×10^{-4}, 1.9×10^{-4} and 1×10^{-4} mm^2/sec, respectively. Similarly, diffusion coefficients for moisture in soft pine wood in radial and tangential directions are 1.1×10^{-4} and 0.67×10^{-4} mm^2/sec, respectively [70,84]. Effective diffusion coefficients reported are also roughly similar: for liquid water in pine wood, oak and teak wood – the values are 0.68×10^{-4}, 0.26×10^{-4} and 0.25×10^{-4} mm^2/sec, respectively [74]. The similarity in the diffusion coefficient values for the leaf-sheath and woods is most likely a result of the broad similarity in their underlying structures [33,38].

In our estimation of the diffusion coefficient, the effect of material swelling due to water absorption has been incorporated. The estimated D_w value of $(6.5 \pm 2.2) \times 10^{-4}$ mm^2/sec, with swelling effects included, is ~ 30% greater than the D_w value $(5.1 \pm 1.2) \times 10^{-4}$ mm^2/sec obtained when the swelling is neglected. Furthermore, the direct *in situ* measurements of water penetration depth **(Fig. 6.7)** are consistent with the predictions made by incorporating the swelling effects in a 1-D diffusion model. The results attest to the need for including the swelling parameter in diffusion analysis with plant materials.

The *in situ* observations have revealed that the diffusion process in the sheath is quite non-uniform (**see Figs. 6.6, 6.8 and** 6.**9),** with the water permeating through the matrix much more rapidly than through the fiber. These observations have also enabled, via tracking of progression of the diffusion front through the individual microstructural constituents, estimation of separate diffusion coefficients for water transport through the fiber (D_f) and matrix (D_m). D_f is found to be one order of magnitude smaller than D_m, confirming the conclusion derived from qualitative visual *in situ* observations of water transport through the sheath microstructure. D_m is, however, found to be similar to D_w, the diffusion coefficient for the composite sheath. This strongly suggests that the matrix diffusion controls the overall water transport process through the sheath. The much slower transport of water through the fiber is most likely due to the lignified and thicker cell walls therein [14,26]. This type of difference in the water penetration rate between the fiber and matrix is likely to hold true for most plant materials that have a fiber-matrix type composite structure.

The non-uniformity of the diffusion, a direct consequence of the heterogeneity of the sheath microstructure, is also reflected in the material deformation. The swelling-induced strain is much greater in the matrix (~ 8), due to the greater water penetration therein, than in the fiber (~ 2) see **Fig. 6.10**. Additionally, since the matrix is less stiff than the fiber, it should be expected to deform

more, contributing to the greater strain. Likewise, differences in stiffness between the epidermis material layers, adjoining the sheath abaxial and adaxial surfaces, and the bulk material in the sheath interior (parenchyma tissue) [33,34], may explain why the swelling and strain are lower along these outer surfaces (**Fig. 6.10**). The large strains and local strain gradients arising from the swelling and non-uniform diffusion are likely to be detrimental to the structural integrity of the leaf material. It can also cause decohesion between the fiber and matrix, with adverse effects on sheath life; as well as a lowering of the stiffness and strength**.**

We can use the measured D_w to make an estimate of sheath life or equivalently foodware product life. Based on the D_w value of $(6.5 \pm 2.2) \times 10^{-4}$ mm^2/sec obtained from the mass gain experiments, and $d_p = 2\sqrt{D_w t}$, it is seen that the water front will traverse the entire sheath thickness (~3 mm) in ~ 60 mins. This can be taken to be an upper bound on the sheath life. In fact, this time is remarkably close, in fact identical, to product life times (60 min.) reported by areca foodware manufacturers. This life estimate is an upper bound since it does not include the effects of swelling-strain on structural integrity. The results do give some pointers as to how areca sheath foodware life can be improved. One possible strategy is to coat the sheath adaxial surface, the surface typically in contact with the food, with a benign hydrophobic coating. Such a coating will increase the time needed for the water to start penetrating the sheath as the surface will not wet immediately. In fact, such a coating may be provided naturally by the sheath material itself. Preliminary experiments show that the areca sheath when heated, secretes a hydrophobic wax layer on the adaxial surface, which can potentially be used to increase the sheath-product life. Another possibility involves some pre-compression of the sheath prior to the forming process, as a means to reduce the diffusion. Preliminary diffusion measurements with foodware have shown that the water diffusion is slower on the slant surface of the plate than at the center. The sheath is compressed more on the slant surface than in the center, as seen in the smaller thickness measured along the slant surface compared to the plate center. Furthermore, diffusion experiments with raw sheath have also shown that pre-compression of the sheath in the thickness direction prior to the experiments slows down the diffusion process.

While water penetration into the sheath decreases the strength of the sheath, it does increase the sheath formability, a definite plus for foodware manufacturing by pressing. Typically, manufacturers subject the sheath to a moisture treatment for 12 hours before conducting the

forming operation. If an optimum moisture content for improved formability is established, then we can use the diffusion results to calibrate the minimum water-exposure time needed to achieve enhanced sheath formability. A preliminary analysis using results from prior work indicates that this exposure time can be < 2 hours, enabling large gains in forming-process throughput and productivity**.**

With regard to parametric effects on the diffusion, the effects of temperature and NaCl concentration have been examined since they are also quite relevant for foodware applications. In the temperature range of 25^0 to 70^0 C, the diffusion coefficient shows a strong 3-fold increase with temperature (**Fig. 6.11**). The effect of salt concentration on diffusion coefficient is the more surprising, with a peculiar local maximum in diffusion coefficient observed at an NaCl concentration of ~ 5 wt% (**Fig. 6.11**). Analogous maxima have been observed in diffusion of KCl and NaCl in water, near the saturation concentrations of these salts, a characteristic attributed to formation of molecular clusters [85]. Likewise, it has been observed that a loss of water in vegetables, which occurs by osmotic dehydration, also a transport process, is also highest at around 5% NaCl concentration [86]**.** In the present instance, we speculate that the diffusion maximum is due to changes in the solution viscosity with NaCl concentration. Typically, an increase in the concentration gradient increases the diffusion rate while a viscosity increase has the opposite effect[87]. This differing dependence could result in a local maximum in the diffusion coefficient vs concentration curve.

Our results suggest that by combining material structure characterization, with *in situ* observations of liquid transport and mass gain/dimension changes, it will be feasible to obtain a comprehensive understanding of liquid transport mechanisms in plant materials and woods. They also suggest that these materials can be treated as composites for analysis of both mechanical and transport properties.

The diffusion characterization methodologies, such as the mass gain and *in situ* observational approaches, and swelling characterization, presented herein are quite general and can be applied to various plant and herbaceous materials. They should be of value for studying diffusion in natural materials with due consideration of microstructural features, diffusion anisotropy (e.g., in-plane vs through-thickness diffusion), and parametric effects such as due to oils and surface coatings.

We hope to examine some of these problems in the near future; as well as apply the results obtained to enhance structural integrity, product life and forming of areca-sheath foodware.

6.6 Conclusion

Diffusion of water into a model plant material system – areca palm leaf-sheath – was studied experimentally using *in situ* observations of the water transport at high resolution, and mass gain measurements. The characterization has provided measurements of the diffusion coefficient not only for the composite ensemble, but also for water transport through the microstructural constituents, viz. fibers and matrix. Water diffusion through the sheath is found to be non-uniform, being an order of magnitude faster in the matrix than in the fibers. Consequently, the matrix diffusion controls the overall transport process. The effect of material swelling due to water absorption is included in the diffusion analysis, unlike in prior studies. It is shown that the swelling effect on the diffusion is considerable in these plant materials, and, if neglected, can lead to significant error, as much as 30%, in the estimation of the diffusion coefficient. The non-uniformity in the diffusion, and the water absorption, cause large (local) strains in the leaf-material. This strain field is also non-homogeneous, the strain values being significantly higher in regions of greater water penetration. The results suggest that if water diffusion controls the sheath (or sheath product) life, then a typical 3 mm leaf-sheath will lose its structural integrity in ~ 60 minutes. The large dilatation strains (4-8) due to swelling could also lower material stiffness and strength, i.e., structural integrity, thus adversely impacting product life. The diffusion data provide a basis also for estimating optimum water exposure times for improving the formability of these materials for product manufacturing.

The diffusion characterization and analysis techniques developed in the study can be applied to the broad class of plant materials and woods, enabling improved understanding of both microstructural and parametric (e.g., osmotic potential, temperature) effects on liquid transport processes in these materials.

7. REDUCING DIFFUSION OF WATER IN PALM SHEATH BY SECRETION OF SURFACE WAX

7.1 Abstract

Diffusion of water into areca sheath has an adverse impact on structural integrity of the sheath and reduces holding capacity of areca foodware, with lower product life resulting. Building on the prior characterization of water diffusion in areca sheath, we examine the possibility of reducing this diffusion by creating a natural hydrophobic layer of wax on the surface of sheath. When areca sheath is heated to a temperature > 80^0 C, a hydrophobic natural wax layer is found to be secreted onto the adaxial surface of the sheath. This can act as a barrier between the water and the sheath, delaying the diffusion process. We characterize the water diffusion in the presence of the adaxial wax layer using the diffusion measurement techniques described earlier. The measurements show that both mass gain and diffusion coefficient decrease when the sheath is subjected to a high-temperature treatment prior to the diffusion process. The diffusion coefficient for water decreased from $(6.5 \pm 2.2) \times 10^{-4}$ mm^2/sec to $(2.7 \pm 1.3) \times 10^{-4}$ mm^2/sec when the sheath was heated to 120^0C to secrete the wax on to the abaxial surface. As a result, the product life of 3 mm sheath increased two-fold, from ~60 minutes to ~180 minutes. We also report on the details of the formation of the wax layer and its dependence on the temperature. The results suggest opportunities for increasing foodware life by optimizing the wax secretion or use of other similar type of natural hydrophobic coatings.

7.2 Introduction

In the foodware applications, the product life is determined largely by the time taken for semi-solid and liquid elements (e.g., water, oils) in the food to penetrate through the walls of the foodware, thereby causing structural degradation of the sheath. It has been claimed, mainly by areca product manufacturers, that areca foodware can hold semi-solid food for approximately 60 minutes, before a plate or bowl becomes soggy due to liquids (e.g., water) seeping through the ~ 3 mm thick sheath wall. Discussions with manufacturers suggest that if this product life can be enhanced to 120 or 180 minutes by reducing the liquid seepage (diffusion), then areca foodware can become more competitive economically.

In **chapter 6**, we studied diffusion of pure water through the adaxial surface of palm sheath using mass gain measurements. It was shown using various types of diffusion measurements that water takes ~60 minutes to penetrate through a sheath of nominal thickness 3 mm. One possible strategy for reducing diffusion is to coat the adaxial surface of the sheath, the surface directly exposed to the food, with a hydrophobic coating. Such a coating should increase the time required for water to begin the penetration into the sheath as the surface will not wet immediately.

Edible film coatings made from hydrocolloids, wax and lipids have received attention in recent years for use as coatings in foodware and edible packaging because of their eco-friendly nature and health considerations [88–90]. Wang et al fabricated a superhydrophobic coating for commercial plastic foodware using FDA-approved edible materials such as Carnauba palm wax and bee wax [91]. They also demonstrated that carnauba palm wax and bee wax are non-toxic even at high concentrations. This suggests the possibility that adaxial surface of palm sheath could be modified by coating the surface with Carnauba palm wax or some other edible wax. Most palm trees contain wax in leaf and sheath, and the areca palm is no exception. This fact is likely "anecdotally" known to manufacturers. In Carnauba palm, the wax layer is found in both surface of leaf and sheath. To extract Carnauba wax, the leaves and sheath are collected, dried in the sun, and then wax is obtained from their surfaces by "beating or pounding" the plant material [92–94]. This provides the well-known Carnauba wax which is used in in products such as automobile waxes, shoe polishes, dental floss, food products (such as sweets), and floor and furniture waxes, often in combination with bee wax and turpentine.

Areca sheath contains 4-6% wax, see **Chapter 3**. If this wax can be secreted out onto the adaxial surface, then it could become an intrinsic diffusion barrier obviating the need for external wax or other similar coatings. We show here that this can indeed be done - creation of a hydrophobic wax layer on the adaxial surface by secretion from sheath interior - by heating the sheath to higher temperatures. We demonstrate the secretion of the wax layer by SEM, contact angle measurement and FTIR. Detailed diffusion measurements paralleling those reported in **Chapter 6** are done to examine the influence of the wax layer on the diffusion process and product life.

7.3 Method

We studied the effect of temperature on the diffusion of water through adaxial surface as this is the surface of the foodware that comes into contact with the food. Prior to the diffusion experiments, the sheath samples were heated in an oven to different temperatures in the range of 80^0C to 200^0C for 3 minutes. **Figure 7.1** shows optical images of the adaxial surface after this heating. The sheath surface is seen to become darker as the temperature rises. The temperature (T) range of 80^0C to 200^0C was chosen based on the melting temperature of wax (70-80^0 C) and the degradation temperature of the sheath (~250^0 C); this is further discussed later in the chapter. After subjecting the sheath to the heat treatments, each sample was coated with water-resistant paint on its sides and on the abaxial surface, as described in **chapter 6**, prior to mass-gain diffusion experiments. The diffusion measurement procedures are the same as those described in the previous chapter. We used three samples for each temperature to get an average diffusion coefficient.

We performed thermogravimetric analysis (TGA) to estimate the thermal degradation temperature of the sheath, based on which the maximum temperature to which the sheath was heated was decided. We also performed SEM, Fourier Transform Infrared Spectroscopy (FTIR), and contact angle measurements on adaxial surface of the sheath to detect the wax secreted on to the surface and its characteristics.

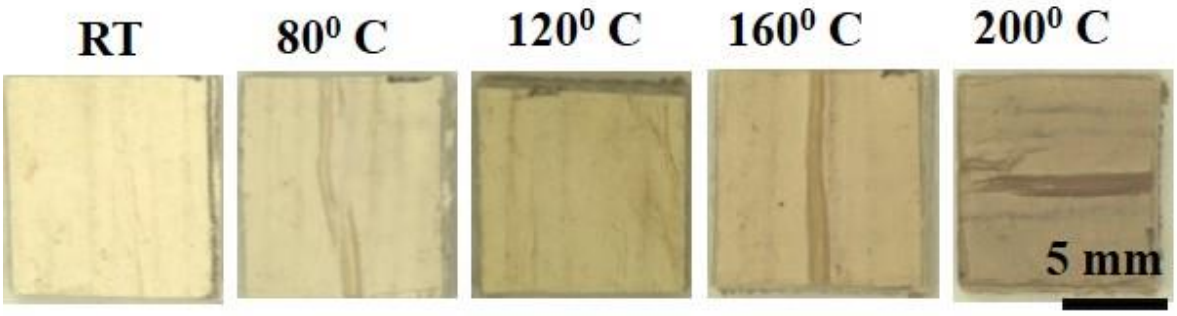

Figure 7.1 Adaxial surface of sheath after 3 minutes of heating to various temperatures. RT is the room temperature sample.

7.3.1 Thermogravimetric analysis (TGA)

Thermogravimetry (TGA) has been widely used to investigate thermal degradation of plant materials. TGA was performed on areca sheath samples to obtain the thermal degradation temperature. This was used to establish the upper limit on the thermal treatment temperature for

wax-secretion. TGA measures the change in the mass of sample as a function of temperature rise. The experiment was carried out with a Perkin Elmer TGA, with temperature range from room temperature to 1000^0 C. At the start of the experiment, nitrogen gas was flowed in to create an inert atmosphere, remove gaseous and condensation products, and minimize chemical interactions with the testing sample.

For the TGA, a 0.2 gm sample of the areca sheath was heated in a ceramic crucible. The sample was first held at constant temperature of 50^0 C for 5 minutes for removing hygroscopic water. The temperature was then ramped up at 10 °C/min to a maximum temperature of 450^0 C. The mass of the sample (measured) is plotted against temperature in the form of a mass-residue plot (**Fig. 7.2**). The mass residue curve shown in the figure represents the percentage of mass of the sample that remains after mass loss at different temperatures. The loss of weight is initially slower (up to 200^0 C); this region corresponds to the region of removal of moisture and other volatile substances. In this temperature range, the wax does not vaporize as most plant-based waxes become vapor at > 250^0 C, see also **Fig. 7.2**. The rapid loss of weight after approximately 250^0 C indicates the beginning of the degradation/burning of sheath components such as hemicellulose, cellulose, lignin, and wax among others [95,96]. At the end of the heating process (450^0 C), about 30% of the solid residue is left as ash. For the wax-secretion and diffusion experiments, we heated the sheath to a maximum of 200^0C based on the TGA analysis. This temperature is ~ 50^0 C lower than the wax degradation temperature (250^0 C).

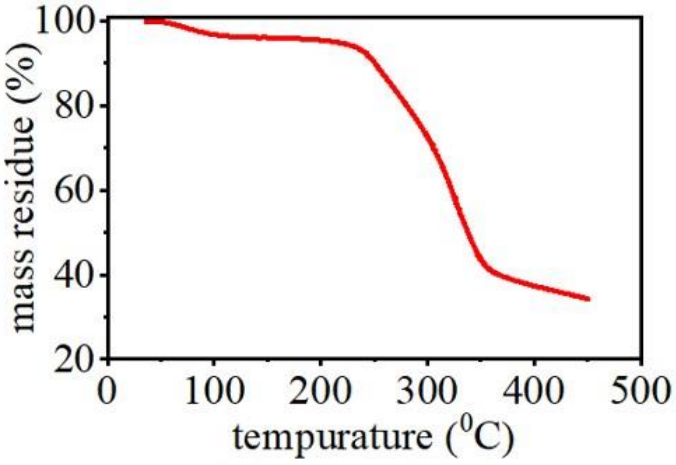

Figure 7.2 TGA analysis on sheath adaxial surface. The curve tracks the residual mass of the sheath (% residue) after heating to various temperatures.

7.3.2 Contact angle measurement

A Rame-Hart Goniometer was used to measure the contact angle of water on the sheath adaxial before and after the heat treatment. A 5 µl water droplet of was placed on the sheath surface, and an image of the droplet was captured within 2-3 seconds. For the imaging, the drop was illuminated with a fiber optic illuminator. The contact angle (θ) of water on the adaxial surface of the sheath was measured from the captured images using ImageJ, an open-source imaging software.

7.3.3 Fourier-transform infrared spectroscopy (FTIR)

The chemical functional groups constituting the adaxial surface of the sheath were investigated using FTIR. A Thermo-Nicolet Nexus 470 spectrometer with MCT-A detector and KBr beam splitter was used for the FTIR experiments. The surface of the sheath was scanned in absorbance mode at a spectral resolution of wavenumber 4 cm^{-1} between 800 cm^{-1} and 4500 cm^{-1}. OMNIC software was used to process the spectrum. The specific functional groups on the surface were identified from the positions of the peaks in the FTIR spectrum.

7.4 Results

7.4.1 Mass gain and diffusion coefficient (D_w)

The diffusion coefficient for water transport through the sheath, with adaxial wax layer, was obtained using mass gain measurements as before (**Chapter 6**). All experimental and sample details are same as in the prior diffusion study. The sheath samples were heated to various temperatures in the range of 50 to 200^0 C before the diffusion measurements. With sheath samples exposed to 80^0 C, 120^0 C, 160^0 C and 200^0 C for 1 minute, there was no significant difference in the mass gain data relative to the room temperature (RT) sample. This suggested that the diffusion coefficient was unchanged.

Upon repeating the water diffusion experiments with the sheath heated to the aforementioned temperatures for a longer 3-minute duration, we observed a decrease in the mass gain relative to that of the room-temperature (RT) sample. **Figure 7.3a** shows the mass-gain experiment results for the 3-minute heat treatments. As before, and typical of a 1-D diffusion process, the increase of m_t with time (**Fig 7.3a**) is quite rapid initially before tapering off [80,81]. It can be seen from the

figure that that the amount of mass gain is much lower in the sheath heated to 80^0 C compared to the RT sample. Furthermore, this mass-gain decrease relative to the RT sample is essentially the same with all the samples exposed to T > 80^0 C.

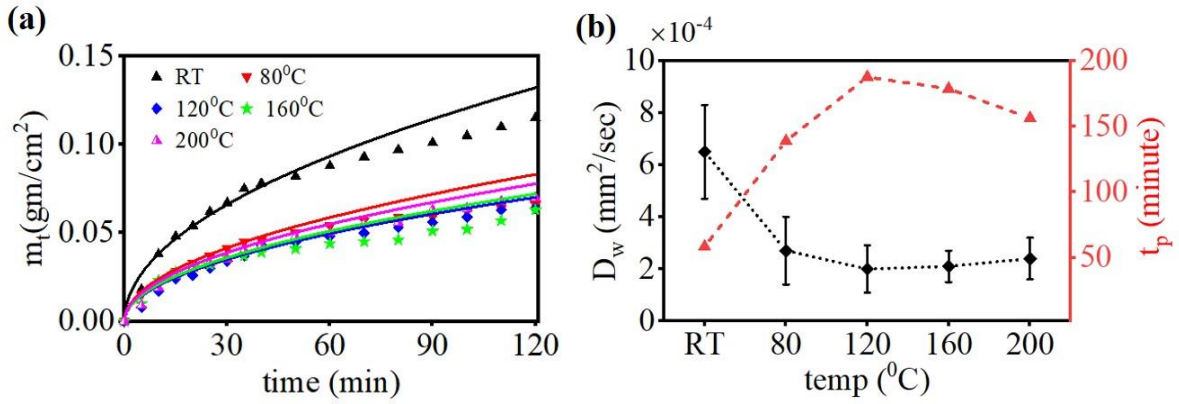

Figure 7.3 Mass gain and diffusion measurements with heat-treated sheath samples (a) Plot of m_t vs t for water in contact with adaxial surface (b) Diffusion coefficient (D_w) (left axis, black data points) and time t_p for water to penetrate through a 3 mm thick sheath (right axis, red data points), for various sheath heat treatment temperatures.

In order to estimate the diffusion coefficient, we fitted the data points from the initial phase of the diffusion experiments (**Fig 7.3a**), between $t = 0$ and $t = 30$ minutes using **eq. 6.2 (chapter 6),** and combined this with estimation of the swelling parameter $\frac{z_s}{\sqrt{t}}$. The data from the initial phase of the diffusion experiment (0-30 min.) alone is used in the analysis since it is in this period, the 1-D model underlying **eq. 6.2** is expected to be valid **(ref)**. We measured z_s for the sheath as before after exposing it to water for 30 minutes, from which $\frac{z_s}{\sqrt{t}}$ was calculated at $t = 30$ minutes. This estimate of the swelling at one specific time is justified by the earlier observations that z_s is parabolic with t (**Chapter 6**). Here, z_s is a negative number as the free sample surface moves outward, in a direction away from the sample thickness (**Chapter 6**). The average values of $\frac{z_s}{\sqrt{t}}$ for the various sheath samples (heated to different T) are given in **Table 7.1.** It is seen from the table that there is a significant reduction in swelling between the room temperature (RT) and T = 80^0 C sample, but little change beyond this temperature. c_s was measured, for the boundary condition as before, from the water concentration in the sheath sample when it is fully saturated, that is after

12 hr. of water exposure. In the present case, the value of c_s is 0.55 gm/cm^3 and the same for all the sheath samples (different T).

Table 7.1 Swelling parameter for the various heat-treated sheath samples (3-minute treatment).

Temp (^{0}C)	$-Z_s/\sqrt{t}$ (mm/sec $^{1/2}$)
RT	0.0082
80	0.0052
120	0.0042
160	0.0047
200	0.0045

In the previous chapter, the average diffusion coefficient (D_w) for pure water at room temperature was obtained as $(6.5 \pm 2.2) \times 10^{-4}$ mm^2/sec based on curve fitting the mass-gain data from three repeat experiments (solid line in **Fig 7.3a**). The same analysis and curve fitting procedure was used to get the diffusion coefficients with the different heat-treated samples, see **Fig 7.3a**. **Figure 7.3b** shows the diffusion coefficient, thus estimated, as a function of temperature (black data points). This value is strictly regarded as an upper bound as before because it is based on a c_s boundary condition that corresponds to full saturation of the sheath sample with water (t > 30 min.). It can be seen from this figure that the diffusion coefficient decreases significantly in the sheath samples heated to 80^0 C and above. Also, the diffusion coefficient is negligibly changed beyond T = 80^0 C. The lowest value for the diffusion coefficient of water, $(2.7 \pm 1.3) \times 10^{-4}$ mm^2/sec, occurs at 120^0 C. This value is ~ 60% lower than the D_w measured with the room temperature sample.

The product life of the sheath may be defined as the time taken for the water to penetrate through a sheath of (typical) thickness 3 mm. We estimated this time (t_p) for water diffusion through a sheath of thickness 3 mm (sheath product life) by using the equation $t_p = h^2/(4D_w)$, with $h = 3$ mm. The red data points in **Fig 7.3b** show the t_p vs temperature curve thus estimated. It is seen from this figure that water takes approximately 60 minutes to diffuse through a 3 mm thick sheath at room temperature, surprisingly close to what the manufacturers have reported anecdotally. Importantly, the figure shows that the t_p is much higher for the samples subjected to the 3-minute heat treatments. The t_p at 120^0 C for a 3 mm thick sheath is ~180 minutes, approximately three

times the t_p at RT. The data clearly shows that the high temperature heat treatments, in fact even at T = 80^0 C, can enhance product life by reducing the water diffusion.

7.4.2 Adaxial surface characterization

To better understand how the heat-treatments reduce the diffusion, we studied changes in the adaxial surface of the sheath due to the heating - changes which could have influenced the mass gain and diffusion process. This included microscopy of the adaxial surface using a high-resolution field-emission SEM (Quanta 3D) operating in low-vacuum mode; complemented by the FTIR and contact angle characterization. **Figure 7.4** shows SEM images of the adaxial surface at room temperature (left column) and for sheath exposed to T = 80^0 C for 3 minutes. A wax layer (< 1 µm thickness) is seen to formed on the adaxial surface after the heat-treatment. This layer is hydrophobic, as revealed by contact angle measurements (below) and prior work on waxes [91,97,98]. Furthermore, the wax also appears to fill the surface pores (stomata), see bottom row of images in **Fig. 7.4**. This filling of the stomata could also contribute, albeit second-order, to increasing the time taken for a liquid to penetrate the adaxial surface.

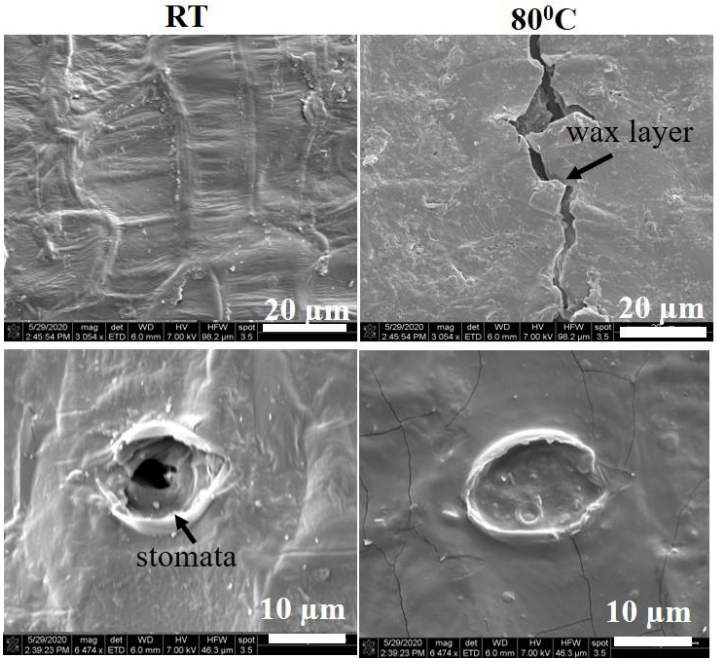

Figure 7.4 SEM images of sheath adaxial surface showing occurrence of wax layer on the adaxial surface in heated sample. (left) RT sample, (right) sheath heated to 80^0 C for 3 minutes. The bottom row shows closure of stomata pores by the wax.

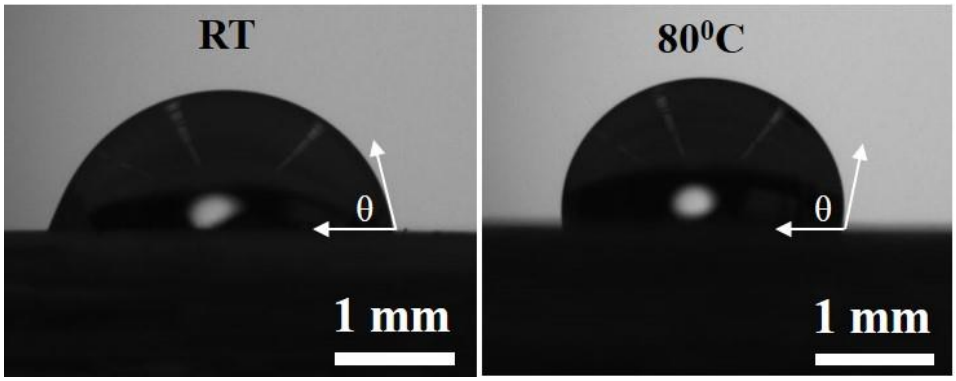

Figure 7.5 Contact angle measurement with water droplet (left) RT sheath sample (right) sheath heated to 80^0 C. Contact angles on the adaxial surface of the RT sheath and 80^0 C sheath are ~75^0 and ~105^0, respectively.

Figure 7.5 shows the contact angle measurement (θ). It is seen that the contact angle for the RT sheath adaxial surface is ~75^0, and for the T = 80^0 C sheath surface is ~105^0. The contact angles measured for the sheath adaxial surface heated to T = 120^0 C, 160^0 C and 200^0 C were all also > 90^0, indicating that when heated, a hydrophobic layer is formed on the adaxial surface.

The FTIR spectrum for the adaxial surface, plotted in **Fig 7.6** as intensity of absorbance spectrum vs wavenumber (cm^{-1}) for various T**,** confirmed the surface hydrophobic layer to be a wax layer (i.e., rich in wax components). The FTIR spectrum obtained for the RT sheath is similar to the spectrum for the base plant material [91,97,98]. For the sheaths heated to various temperatures, the FTIR spectrum shows new peaks in the spectrum. By comparing the spectra (e.g., peak locations) with spectra libraries - HR Nicolet sampler library and HR Aldrich FT-IR Collection Edition II – we could conclude that the spectra components match (> 85%) with those of organic waxes such as carnauba wax, vegetable wax from Brazilian palm tree and bee wax. The spectra for the higher T samples are also essentially the same as the spectrum of Carnauba wax reported in the literature [94].

The chemical formula for a typical wax unit is shown in (**Fig 7.6, right).** Specifically, the peaks in the sheath spectra of **Fig 7.6** were found to correspond to the following functional groups in waxes: (a) absorption band at 1165 cm^{-1} corresponds to the -CO bond, while the band at 1460 cm^{-1}corresponds to the -CH_2 bond; (b) the 1736 cm^{-1} peak corresponds to the stretching vibration of -C=O; and (c) the symmetrical and asymmetrical stretching of the -CH group are represented by the peaks at 2848 cm^{-1} and 2915 cm^{-1}, respectively [99,100].

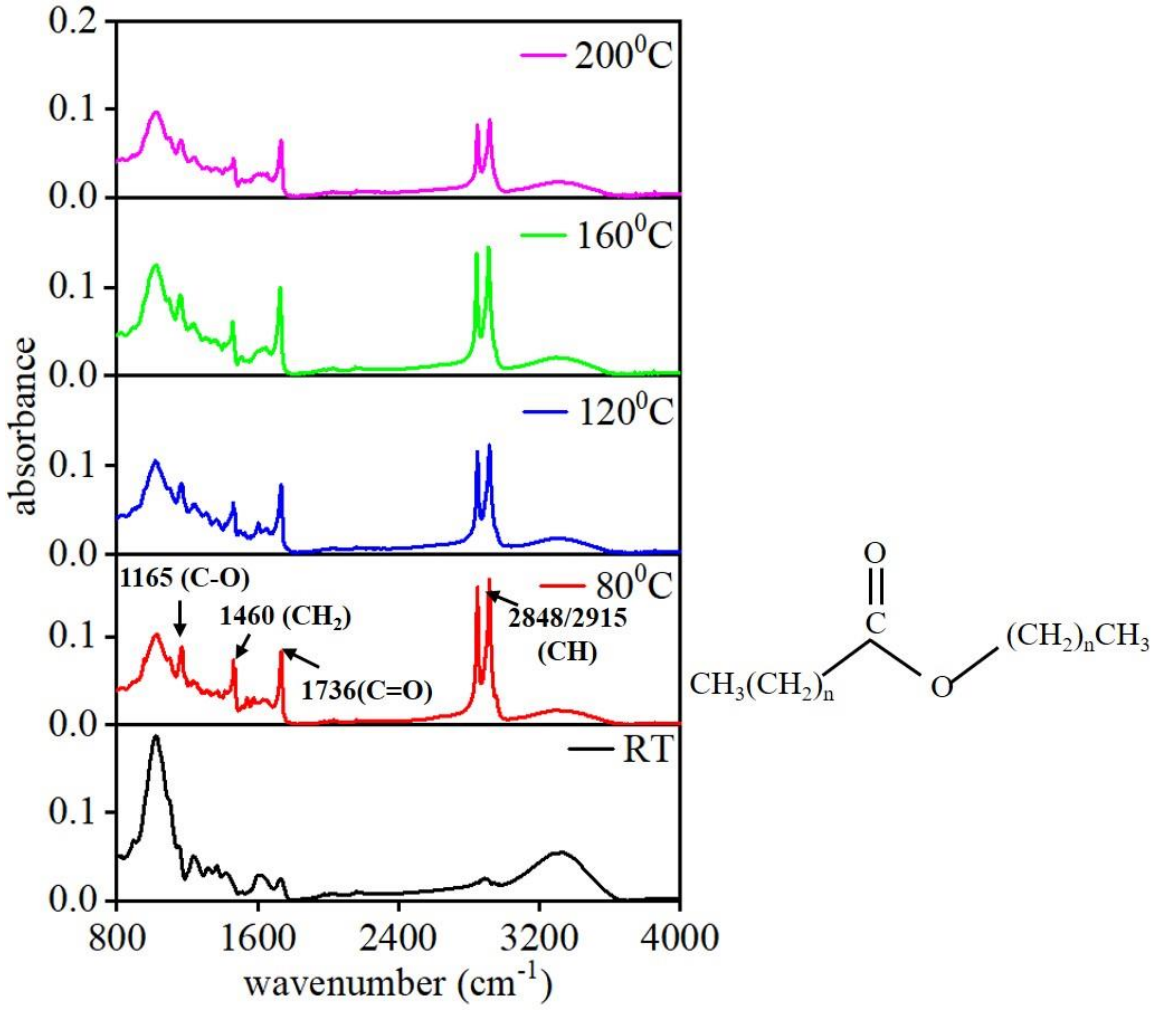

Figure 7.6 FTIR spectrum of the adaxial surface of RT sheath and sheath heated to higher temperatures. Peaks corresponding to functional groups in the wax are seen in the heated samples. Chemical formula for wax unit, highlighting functional groups, is shown in the right

7.4.3 Measurement of diffusion in a dewaxed sheath

Diffusion experiments were conducted with fully dewaxed sheath samples (with and without heat-treatment after the dewaxing) to see if there were any other factors (other than the wax secretion) that could explain the observed reductions in the diffusion coefficient after the high-temperature heat treatments. The dewaxing eliminates the wax hydrophobic effect as a variable in influencing the diffusion. The dewaxing was done with a solution of acetone and ethanol (Fischer Scientific). The sheath was cut into 10×10 mm^2 samples, typically used for the diffusion experiments. Each sample was then dewaxed by immersing it in the acetone-ethanol (2:1 v/v) solution at 80° C for 3 hours [22,23]. It is well-known that plant wax melts and dissolves in an acetone-ethanol solution at

80°C. The acetone-ethanol, together with the wax, was removed by filtering the samples using a Buckner funnel. Each sheath sample was then vacuum dried for 2 hours. The dewaxing procedure was repeated twice. The dewaxed samples were then heat treated at the various temperatures for 3 minutes.

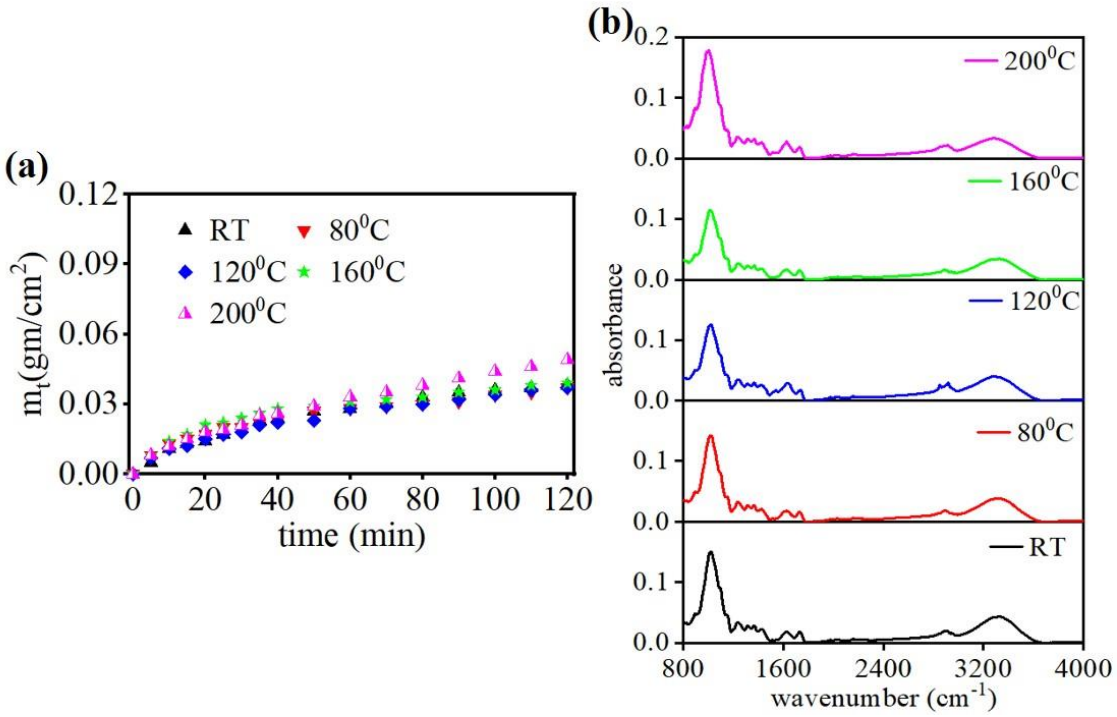

Figure 7.7 Diffusion measurements with dewaxed sheath subjected to heat-treatment. a) Plot of m_t vs t for samples heat-treated at various temperature after the dewaxing. b) The FTIR spectrum shows no peaks corresponding to wax such as observed in the non-dewaxed samples.

The diffusion mass-gain experiments were carried out with the dewaxed heat-treated samples as before, with the adaxial surface alone exposed to the water. **Figure 7.7a** shows the mass gain data plotted against time. There is negligible change in the m_t values with time between the RT and heat-treated samples, reinforcing that the wax hydrophobic layer is the cause for the diffusion reduction observed before. However, the overall mass gain was reduced (**Fig 7.7a**) compared to the non-dewaxed case (**Fig. 7.3**). We do not yet have an explanation based on structural or composition changes for this finding. We hope to study this further in the future. Based on this latter observation, an argument could be made that this dewaxing route offers a means for increasing product life. However, this dewaxing process is likely not feasible for practical

application in the foodware sector because it is time-consuming. Furthermore, the effect of the acetone and ethanol solution treatment on human health is an unknown variable.

Figure 7.7b also shows the results of FTIR analysis performed on the dewaxed samples, after heat-treatment to the different temperatures. Note that the heat treatment follows the dewaxing. These FTIR spectra do not show any peaks corresponding to wax, with any of the samples. The absence of the wax spectral peaks indicates that wax layers do not now form on the adaxial surface. This is because the wax has been removed by the dewaxing process.

Taken together, the various measurements prove that hydrophobic wax layers are secreted onto the adaxial surface upon heating and that these layers significantly reduce the diffusion of water in the sheath.

7.5 Discussion

The diffusion coefficient (D_w) of water through the sheath adaxial surface, which is typically in contact with the food, has been estimated using mass gain measurements for samples subjected to heat treatments at temperatures in the range of 80^0 C to 200^0 C for 3 minutes.

It is found that the diffusion coefficient for water through the adaxial surface is lowered significantly, from $(6.5 \pm 2.2) \times 10^{-4}$ mm^2/sec in regular untreated samples, to $(2.7 \pm 1.3) \times 10^{-4}\ \mathrm{mm}^2/\mathrm{sec}$ in sheath samples subjected to the heat-treatment (T $\geq 80^0$ C). Since there is negligible influence of T on the diffusion coefficient for T > 80^0 C, the heat-treatment at 80^0 C is sufficient to achieve significant reduction in the mass gain and diffusion coefficient. This diffusion reduction is shown to be due to secretion of a hydrophobic wax layer onto the wax surface for T $\geq 80^0$ C. The wax layer formation has been confirmed by SEM imaging and contact angle measurements; FTIR analysis showing presence of chemical groups typical of wax on the heat-treated sample (adaxial) surface; and diffusion experiments with samples subjected to a dewaxing treatment prior to the heat treatment (94,99,100). The 80^0 C temperature threshold is likely due to the fact that most plant waxes melt around this temperature. Hence, simply heating the sheath to 80^0 C causes the wax to melt and be ejected onto the surface to form a wax layer.

Using the measured diffusion coefficient data, we could estimate that the time (t_p) for penetration of water through a 3 mm thick sheath (typical sheath thickness) is increased from ~60 minutes to

~180 minutes. Since this time can be identified with the sheath life, based on structural integrity considerations, the results show that the foodware life can potentially be improved 3× by the wax-secretion heat treatment. Manufacturers of areca sheath foodware claim that plates and bowls made from the sheath can hold liquid food for ~ 60 minutes before the plate/bowl walls become soggy. Our measurements show that the time required for water to penetrate (~60 minutes) through a sheath of thickness 3 mm is remarkably close to the product life times reported by the areca foodware manufacturers.

The wax-secretion observations and diffusion measurements with heat-treated samples suggest opportunities for increasing foodware life by slowing down the diffusion process. Coating the adaxial surface of the sheath with a hydrophobic coating is one possible route for increasing product life. Such a coating will increase the time needed for the water to begin penetrating into the sheath as the adaxial surface will not wet immediately. The natural wax secretion by heating the sheath is another route for forming a hydrophobic layer and increasing foodware life. Superhydrophobic coatings, using edible wax such as carnauba wax and bee wax, can be created on the sheath adaxial surface using various techniques such as dipping, spraying, and brushing. Preliminary experiments done by fabricating Carnauba and bees wax layers on the sheath surface by dipping the sheath in molten wax dissolved in Ethanol show that product life can be enhanced to ~ 6 hours.

7.6 Conclusion

The diffusion of water in areca palm sheath heated to different temperatures in the range of 80^0 C to 200^0 C (for 3 minutes) has been studied experimentally using mass gain measurements. SEM imaging, contact angle measurement, and FTIR analysis were used to characterize changes to the adaxial surface arising from the heat-treatment and correlate these changes with the diffusion. The adaxial surface characterization showed that heating the sheath causes a natural wax to be secreted on the sheath surface, forming a hydrophobic layer. The hydrophobic layer acts as a barrier between water and the sheath, delaying the start of the diffusion process. The heat-treatment was found to lower the diffusion coefficient significantly. As a result, the life time of areca sheath for foodware could be tripled, from ~ 60 minutes to ~180 minutes, for a 3mm thick sheath. The results suggest opportunities for increasing the life and applications of palm-sheath foodware using

hydrophobic wax surface coatings. These coatings could be realized by inherent secretion of the wax from the sheath bulk onto the surface by suitable temperature-time heat treatments; application of external edible wax or equivalent plant-material coatings; or combinations thereof. We plan to explore some of these opportunities in the near future.

8. CONCLUSION AND FUTURE WORK

A study has been made of the structure, strength, formability, and diffusion properties of areca palm sheath. The study of these properties is motivated by use of the sheath material in eco-friendly foodware such as plates and bowls, wherein these properties are known to play an important role in determining what product shapes can be formed, material structural integrity and product lifetime. The sheath material has a long, flat and slender shape whose exterior abaxial and adaxial sides are characterized by striations that run along the length of the sheath. The sheath thickness is typically about 3 mm, and the thickness of the abaxial and adaxial epidermis (skin) layers are ~ 20 um. The abaxial surface has a greater hardness and stiffness (Young's Modulus) than the adaxial surface. The bulk of the sheath interior is found to resemble a unidirectional fiber-reinforced composite, with the principal constituents being fiber (25 %, area fraction), matrix (75 %, area fraction) and porosity (0.6-0.7). The fibers run parallel to the surface striations. Based on comparison of the sheath structure attributes - morphology (external) and anatomy (internal) - with those of palm leaf and stem, we conclude from the structure analysis that the sheath is a hybrid of the leaf and the stem.

The strength properties and deformation response (formability) of the sheath have been characterized in terms of uniaxial tension and compression, rolling and biaxial stretching. It is shown that hydration of the sheath has a large effect on the deformation response, enabling strains of 0.3 to 2 to be reached prior to failure depending on the loading configuration. In loading by biaxial stretching (Limited Dome Height (LDH) testing), that is analogous to the sheath stretch forming process, the sheath is seen to withstand forming limit strains of 0.3 to 0.6. The highest limit strains are obtained when the sheath is given a treatment prior to the forming process with aqueous NaOH solution (5% NaOH by weight). For NaOH concentrations $\leq$5%, the treatment has negligible impact on the sheath microstructure while significantly enhancing formability. The biaxial stretch formability of the sheath under hydrated conditions is similar to or superior to that of very ductile sheet metals like Al and Cu. However, the sheath formability differs from (plastic) ductility as defined in the conventional sense for metals. While the sheath deformation strain is large under load, it is not plastic deformation like with metals - the deformation has to be "locked in" by a short-term exposure (3 minutes) to heat at temperatures of ~ 120 ^{0}C that drives out the

water. The results also demonstrate that conventional formability tests, usually employed to assess sheet metal formability, can be applied to plant materials and establish forming limit diagrams for facilitating product design.

We have characterized the diffusion of water in the sheath. This characterization shows that the structural integrity and life of areca sheath foodware are determined by diffusion of liquids through the sheath wall thickness. The diffusion of water is studied using mass gain measurements and *in situ* imaging of water transport. We establish diffusion coefficient values for the bulk composite, accounting for factors such as material swelling due to the water absorption. We also find that the diffusion coefficient for the matrix is one order of magnitude greater than for the fiber; hence matrix diffusion controls the overall water transport process through the sheath wall. We vary salt concentration in the water by controlled additions of NaCl (another key food constituent) and note a non-monotonic dependence of the diffusion on concentration. By subjecting the leaf-sheath to a short-time (~ 3 minutes) thermal treatment (80^0 C), a hydrophobic wax layer can be made to secrete onto the leaf surface. This wax coating significantly reduces the water diffusion, enabling sheath foodware life time to be increased 2 to 3-fold.

The leaf-sheath is a "waste product" of the palm. Since the forming forces are negligibly small, the areca sheath foodware is found to have negligible embodied energy (4 to 5 orders of magnitude smaller) compared to paper and plastics based foodware. Also, areca sheath is known to degrade in about 100 days. These additional attributes of the sheath, in conjunction with the primary attributes of high formability and sufficiently small diffusion, make the sheath an attractive material for foodware and related applications, both based on considerations of ease of manufacture and sustainability.

The research provides a foundation for identifying a broader class of plant materials for use in production of sustainable foodware products including packaging. The techniques developed in the research can be used to quickly evaluate strength and formability attributes, together with diffusion properties. This should help in screening plant material systems with suitable combinations of properties that will maximize ease of production (manufacturability) and product life time (structural integrity). In the immediate future, we seek to explore food-friendly hydrophobic coatings that can be easily applied to sheath surfaces to reduce diffusion, thereby improving product life and advancing commercial applications of the areca sheath. In the longer

term, we plan a systematic program to identify a broader class of plant materials that can be directly formed into high-aspect ratio shapes, beginning with various palm species that are quite abundant in nature.

REFERENCES

1. Geyer R, Jambeck JR, Law KL. Production, use, and fate of all plastics ever made. Science Advances. 2017; 3 (7): e1700782.
2. Moss E and Grousset R. The Dirty Truth About Disposable Foodware, February 2020 [Available from: https://www.mossandmollusk.com/the-dirty-truth].
3. Haward M. Plastic pollution of the world's seas and oceans as a contemporary challenge in ocean governance. Nature communications. 2018; 9 (1): 1-3. .
4. Charaka-Samhita, translated by Avinash Chandra Kaviratna, Dass (Calcutta). 1890; 1732-1837.
5. Meulenbeld GJ. A History of Indian Medical Literature. Groningen. 1999–2002; IA: 7–180.
6. Krishnamurthy KH. Supari or betel nut (areca catechu, Linn.). Journal of New Approaches to Medicine and Health. 2009; 17 (3).
7. Raghavan V, Baruah HK. Arecanut: India's popular masticatory—history, chemistry and utilization. Economic Botany. 1958; 12 (4): 315-345.
8. Andrady AL. Microplastics in the marine environment. Marine Pollution Bulletin. 2011; 62 (8): 1596-1605.
9. Sukhdev P. Costing the earth. Nature. 2009; 462 (7271): 277.
10. Costanza R, d'Arge R, De Groot R, Farber S, Grasso M, Hannon B, Limburg K, Naeem S, O'neill RV, Paruelo J, Raskin RG. The value of the world's ecosystem services and natural capital. Nature. 1997; 387 (6630): 253-260.
11. Watt G. A dictionary of the economic products of India. Cambridge University Press. 2014.
12. Gupta PC, Warnakulasuriya S. Global epidemiology of areca nut usage. Addiction Biology. 2002; 7 (1): 77-83.
13. Bomhard ML. Palm trees in the United States. US Department of Agriculture, Forest Service. 1950; 22.
14. Tomlinson PB. The uniqueness of palms. Botanical Journal of the Linnean Society. 2006; 151 (1): 5-14.
15. Kalita P, Dixit US, Mahanta P, Saha UK. A novel energy efficient machine for plate manufacturing from areca palm leaf sheath. Journal of Scientific & Industrial Research. 2008; 67: 807-811.

16. Ashby MF. Materials and the Environment: Eco-Informed Material Choice. 2nd edition. Elsevier; 2013.
17. Costanza R. Embodied energy and economic valuation. Science. 1980; 210 (4475): 1219-1224.
18. Guo M, Zhang TH, Chen BW, Cheng L. Tensile strength analysis of palm leaf sheath fiber with Weibull distribution. Composites Part A: Applied Science and Manufacturing. 2014; 62: 45-51.
19. Zhang T, Guo M, Cheng L, Li X. Investigations on the structure and properties of palm leaf sheath fiber. Cellulose. 2015; 22(2): 1039-1051.
20. Koch K, Neinhuis C, Ensikat HJ, Barthlott W. Self assembly of epicuticular waxes on living plant surfaces imaged by atomic force microscopy (AFM). Journal of Experimental Botany. 2004; 55(397): 711-718.
21. Koch K, Ensikat HJ. The hydrophobic coatings of plant surfaces: epicuticular wax crystals and their morphologies, crystallinity and molecular self-assembly. Micron. 2008; 39(7): 759-772.
22. Sun XF, Sun RC, Su Y, Sun JX. Comparative study of crude and purified cellulose from wheat straw. Journal of agricultural and food chemistry. 2004; 52(4): 839-847.
23. Morán JI, Alvarez VA, Cyras VP, Vázquez A. Extraction of cellulose and preparation of nanocellulose from sisal fibers. Cellulose. 2008; 15(1): 149-159.
24. Underwood E, Qauntitative Stereology. Addison Wesley; 1970. .
25. El Messiry M. Theoretical analysis of natural fiber volume fraction of reinforced composites. Alexandria Engineering Journal. 2013; 52(3): 301-306.
26. Tomlinson PB, Horn JW, Fisher JB. The Anatomy of Palms: Arecaceae - Palmae. Oxford University Press; 2011.
27. Guerriero G, Hausman JF, Legay S. Silicon and the plant extracellular matrix. Frontiers in plant science. 2016; 7: 463.
28. Cao BL, Ma Q, Zhao Q, Wang L, Xu K. Effects of silicon on absorbed light allocation, antioxidant enzymes and ultrastructure of chloroplasts in tomato leaves under simulated drought stress. Scientia horticulturae. 2015; 194: 53-62.

29. Ye M, Song Y, Long J, Wang R, Baerson SR, Pan Z, Zhu-Salzman K, Xie J, Cai K, Luo S, Zeng R. Priming of jasmonate-mediated antiherbivore defense responses in rice by silicon. Proceedings of the National Academy of Sciences. 2013; 110 (38): E 3631-3639.
30. Dunn DB, Sharma GK, Campbell CC. Stomatal patterns of dicotyledons and monocotyledons. American Midland Naturalist. 1965:185-195.
31. Staples GW, Bevacqua RF. Areca catechu (betel nut palm). Species profiles for Pacific Island Agroforestry. 2006; 1-17.
32. Corner EJ. The natural history of palms. University of Carlifornia Press, 1966.
33. Gibson LJ. The hierarchical structure and mechanics of plant materials. Journal of the royal society interface. 2012; 9(76): 2749-2766.
34. Gibson LJ, Ashby MF, Harley BA. Cellular materials in nature and medicine. Cambridge University Press; 2010.
35. Srivaro S, Rattanarat J, Noothong P. Comparison of the anatomical characteristics and physical and mechanical properties of oil palm and bamboo trunks. Journal of Wood Science. 2018; 64(3): 186-192.
36. Dixon PG, Gibson LJ. The structure and mechanics of Moso bamboo material. Journal of the Royal Society Interface. 2014; 11(99): 20140321.
37. Tan T, Rahbar N, Allameh SM, Kwofie S, Dissmore D, Ghavami K, Soboyejo WO. Mechanical properties of functionally graded hierarchical bamboo structures. Acta biomaterialia. 2011; 7(10): 3796-3803.
38. Fratzl P, Weinkamer R. Nature's hierarchical materials. Progress in Materials Science. 2007; 52 (8): 1263-1334.
39. Huang P, Chang WS, Ansell MP, John CY, Shea A. Porosity estimation of Phyllostachys edulis (Moso bamboo) by computed tomography and backscattered electron imaging. Wood Science and Technology. 2017; 51(1): 11-27.
40. Obataya E, Norimoto M, Gril J. The effects of adsorbed water on dynamic mechanical properties of wood. Polymer. 1998; 39(14): 3059-3064.
41. Hunt DG. A unified approach to creep of wood. Proceedings of the Royal Society of London. Series A: Mathematical, Physical and Engineering Sciences. 1999; 455(1991): 4077-4095.
42. Dieter GE. Mechanical Metallurgy. 2nd ed., McGraw-Hill, New York; 1976. .
43. Atlas of Stress-strain Curves. ASM International, 2nd Edition; 2002.

44. Davis JR, editor. Copper and Copper Alloys. ASM International; 2001.
45. Semiatin SL. editor. Metalworking: sheet forming. ASM international; 2006.
46. Chen Y, Zhang K, Zhang T, Yuan F, Su N, Weng B, Wu S, Guo Y. Effect of softening treatments on the properties of high-density cylindrical luffa as potential mattress cushioning material. Cellulose. 2019; 26(18):9831-9852.
47. Marciniak Z, Duncan J, Mechanics of Sheet Metal Forming. Edward Arnold; 1991. .
48. Keeler SP and Backhofen WA, Plastic instability and fracture in sheet stretched over rigid punches. ASM Transactions. 1963; 56(11): 25-48.
49. Backofen WA. Deformation processing. Metallurgical Transactions. 1973; 4(12): 2679-2699.
50. Hecker SS. A cup test for assessing stretchability; 1974.
51. Azrin M, Backofen WA. The deformation and failure of a biaxially stretched sheet. Metallurgical Transactions. 1970; 1(10): 2857-2865.
52. Chadwick P, Continuum Mechanics. Wiley; 1976.
53. Timoshenko SP, Woinowsky-Krieger S, Theory of Plates and Shells. McGraw-hill; 1959.
54. Hill R. C. A theory of the plastic bulging of a metal diaphragm by lateral pressure. Philosophical Magazine. 1950; 41(322):1133-1142.
55. Chen G, Luo H, Yang H, Zhang T, Li S. Water effects on the deformation and fracture behaviors of the multi-scaled cellular fibrous bamboo. Acta Biomaterialia. 2018; 65: 203-215.
56. Le Moigne N, Navard P. Dissolution mechanisms of wood cellulose fibres in NaOH–water. Cellulose. 2010; 17(1): 31-45.
57. Song J, Chen C, Wang C, Kuang Y, Li Y, Jiang F, Li Y, Hitz E, Zhang Y, Liu B, Gong A. Superflexible wood. ACS applied materials & interfaces. 2017; 9(28): 23520-23527.
58. Song J, Chen C, Zhu S, Zhu M, Dai J, Ray U, Li Y, Kuang Y, Li Y, Quispe N, Yao Y. Processing bulk natural wood into a high-performance structural material. Nature. 2018; 554(7691): 224-208.
59. Mohanty DP, Udupa A, Chandra AR A, Viswanathan K, Mann JB, Trumble KP, Chandrasekar S. Mechanical behavior and high formability of palm leaf materials. Advanced Energy and Sustainability Research. 2021; 2(4): 2000080.

60. Shi Z, Yang Q, Kuga S, Matsumoto Y. Dissolution of wood pulp in aqueous NaOH/urea solution via dilute acid pretreatment. Journal of agricultural and food chemistry. 2015; 63(27): 6113-6119.
61. Shi Z, Yang Q, Cai J, Kuga S, Matsumoto Y. Effects of lignin and hemicellulose contents on dissolution of wood pulp in aqueous NaOH/urea solution. Cellulose. 2014; 21(3): 1205-2015.
62. Le Moigne N, Navard P. Dissolution mechanisms of wood cellulose fibres in NaOH–water. Cellulose. 2010; 17(1): 31-45.
63. Shi J, Lu Y, Zhang Y, Cai L, Shi SQ. Effect of thermal treatment with water, H 2 SO 4 and NaOH aqueous solution on color, cell wall and chemical structure of poplar wood. Scientific reports. 2018; 8(1):1-9.
64. Borysiak S, Doczekalska B. X-ray diffraction study of pine wood treated with NaOH. Fibres Text. East. Eur. 2005; 13(5):87-89.
65. Hsiao TC, Acevedo E, Fereres E, Henderson DW. Water stress, growth and osmotic adjustment. Philosophical Transactions of the Royal Society of London. B, Biological Sciences. 1976; 273(927): 479-500.
66. Bernacchi CJ, VanLoocke A. Terrestrial ecosystems in a changing environment: a dominant role for water. Annual Review of Plant Biology. 2015; 66: 599-622.
67. Borrega M, Tolonen LK, Bardot F, Testova L, Sixta H. Potential of hot water extraction of birch wood to produce high-purity dissolving pulp after alkaline pulping. Bioresource Technology. 2013; 135: 665-671.
68. Gordon JE. The New Science of Strong Materials. Princeton University Press, Princeton, NJ, 2018.
69. Levy JF. The natural history of the degradation of wood. Philosophical Transactions of the Royal Society of London. Series A, Mathematical and Physical Sciences. 1987; 321(1561): 423-433.
70. Burr HK, Stamm AJ. Diffusion in wood. The Journal of Physical Chemistry. 1947; 51(1): 240-261.
71. Célino A, Fréour S, Jacquemin F, Casari P. The hygroscopic behavior of plant fibers: a review. Frontiers in Chemistry. 2014; 1: 43.

72. Amer M, Kabouchi B, Rahouti M, Famiri A, Fidah A, El Alami S, Ziani M. Experimental study of the linear diffusion of water in clonal eucalyptus wood. International Journal of Thermophysics. 2020; 41(10): 1-7.
73. Penvern H, Zhou M, Maillet B, Courtier-Murias D, Scheel M, Perrin J, Weitkamp T, Bardet S, Caré S, Coussot P. How bound water regulates wood drying. Physical Review Applied. 2020; 14(5): 054051.
74. Gezici-Koç Ö, Erich SJ, Huinink HP, Van der Ven LG, Adan OC. Bound and free water distribution in wood during water uptake and drying as measured by 1D magnetic resonance imaging. Cellulose. 2017; 24(2): 535-553.
75. Rafsanjani A, Stiefel M, Jefimovs K, Mokso R, Derome D, Carmeliet J. Hygroscopic swelling and shrinkage of latewood cell wall micropillars reveal ultrastructural anisotropy. Journal of the Royal Society Interface. 2014; 11(95): 20140126.
76. Siau JF. Transport Processes in Wood. Springer, 1984.
77. Dayananda MA, Grace RE. Ternary diffusion in copper-zinc-manganese alloys. Transactions of the Metallurgical Society of AIME. 1965; 233(7): 1287-1293.
78. Dayananda MA, Kirsch PF, Grace RE. Ternary diffusion in Cu-Zn-Sn solid solutions. Transactions of the Metallurgical Society of AIME. 1968; 5: 885-890.
79. Udupa A, Viswanathan K, Ho Y, Chandrasekar S. The cutting of metals via plastic buckling. Proceedings of the Royal Society A: Mathematical, Physical and Engineering Sciences. 2017; 473(2202): 20160863.
80. Crank J. The Mathematics of Diffusion. Oxford University Press, 1979.
81. Wilkinson DS. Mass Transport in Solids and Fluids. Cambridge University Press; 2000.
82. Dayananda MA. Average effective interdiffusion coefficients and the Matano plane composition. Metallurgical and Materials Transactions A. 1996; 27(9): 2504-2509.
83. Kestin J, Khalifa HE, Correia RJ. Tables of the dynamic and kinematic viscosity of aqueous NaCl solutions in the temperature range 20–150 C and the pressure range 0.1–35 MPa. Journal of Physical and Chemical Reference Data. 1981; 10(1): 71-88.
84. Olek W, Weres J. Drying of Porous Materials. Springer, Dordrecht, 2006.
85. Chang YC, Myerson AS. The diffusivity of potassium chloride and sodium chloride in concentrated, saturated, and supersaturated aqueous solutions. AIChE Journal. 1985; 31(6): 890-894.

86. Antonio GC, Azoubel PM, Murr FE, Park KJ. Osmotic dehydration of sweet potato (Ipomoea batatas) in ternary solutions. Food Science and Technology. 2008; 28(3): 696-701.
87. Kim JS, Wu Z, Morrow AR, Yethiraj A, Yethiraj A. Self-diffusion and viscosity in electrolyte solutions. The Journal of Physical Chemistry B. 2012; 116(39): 12007-12013.
88. Mokhothu TH, John MJ. Bio-based coatings for reducing water sorption in natural fibre reinforced composites. Scientific reports. 2017; 7(1):1-8.
89. Bourtoom T. Edible films and coatings: characteristics and properties. International food research journal. 2008; 15(3) :237-248.
90. Alam M, Akram D, Sharmin E, Zafar F, Ahmad S. Vegetable oil based eco-friendly coating materials: A review article. Arabian Journal of Chemistry. 2014;7(4): 469-479. .
91. Wang W, Lockwood K, Boyd LM, Davidson MD, Movafaghi S, Vahabi H, Khetani SR, Kota AK. Superhydrophobic coatings with edible materials. ACS applied materials & interfaces. 2016; 8(29): 18664-18668.
92. Freitas CA, Sousa PH, Soares DJ, Silva JY, Benjamin SR, Guedes MI. Carnauba wax uses in food–A review. Food chemistry. 2019;291:38-48.
93. Vandenburg LE, Wilder EA. The structural constituents of carnauba wax. Journal of the american oil chemists society. 1970; 47(12): 514-518.
94. Oliveira TA, Mota ID, Carvalho LH, Barbosa R, Alves TS. Influence of carnauba wax on films of poly (butylene adipate co-terephthalate) and sugarcane residue for application in soil cover (mulching). Materials Research. 2019; 22: e20190040.
95. Owolabi AF, Ghazali A, Khalil HA, Hassan A, Arjmandi R, Fazita MN, Haafiz MM. Isolation and characterization of microcrystalline cellulose from oil palm fronds using chemomechanical process. Wood and Fiber Science. 2016; 48(4): 1-11.
96. Dehghani A, Ardekani SM, Al-Maadeed MA, Hassan A, Wahit MU. Mechanical and thermal properties of date palm leaf fiber reinforced recycled poly (ethylene terephthalate) composites. Materials & Design (1980-2015). 2013; 52: 841-848.
97. Janesch J, Arminger B, Gindl-Altmutter W, Hansmann C. Superhydrophobic coatings on wood made of plant oil and natural wax. Progress in Organic Coatings. 2020; 148: 105891.
98. Troughton JH, Hall DM. Extracuticular wax and contact angle measurements on wheat (Triticum vulgare L.). Australian Journal of Biological Sciences. 1967; 20(3): 509-526.

99. Gonultas O, Candan Z. Chemical characterization and ftir spectroscopy of thermally compressed eucalyptus wood panels. Maderas. Ciencia y tecnología. 2018; 20(3): 431-442.
100. Nandiyanto AB, Oktiani R, Ragadhita R. How to read and interpret FTIR spectroscope of organic material. Indonesian Journal of Science and Technology. 2019; 4(1): 97-118.

VITA

Debapriya Pinaki Mohanty was born in April 1987 in Basta, Odisha, India. He completed his undergraduate degree in 2010 from the Department of Mechanical Engineering, Veer Surendra Sai University of Technology, Burla. In 2012, he completed his Masters in Technology from Department of Mechanical Engineering, IIT Kanpur, with specialization in Solid Mechanics. Upon graduation, Debapriya accepted a position with Renault Nissan Technology and Business Center India, Chennai, as a graduate engineer. Debapriya returned to academia in 2015 and obtained an MS degree from the School of Aeronautics and Astronautics, Purdue University, in 2017. He then began his doctoral studies in the School of Industrial Engineering at Purdue University, with Professor Srinivasan Chandrasekar in the Center for Materials Processing and Tribology.